

This item was submitted to [Loughborough's Research Repository](#) by the author.  
Items in Figshare are protected by copyright, with all rights reserved, unless otherwise indicated.

## **Molecular dynamics simulation of fracture and energy dissipation in polymer/clay nanocomposites**

PLEASE CITE THE PUBLISHED VERSION

PUBLISHER

© Lei Chen

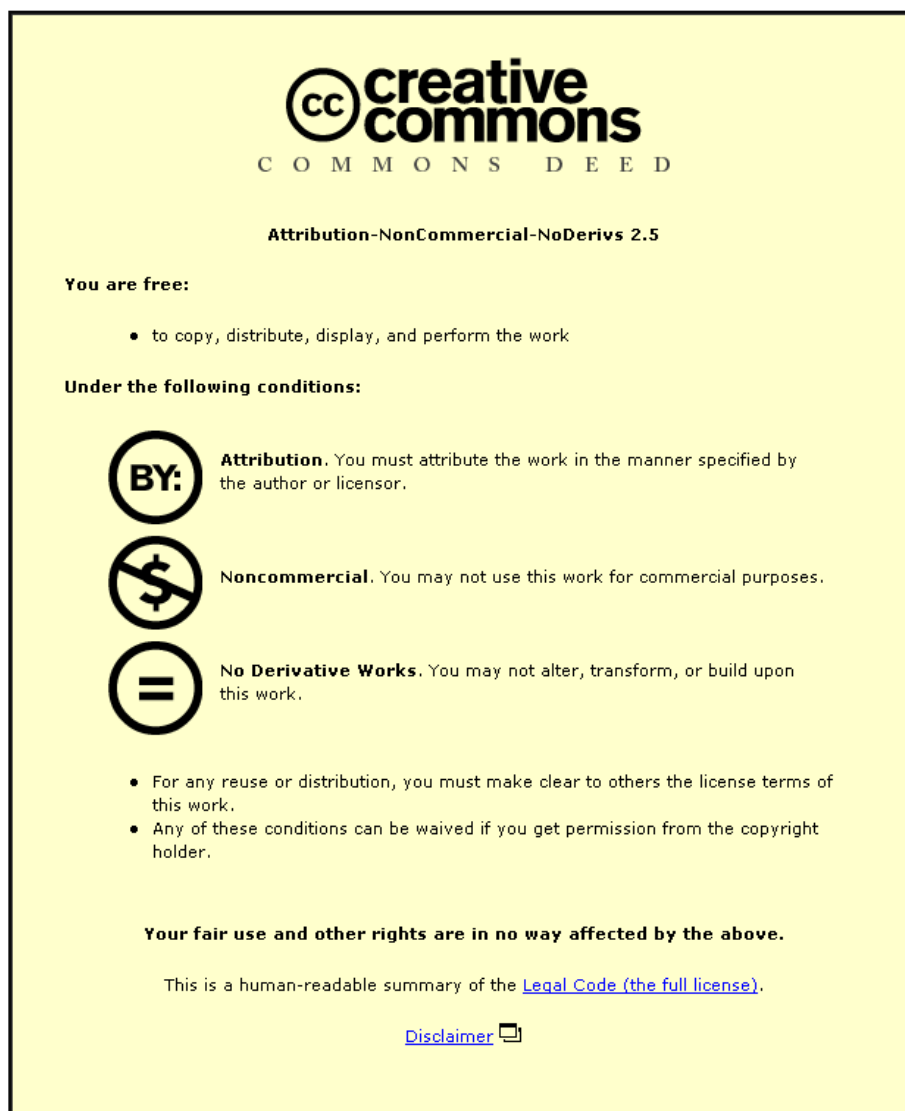
LICENCE

CC BY-NC-ND 4.0

REPOSITORY RECORD

Chen, Lei. 2012. "Molecular Dynamics Simulation of Fracture and Energy Dissipation in Polymer/clay Nanocomposites". figshare. <https://hdl.handle.net/2134/10764>.

This item was submitted to Loughborough University as a PhD thesis by the author and is made available in the Institutional Repository (<https://dspace.lboro.ac.uk/>) under the following Creative Commons Licence conditions.



For the full text of this licence, please go to:  
<http://creativecommons.org/licenses/by-nc-nd/2.5/>

## University Library

Author/Filing Title ..... *CHEV, L.* .....

.....  
Class Mark ..... *T* .....

**Please note that fines are charged on ALL  
overdue items.**

--	--	--

0403819601





# **Molecular Dynamics Simulation of Fracture and Energy Dissipation in Polymer/Clay Nanocomposites**

by

**Lei CHEN**

**A doctoral thesis submitted in partial fulfillment of the  
requirements for the award of Doctor of Philosophy of  
Loughborough University**

**Supervisor: Dr. Mo SONG**

**Institute of Polymer Technology and materials Engineering  
Loughborough University**

**© Lei CHEN 2008**



Loughborough  
University  
Pilkington Library

Date 1/3/10

Class T

Acc  
No. 0403819601

## **ACKNOWLEDGEMENTS**

First of all, I would like to express my sincere thanks to my supervisor, Dr. Mo Song, for his great encouragement, invaluable help, advices and considerable contribution throughout this project.

I would also like to express my grateful appreciate to Dr. Jie Jin for her great encouragement and invaluable help and to Dr. Kejian Yao and Dr. Hesheng Xia for the preparation of experimental specimens.

I would like to extend my special thanks to Miss Li Sun for her kindly help with normal living.

Finally, I would like to express my thanks to all technical and support staff and all students in IPTME, especially to Mr. Ray Owens for his kindly help with tensile test

## ABSTRACT

Molecular dynamics simulation method was used to investigate the effect of nanofillers on fracture strength and energy dissipation of polymers, including nanofillers contents, interaction strength between the nanofillers and polymer chains, relaxation time and geometry of the nanofillers. Molecular dynamics simulation results revealed that the addition of layered silicate can improve the fracture strength of polymers. The interactions between the surface of layered silicate and polymer chains, and the difference between the relaxation times of layered silicate and that of polymer chains have significant influences on the fracture strength and energy dissipation of polymers. For these polymers, which  $T_g$ s are lower than room temperature, such as polyurethane, or nearby (or equal to) room temperature, such as Nylons, the nanoplatelets can always enhance the mechanical properties. However, for these polymers, which  $T_g$ s are higher than room temperature, such as epoxy and polystyrene, the addition of the nanoplatelets does not work well for toughening these polymers. If one wants the nanoplatelets to be working for toughening these polymers, it is necessary to build up a stress relaxation interface between the polymer matrix and the nanoplatelets, such as the modification of the surfaces of nanofillers using coupling agents. When the relaxation time of the polymer is long enough, the incorporation of nanofillers into the polymer will cause the polymer to become more brittle. This result explains why the toughness of epoxy/ clay nanocomposites becomes poor. The simulation results clearly revealed that the orientation of nanoplatelets is reversible at low strain of 50% suggesting that additional energy dissipation only results from the frictional sliding at the interface, whereas the orientation of nanoplatelets at large strain of 200% showed more irreversibility suggesting that the additional energy loss results from both the interfacial frictional sliding and the orientation of the nanoplatelets. The additional dissipated energy was also influenced by the strength of interactions between polymer chains and clay platelets. The stronger interactions the more energy dissipated. Molecular dynamics simulation results revealed that the geometry of nanofillers also affect the mechanical properties of polymer nanocomposites. The enhancement of carbon nanotubes on the mechanical properties of the polymers are enhanced the greatest by carbon nanotubes.



## TABLE OF CONTENTS

<b>CHAPTER 1: INTRODUCTION AND OBJECTIVES OF THE PROJECT .....</b>	<b>1</b>
1.1 Introduction .....	1
1.2 Objectives Of The Project .....	5
Reference .....	5
 <b>CHAPTER 2: PRINCIPLE OF MOLECULAR DYNAMICS SIMULATION .....</b>	 <b>7</b>
2.1 Introduction .....	7
2.2 Statistical Mechanics .....	8
2.2.1 Time Average Of Physical Properties .....	8
2.2.2 Potential Energy .....	9
2.2.3 Kinetic Energy .....	9
2.2.4 Total Energy .....	10
2.2.5 Temperature .....	10
2.2.6 Pressure .....	11
2.2.7 Mean Space Displacement .....	14
2.2.8 Real Space Correlation .....	15
2.3 Equation Of Motion .....	17
2.3.1 Lagrangian Fuction .....	17
2.3.2 Hamiltonian Function .....	18
2.4 Intermolecular Potentials and Force Calculation .....	19
2.4.1 Lennard-Jones Potential and Its Force Calculation .....	20
2.4.2 Finitely- Extensible Non-Linear Elastic (FENE) Potential and Force Calculation .....	23
2.4.3 Lennard-Jones Reduced Units .....	24
2.5 Intergrating The Equations of Motion .....	25
2.5.1 The Verlet Algorithm .....	25
2.5.2 The Euler Scheme Algorithm .....	26
2.5.3 The Leapforg Algorithm .....	27

2.5.4 Velocity-Verlet Algorithm .....	28
2.5.5 Beeman Algorithm .....	29
2.5.6 Predictor-Corrector Algorithm .....	30
2.5.7 Periodic Boundary Condition .....	31
2.6 State Of The MD Simulation .....	32
2.6.1 Initial State .....	32
2.6.2 Equilibration .....	33
2.7 Applications .....	33
Reference .....	36

**CHAPTER 3: PROGRAMME FOR MOLECULAR DYNAMICS SIMULATION OF  
FRACTURE AND ENERGY DISSIPATION ..... 39**

3.1 Introduction .....	39
3.2 Programme for Molecular Dynamics Simulation Of Fracture In Polymer Composites	43
3.2.1 Configuration .....	43
3.2.2 Simulation .....	50
3.2.3 Data Output And Graphing .....	61
3.3 Programme For Molecular Dynamics Simulation Of Energy Dissipation In Polymer nanocomposites .....	62
3.3.1 Configuration .....	62
3.3.2 Simulation .....	69
3.3.3 Data Output And Graphing .....	80

**CHAPTER 4: MOLECULAR DYNAMICS SIMULATION OF FRACTURE IN  
POLYMER/CLAY NANOPATELET NANOCOMPOSITES 82**

4.1 Introduction .....	82
4.2 Molecular Dynamics Simulation Of Fracture In Polymer/Clay Nanocomposite .....	83
4.2.1 Background Of mechanical Properties .....	83
4.2.2 Effect Of Incorporation Of Nanoplatelets On Fracture .....	91

4.2.3 Effect Of Interaction Between Nanoplatelets And Polymers On Fracture .....	105
4.2.4 Effect Of Relaxation Time On Fracture .....	112
Reference .....	119

## **CHAPTER 5: ENERGY DISSIPATION AND ENHANCEMENT OF FATIGUE DURABILITY OF POLYMER NANOCOMPOSITES .....**

5.1 Introduction .....	121
5.2 Simulation, And Experiments For Comparison .....	123
5.2.1 Simulation .....	123
5.2.1.1 Model .....	123
5.2.1.2 Simulation .....	124
5.2.2 Experimental .....	125
5.2.2.1 Materials .....	125
5.2.2.2 Sample Preparation .....	130
5.2.2.3 Hysteresis Test .....	130
5.2.2.4 Cyclic Fatigue test .....	131
5.2.2.5 Wide-Angle X-Ray Diffraction .....	131
5.3 Energy Dissipation In Exfoliation Polymer/Organoclay Nanocomposites .....	131
5.3.1 Introduction .....	132
5.3.2 Results And Discussion .....	132
5.3.3 Experimental Comparison .....	142
5.3.4 Orientation Factor Of Nanofillers .....	146
5.4 Enhancement Of Fatigue Durability By Incorporation Of Clay And Its Mechanism .....	154
5.4.1 Introduction .....	154
5.4.2 Enhancement Of Fatigue Durability By Incorporation Of Clay .....	157
5.4.3 Mechanism Of The Enhancement Of Fatigue Durability .....	160
Reference .....	167

## **CHAPTER 6: EFFECT OF GEOMETRY OF NANOFILLERS ON FRACTURE OF**

<b>POLYMERS .....</b>	<b>169</b>
6.1 Introduction .....	169
6.2 Models Of Simulation .....	172
6.2.1 Model Of A Polymer Chain .....	172
6.2.2 Model Of A Nanoparticle .....	172
6.2.3 Model Of A Nanoplatelet .....	174
6.2.4 Model Of A Nanotube .....	176
6.3 Results And Discussion .....	180
Reference .....	186
 <b>CHAPTER 7: CONCLUSIONS AND FUTURE WORK .....</b>	 <b>188</b>
<b>APPENDIX .....</b>	<b>193</b>

## LIST OF FIGURES

Figure 1.1	Schematic of the three types of nanofillers.	1
Figure 1.2	Structure of 2:1 phyllosilicates.	2
Figure 1.3	Scheme of two different types of nanocomposite arising from the interaction of layered silicates and polymers: (a) intercalated nanocomposite and (b) exfoliated nanocomposite.	3
Figure 2.1	The sketch map of what the computer simulations can do.	7
Figure 2.2	A schematic of the loading external force.	13
Figure 2.3	The curve of Lennard-Jones potential.	21
Figure 2.4	A sketch of periodic boundary condition (a) cut-off sphere in conventional way; (b) cut-off sphere partitioned under periodic boundary condition.	21
Figure 2.5	The curve of Lennard-Jones potential with cut-off radius.	22
Figure 2.6	The curve of FENE potential	23
Figure 2.7	The curve of how Predictor-corrector algorithm works.	30
Figure 2.8	A sketch of a two dimensional simulation cell using the periodic boundary condition	32
Figure 3.1	Stress- strain curve of polymers.	39
Figure 3.2	Deformation of specimen during the test.	40
Figure 3.3	Load- deformation curve of a viscoelastic material. B= dissipated energy.	41
Figure 3.4	Main flow chart of the simulation.	42
Figure 3.5	Necking perform once in the simulation.	43
Figure 4.1	Schematic map of fracture mode.	84
Figure 4.2	Schematic of tensile test.	87
Figure 4.3	Schematic of stress-Strain curve.	88
Figure 4.4	Snapshots of the simulation at (a)0%, (b)100%, (c)200%,	92

	(d)400% elongation at 1.1 Tg with 5wt.% nanoplatelets.	
Figure 4.5	MD snapshots looking from x- axis direction at at (a)0%, (b)100%, (c)200%, (d)400% elongation 0.4 Tg, , and , with 5wt.% nanoplatelets	93
Figure 4.6	Force/area curves vs. distance with different contents of the nanoplatelets at 1.1 Tg.	94
Figure 4.7	Force/area curves vs. distance with different contents of the nanoplatelets at 0.4Tg.	95
Figure 4.8	Normalized work, $W^*$ , to failure with content of nanoplatelets at 1.1 Tg.	96
Figure 4.9	Normalized work, $W^*$ , to failure with content of nanoplatelets at 0.4Tg.	97
Figure 4.10	Schematic of polymer fracture. (a). The break of chemical bonds; (b). The mutual slippages between molecules; (c). The destroy of Van der Waals interactions between molecules or hydrogen bonds.	98
Figure 4.11	Profile chart of crack tip. If the elongation reaches the critical elongation, then the craze body will become crack. As the crack tip increases incessantly, the crack moves through the material.	101
Figure 4.12	Schematic of how the nanoplatelets stop crack as a barrier. In the figure, the crack was moving from the crack region. The nanoplatelet blocked the movement of crack on its way as a barrier.	102
Figure 4.13	Nanoplatelet – nanoplatelet correlation function, with 1wt.% nanoplatelets.	104
Figure 4.14	Nanoplatelet – nanoplatelet correlation function, with 3wt.% nanoplatelets.	104
Figure 4.15	Nanoplatelet – nanoplatelet correlation function, with 5wt.% nanoplatelets.	105

Figure 4.16	Force/ Area vs distance with different interactions between nanoplatelets (3wt.%) and polymer chains, where $\epsilon$ , $\sigma$ , and $\tau$ with the temperatures above $T_g$ , .	106
Figure 4.17	Force/ Area vs distance with different interactions between nanoplatelets (3wt.%) and polymer chains, where $\epsilon$ , $\sigma$ , and $\tau$ with the temperatures below $T_g$ , .	107
Figure 4.18	Normalilized work to failure, $W^*$ , as a function of the different interactions between nanoplatelets (3wt.%) and polymer chains, where $\epsilon$ , $\sigma$ , and the pulling velocity was at the temperature above $T_g$ , .	108
Figure 4.19	Normalilized work to failure, $W^*$ , as a function of the different interactions between nanoplatelets (3wt.%) and polymer chains, where $\epsilon$ , $\sigma$ , and the pulling velocity was at the temperature below $T_g$ , .	109
Figure 4.20	Pair correlation function of the Lennard-Jones liquid	110
Figure 4.21	Nanoplatelet – nanoplatelet correlation function, with interaction strength with 3wt.% nanoplatelets .	111
Figure 4.22	Nanoplatelet – nanoplatelet correlation function, with the interaction strength with 3wt.% nanoplatelets.	112
Figure 4.23	The force/area curves vs. distance with different relaxation times at $1.1 T_g$ .	113
Figure 4.24	The force/area curves vs. distance with different relaxation times at $0.4 T_g$ .	114
Figure 4.25	Normalized work, $W^*$ , to failure with relaxation time at $1.1 T_g$ with 3wt.% nanoplatelets.	115
Figure 4.26	Normalized work, $W^*$ , to failure with relaxation time at $0.4 T_g$ with 3wt.% nanoplatelets .	115
Figure 4.27	Nanoplatelet – nanoplatelet correlation function, with relaxation time with 3wt.% nanoplatelets.	116

Figure 4.28	Nanoplatelet – nanoplatelet correlation function, with relaxation time with 3wt.% nanoplatelets.	116
Figure 5.1	Schematic map of the necking in experiments and how simulation area actualize necking during the simulation by the periodic boundary condition. a. experiment sample, b. necking in experiment after tension, c. snapshot of original simulation area, d. snapshot of simulation area after simulation, e. how to understand the necking of the simulation area during the simulation by the periodic boundary condition.	125
Figure 5.2	Hysteresis curves for polymer nanocomposite with 0wt.% organoclay content, subjected to 100% strain	133
Figure 5.3	Hysteresis curves for polymer nanocomposite with 1wt.% organoclay content, subjected to 100% strain	133
Figure 5.4	Hysteresis curves for polymer nanocomposite with 3wt.% organoclay content, subjected to 100% strain	134
Figure 5.5	Hysteresis curves for polymer nanocomposite with 5wt.% organoclay content, subjected to 100% strain	134
Figure 5.6	Hysteresis curves for polymer nanocomposite with 0wt.% organoclay content, subjected to 50% strain	136
Figure 5.7	Hysteresis curves for polymer nanocomposite with 1wt.% organoclay content, subjected to 50% strain	136
Figure 5.8	Hysteresis curves for polymer nanocomposite with 3wt.% organoclay content, subjected to 50% strain	137
Figure 5.9	Hysteresis curves for polymer nanocomposite with 5wt.% organoclay content, subjected to 50% strain	137
Figure 5.10	Hysteresis curves for polymer nanocomposite with 0wt.% organoclay content, subjected to 200% strain	138
Figure 5.11	Hysteresis curves for polymer nanocomposite with 1wt.% organoclay content, subjected to 200% strain	138



Figure 5.12	Hysteresis curves for polymer nanocomposite with 3wt.% organoclay content, subjected to 200% strain	139
Figure 5.13	Hysteresis curves for polymer nanocomposite with 5wt.% organoclay content, subjected to 200% strain	139
Figure 5.14	Effect of organoclay content on dissipated energy in PU nanocomposites at 100% strain	140
Figure 5.15	Hysteresis curves for PU nanocomposites with 0wt.% organoclay content, subjected to 100% strain	143
Figure 5.16	Hysteresis curves for PU nanocomposites with 1wt.% organoclay content, subjected to 100% strain	143
Figure 5.17	Hysteresis curves for PU nanocomposites with 3wt.% organoclay content, subjected to 100% strain	144
Figure 5.18	Hysteresis curves for PU nanocomposites with 5wt.% organoclay content, subjected to 100% strain	144
Figure 5.19	Wide-angle x-ray diffraction patterns for C20-clay and PU/C20-clay nanocomposite (5Wt% C20)	145
Figure 5.20	Chain segment and coordinate system	146
Figure 5.21	Dissipated energy at 100% elongation	150
Figure 5.22	The permanent set occurred in each cycle.	151
Figure 5.23	Schematic map of the relationship between the unresumable dissipated energy and the resumable dissipated energy in the recyclic test	152
Figure 5.24	Dissipated energy of the 1st cycle of the polymer nanocomposites recyclic simulation versus nanoplatelets content at different deformations (50%, 100%, and 200%).	153
Figure 5.25	Effect of organoclay on the viscosity of polyol.	158
Figure 5.26	WAXD results under different stains.	161
Figure 5.27	Schematic diagram of d-spacing on nanoscale change during stretching.	162

Figure 5.28	Hysteresis curves for the PU/organoclay nanocomposites at 100% strain.	163
Figure 5.29	Effect of organoclay on dissipated energy	164
Figure 5.30	Effect of the organoclay on permanent set.	165
Figure 6.1	Fracture toughness vs. nanoparticles volume content for EP (epoxy) /Al <sub>2</sub> O <sub>3</sub> and EP/TiO <sub>2</sub> nanocomposites.	171
Figure 6.2	The effects of MWCNTs loading content (wt.%) on the mechanical performances of CNTs/epoxy composites: fracture strain.	172
Figure 6.3	Schematic map of the nanoparticles model with a cut- off radius. O is the centre of the nanoparticles sphere, R <sub>p</sub> is the radius of nanoparticles sphere, r <sub>pc</sub> is cut- off radius of nanoparticles. OA, OB and OC are the radius of nanoparticles sphere, AA', BB' and CC' are the cut- off radius in the direction of OA, OB and OC, respectively.	175
Figure 6.4	Schematic map of the calculation of the distance between a nanoplatelet and a monomer of a neighboring polymer chain, $r_{pm}$ .	177
Figure 6.5	Schematic map of a nanotube model.	178
Figure 6.6	Schematic map of the calculation of Lt. O and O' are the centres of two nanotube cross sections, respectively. R <sub>t</sub> is radius of the nanotube cross section, Lt is the length of nanotube.	178
Figure 6.7	The Schematic map of the calculation of the distance between a nanotube and a monomer (or segment) of a neighbouring polymer chain, $r_{tm}$ .	180
Figure 6.8	The force/area curves vs. distance with different geometry of the nanofillers at 1.1T <sub>g</sub> .	181
Figure 6.9	The force/area curves vs. distance with different geometry of the nanofillers at 0.4T <sub>g</sub> .	182

Figure 6.10	The normalized work, $W^*$ , to failure with different geometry of the nanofillers at 0.4Tg.	183
Figure 6.11	The normalized work, $W^*$ , to failure with different geometry of the nanofillers at 1.1Tg.	183
Figure 6.12	The relationships of $r_{fm}$ , $r_{pm}$ and $r_{tm}$ , when	184
Figure 6.13	Nanoparticle – nanoparticle correlation function, with 3wt.% content of nanoparticle.	186
Figure 6.14	Nanoplatelet – nanoplatelet correlation function, with 3wt.% content of nanoplatelets.	186
Figure 6.15	Nanotube – nanotube correlation function, with 3wt.% content of nanotubes.	187
Figure 7.1	The force/area curves vs. distance with content of the nanoplatelets at 0.4Tg.	190
Figure 7.2	Dissipated energy vs. content of nanoplatelets at 100% elongation.	191
Figure 7.3	The normalized work, $W^*$ , to failure with different geometries of the nanofillers at 0.4Tg.	192

## LIST OF TABLES

Table 1.1	The result of nanofillers used to enhance the mechanical properties of polymers.....	4
Table 2.1	Lennard-Jones reduced units.....	25
Table 5.1	Details of 4, 4'- methylenebis (cyclohexyl isocyanate).....	126
Table 5.2	Reactivity of HMDI relative to IDI, MDI. HDI and IPDI.....	126
Table 5.3	Details of modified MDI.....	127
Table 5.4	Details of polyether polyol.....	128
Table 5.5	Details of 1,4-Butanediol.....	128
Table 5.6	Details of Cloisite 20A.....	129
Table 5.7	Details of Cloisite 30B.....	130
Table 5.8	Simulation results of dissipated energy in the polymer nanocomposites.....	142
Table 5.9	Variation of orientation factor (5wt.% nanoclay).....	152
Table 5.10	WAXD results for the stretching test of PUE-organoclay (5% by weight).....	162

## LIST OF SYMBOL

$\tau$	the simulation time
$N_T$	the total number of time steps in the simulation
$t$	the index which runs over the time steps from 1 to $N_T$
$A(t)$	the instantaneous value of A
$V(t)$	the instantaneous potential energy at time $t$ ,
$ r_i(t) - r_j(t) $	the distance between $i$ and $j$
$m_i$	the mass of the particle $i$
$v_i(t)$	the instantaneous velocity of particle $i$ at time
$E(t)$	Total energy
$E_{kin}(t)$	the instantaneous kinetic energy
$T(t)$	the instantaneous temperature
$N$	the total numbers of particles in the system
$k_B$	the Boltzmann constant, $k_B = 1.3806505(24) \times 10^{-23} \text{ J/K}$
$r_i$	the position of particle $i$
$F_i^{TOT}$	the total force acting on particle $i$
$D$	the dimensionality of the system (2 or 3) pp.12
$F_i$	the internal force (arising from the intermolecular interactions)
$F_i^{EXT}$	the external force exerted by the container's walls
MSD	The mean square displacement
$D$	diffusion coefficient pp.15
$g(r)$	the pair correlation function
$a_i$	the acceleration of the particle, $a_i = \frac{d^2 r_i}{dt^2}$
$L$	Lagrangian function
$H$	Hamiltonian function
$p_i$	a component of the momentum of particle $i$

$\vec{r}_i$	the position of the particle
$\vec{v}_i$	the velocities of the particle
$\vec{a}_i$	the acceleration of the particle
$\varepsilon$	the characteristic of the well depth,
$\sigma$	the length scale
$r_c$	the cut-off radius
O	the centre of the nanoparticles sphere
$R_p$	the radius of nanoparticles sphere
$r_{pc}$	cut- off radius of nanoparticles
A	the surface area of the nanoplatelet model
l	the length of nanoplatelet model
A'	the surface area of nanoparticles model
$R_t$	radius of the nanotube cross section
$L_t$	the length of nanotube
$V_{pm}(r)$	Lennard- Jones potential between a nanoplatelet and a monomer of a neighboring polymer chain,
	the distance between nanoplatelet and the monomer of a polymer
$r_{pm}$	chain, the $r_{pm}$ are considered as $r_{pm} = \frac{r_{pmA} + r_{pmB} + r_{pmC} + r_{pmD}}{4}$
$r_{pmc}$	the cut- off radius between a nanoplatelet and a monomer of a neighboring polymer chain
$\varepsilon_{pm}$	characteristic energy between a nanoplatelet and a monomer of a neighboring polymer chain
$V_{tm}(r)$	Lennard- Jones potential between a nanotube and a monomer of a neighboring polymer chain
	the distance between nanotube and the monomer of a polymer
$r_{tm}$	chain, the $r_{tm}$ are considered as $r_{tm} = \frac{r_{tmA} + r_{tmB}}{2}$
$r_{tmc}$	is the cut- off radius between a nanotube and a monomer of a neighboring polymer chain
$\varepsilon_{tm}$	characteristic energy between a nanotube and a monomer of a neighboring polymer chain

## CHAPTER 1

### INTRODUCTION AND AIMS OF PROJECT

#### 1.1 INTRODUCTION

In the last decade, nanostructured materials have excited considerable interest in the materials research community partly due to their potentially remarkable mechanical properties. In particular, layered silicate (montmorillonite clay)-reinforced polymer composites have shown great promise [1].

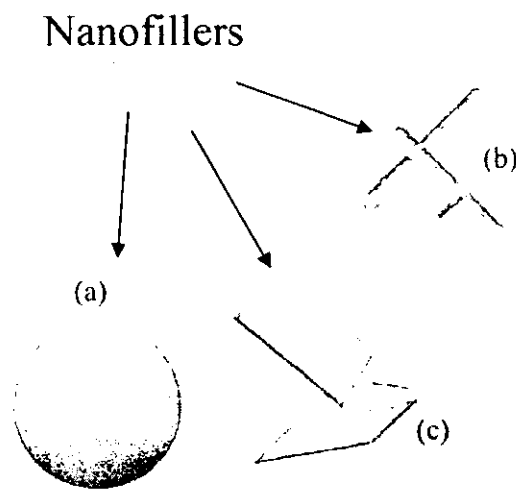


**Figure 1.1** Schematic of the three types of nanofillers.

Polymer nanocomposite is a new class of composites prepared by using nanotechnology, which are polymer reinforced with small quantities (normally less than 5% by weight) of different nanofillers. Both thermoset and thermoplastic polymers have been incorporated with the nanofillers into nanocomposites [2], which including polypropylene [3], polyethylene [4], polystyrene [5], poly(vinyl chloride) [6], polyurethane [7], epoxy [8], nylon [9], rubber [10], recycled poly(ethylene

terephthalate) [11], and so on. There are hundreds kinds of nanofillers which polymers can fill with. Hence three major types of nanofillers can be distinguished depending on how many dimensions of the dispersed nanofillers are in the nanometer range (shown in Figure 1.1).

Layered silicate is one of the most commonly used nanofillers. Only one dimension in the nanometer range is the characteristic of this nature of nanofillers. Nanofillers in this family is present in the form of sheets of one to a few nanometer thick to hundreds to thousands nanometers long. The feasibility of sort of nanofillers reinforcing with polymer are widely investigated because the starting clay materials are easily available [12, 13].

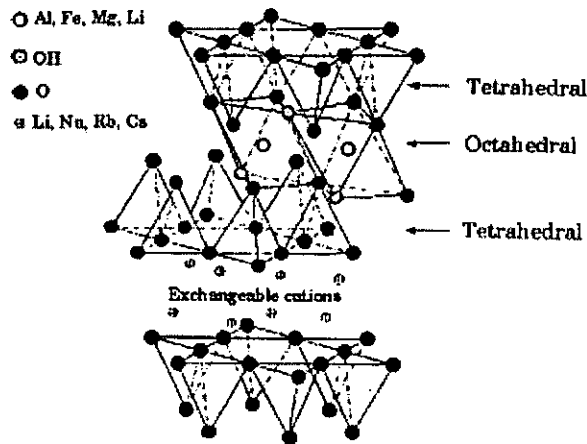


**Figure 1.2** Structure of 2:1 phyllosilicates. [14]

The layered silicates such as montmorillonite (MMT), hectorite and saponite commonly used in nanocomposites belong to the structural family known as the 2:1 phyllosilicates. Their crystal lattice consists of two-dimensional layers where a central octahedral sheet of alumina or magnesia is fused to two external silica tetrahedron by the tip so that the oxygen ions of the octahedral sheet do also belong to the tetrahedral sheets (Figure 1.2.).



According to the nature of the components used and the method of preparation, two main types of nanocomposites may be obtained when nanofillers are associated with a polymer (shown in Figure 1.3): Intercalated nanocomposite, and exfoliated nanocomposite.

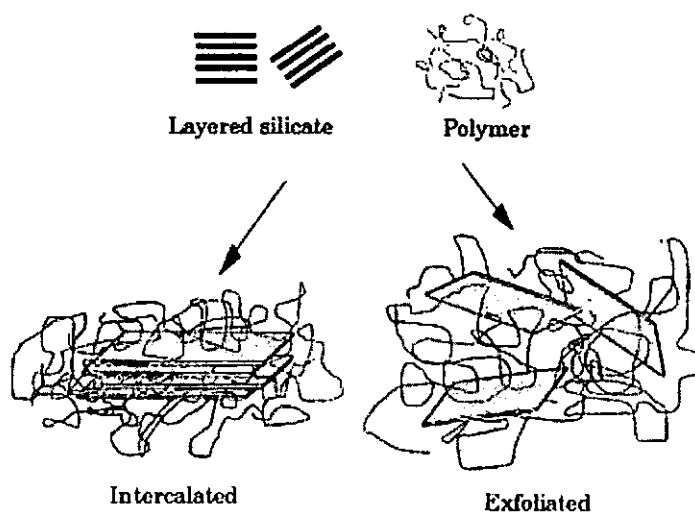


**Figure 1.3** Scheme of two different types of nanocomposite arising from the interaction of layered silicates and polymers: (a) intercalated nanocomposite and (b) exfoliated nanocomposite.

The nanocomposites offer attractive potential for diversification and application over traditional polymers. The many useful properties of polymers such as mechanical properties, thermal stability and barrier properties can be built by incorporation of only small amount of nano-sized organoclay into polymer hosts [1, 15-18]. Compared with pure polymer or conventional composites, the nanocomposites have higher modulus [1, 15, 16], greater strength [17], longer fatigue durability [18], higher heat resistance [1, 17] and lower gas permeability [19], better flame retardancy [20,21] and etc.

Simulation has become one of most general method in scientific and engineering studies, applications can be found physics, chemistry, biochemistry, materials science, and in branches of engineering, etc. Molecular dynamics simulation is one kind of simulations which provides the methodology for detailed microscopic modelling on the molecular scale.

**Table 1.1** The result of nanofillers used to enhance the mechanical properties of polymers.

Polymer Matrix	Polyurethane	Epoxy	Nylon 6	polypropylene	poly(vinyl chloride)	polystyrene	rubber
Enhancement of Mechanical Properties	✓	×	✓	✓	×	×	✓
Tg (°C)	-45	150	40	-10	80	100	-60~90

The addition of clay cannot enhance the properties effectively for all polymers, in fact. It can be found in Table 1.1. that the nanofillers are always working for the enhancement of the mechanical properties for these polymers, which Tgs are lower than room temperature or near by (or equal to) room temperature, such as nylon. However, for these polymers, which Tgs are higher than room temperature, the addition of the clay is not working well for toughening these polymers. The question is why clay is always working for the improvement of the mechanical properties of those polymers, which Tgs are lower than room temperature such as polyurethane [7] and rubbers [10] or near by (or equal to) room temperature, such as nylon [9], and not working well for the improvement of toughness of those polymers, which Tgs are higher than room temperature such as epoxy [8] and polystyrene [5]. In addition, under what kinds of conditions, organoclay can enhance the toughness of epoxy and polystyrene. Moreover, it is found in experiments that the addition of organoclay can also enhance the cyclic fatigue property [18]. However, the details of information concerning how and why the incorporation of organoclay can improve the fatigue durability of some polymers is still not clear yet. The mechanisms controlling the total

fatigue life of polymers vary with many morphological, thermal, mechanical and environmental factors [22-24]. Therefore, the research into the deformation and fracture of polymer nanocomposites by fatigue is significantly important for their certain applications. Due to the limitation of the experiments conditions and economic reasons, we attempt to answer the questions by means of computer simulation in this research thesis.

## 1.2 OBJECTIVES OF THE PROJECT

As we mentioned above, the objectives of this project are:

- Programme development of molecular dynamics simulation in polymer/clay nanocomposite.
- Investigation of mechanism of fracture in polymer clay nanocomposite by computer simulation.
- Investigation of energy dissipation in polymer clay nanocomposite.
- Investigation of the effect of nanofiller dimension on fracture.

## REFERENCE

1. S.S. Ray, M. Okamoto, *Progress in Polymer Science.*, **28**, 1539 (2003).
2. P. C. LeBaron, Z. Wang, T. J. Pinnavaia, *Appl. Clay. Sci.*, **15**, 11 (1999).
3. M. C. Koo, M. J. Kim, M. H. Choi, S. O. Kim, I. J. Chung, *J. Appl. Polym. Sci.*, **88**, 1526 (2003).
4. B.Liao, M.Song, H.Liang, Y.X.Pang, *Polymer*, **42**, 10007 (2001).
5. B. Hoffmann, C.Dietricha, R.Thomann, C.Friedrich, R.Mulhaupt, *Macromol. Rapid. Commun.*, **21**, 57 (2000).

6. H. Haiyan, P. Mingwang, L. Xiucuo, S. Xudong, Z. Liucheng, *Polymer. Internatioanl.*, **53**, 225 (2004).
7. K. J. Yao, M. Song, D. J. Hourston, D. Z. Luo, *Polymer*, **43**, 1017 (2002).
8. J. H. Park, S. C. Jana, *Macromolecules*, **36**, 2758 (2003).
9. T. D. Fornes, P. J. Yoon, H. Keshkula, D. R. Paul, *Polymer*, **42**, 9929 (2001).
10. M. Song, C. W. Wong, J. Jin, M. A. Ansarifar, Z. Y. Zhang, M. Richardson, *Polymer. International.*, **54**, 560 (2005).
11. A. Pegoretti, J. Kolarik, C. Peroni, C. Migliaresi, *Polymer*, **45**, 2751 (2004).
12. M. Ogawa, K. Kuroda, *Bull. Chem. Soc. Jpn.*, **70**, 2593 (1997).
13. B.K.G. Theng, *The Chemistry of Clay-Organic Reactions*, Wiley, New York (1974).
14. E. P. Giannelis, R. Krishnamoorti, E. Manias, *Adv. Polym. Sci.*, **118**, 108 (1999).
15. E. P. Gianneils, *Adv. Mater.*, **8**, 29 (1996).
16. M. Biswas, R. S. Sinha, *Adv. Polym. Sci.*, **155**, 167 (2001).
17. E. P. Giannelis, *Appl. Organomet. Chem.*, **12**, 675 (1998).
18. K.J. Yao, *High Performance Polyurethane-Organoclay Nanocomposites*, **PhD thesis**, Loughborough University. 2005.
19. M. A. Osman, V. Mittal, M. Morbidelli, U. W. Suter, *Macromolecules*, **36**, 9851 (2003).
20. J.W. Gliman, C. L. Jackson, A. B. Morgan, Harris R. *Chem. Mater.*, **12**, 1866 (2000).
21. M. Alexander, G. Beyer, C. Henrist, R. Cloots, A. Rulmont, R. Jerome, P. Dubois, *Macromol. Rapid. Commun.*, **22**, 643 (2001).
22. J. Schijve, *Fatigue of Structure and Materials*, **Kluwer Academic Publishers**, 2001.
23. H. J. Qi, M. C. Boyce, *Mechan. Mater.*, **37**, 817 (2005).
24. E. M. Christenson, J. M. Anderson, A. Hiltner, E. Baer, *Polymer*, **46**, 11744 (2005).

## CHAPTER 2

### PRINCIPLE OF MOLECULAR DYNAMICS SIMULATION

#### 2.1 INTRODUCTION

Computer simulations play a crucial role in science research today. In the past, the theories were always summarized by a series of experiments; on the other hand, it was also used to instruct the experiments. But it seems that this traditional research method is upset down by the computer experiments, due to its inimitable advantage. Computer simulations cannot only be used to understand and interpret the experiments at the microscopic level, but also to solve some problems which are not accessible experimentally, or which experiments would stupendous expensive, such as under extremely high/ low pressure or extremely high/ low temperature (shown in Figure 2.1) [1]

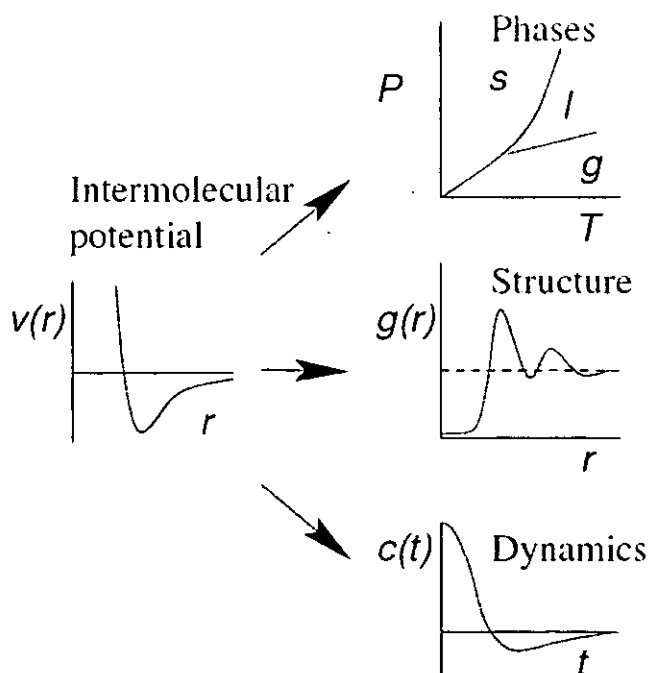


**Figure 2.1** The sketch map of what the computer simulations can do.

Furthermore, the computer simulations can offer a great thing over conventional experiments - thought experiments, which allow the computer simulator to perform an experiment which is just impossible to do in reality, but whose outcome greatly increases our understanding of phenomena.

Molecular dynamics (MD) simulation is one of the most popular used computer simulation methods, particularly well suited to model macromolecular systems because of the generality of the algorithm, which is integrate the motion equations of a set of interacting particles/ molecules by using the laws of classical mechanics, then time evolve them. Molecular dynamics differs by being deterministic, completely determined by its present state [2]. Due to the characteristics of nanocomposites, it is very difficult to understand what actually happened inside the materials in molecular level. Scientists engaged in studying matter at this level require computational tools to allow them to follow the movement of individual molecules .

## **2.2 STATISTICAL MECHANICS**

In order to relate the microscopic molecules motion of the simulations to the classical mechanics, such as stress, strain, elongation, etc, the statistical mechanics are introduced. It is considered that the classical mechanics are ensemble behaviour of a mount of its components- called as macro states. For each macro state, there are many corresponding microstates, which are formed from the product of a single many-particle state.

### **2.2.1 Time average of physical properties**

Measuring a quantity in molecular dynamics is always instead of a time averages value of physical properties over the system trajectory. Physical properties are usually a function of the particle coordinates and velocities [3]. So, for instance, one can define the instantaneous value of a generic physical property A at time t:

$$A(t) = f(r_1(t), \dots, r_N(t), v_1(t), \dots, v_N(t)) \quad (2.1)$$

And then, obtain their average:

$$\langle A \rangle = \lim_{\tau \rightarrow \infty} \frac{1}{\tau} \int_0^\tau A(t) dt = \frac{1}{N_T} \sum_{t=1}^{N_T} A(t) \quad (2.2)$$

Where  $\tau$  is the simulation time,

$N_T$  is the total number of time steps in the simulation,

$t$  is the an index which runs over the time steps from 1 to  $N_T$ , and

$A(t)$  is the instantaneous value of  $A$ .

$A(t)$  is calculated at each time step by the MD program while running. The sum  $\sum_t A(t)$  is also updated at each step. At the end of the run the average is immediately obtained by dividing by the number of steps.

### 2.2.2 Potential energy

Potential energy is energy which results from position or configuration. Consider one particle  $i$  in the system. Every other particle  $j$  attracts or repels it. The interaction at time  $t$  depends on the positions of the particles  $i$  and  $j$  [1, 4, 5]. It can be described by the following equation:

$$V(t) = \sum_i \sum_{j>i} U(|r_i(t) - r_j(t)|) \quad (2.3)$$

Where  $V(t)$  is the instantaneous potential energy at time  $t$ ,

$|r_i(t) - r_j(t)|$  is the distance between  $i$  and  $j$ .

### 2.2.3 Kinetic energy

The kinetic energy of an object is the extra energy which it possesses due to its motion. It is defined as the work needed to accelerate a body of a given mass from rest to its current velocity. Having gained this energy during its acceleration, the body maintains this kinetic energy unless its speed changes. Negative work of the same magnitude would be required to return the body to a state of rest from that velocity. The instantaneous kinetic energy can be described by:

$$E_{kin}(t) = \frac{1}{2} \sum_i m_i (v_i(t))^2 \quad (2.4)$$

Where  $E_{kin}(t)$  is the instantaneous kinetic energy of particle  $i$  at time  $t$ ,

$m_i$  is the mass of the particle  $i$ , and

$v_i(t)$  is the instantaneous velocity of particle  $i$  at time.

#### 2.2.4 Total energy

The total energy of the system at time  $t$  is the summation of the quantity of instantaneous potential energy and kinetic energy at time  $t$ , which is described by:

$$E(t) = E_{kin}(t) + V(t) \quad (2.5)$$

#### 2.2.5 Temperature

Temperature is one of the principal parameters of thermodynamics. The temperature of a system is related to the average energy of microscopic motions in the system. The instantaneous temperature is related to the instantaneous kinetic energy directly. It can be calculated from the following equation:

$$E_{kin}(t) = \frac{3}{2} N k_B T(t) \quad (2.6)$$

Therefore,



$$T(t) = \frac{2}{3} \cdot \frac{E_{kin}(t)}{Nk_B} \quad (2.7) [2]$$

Where  $E_{kin}(t)$  is the instantaneous kinetic energy,

$T(t)$  is the instantaneous temperature,

$N$  is the total numbers of particles in the system, and

$k_B$  is the Boltzmann constant,  $k_B = 1.3806505(24) \times 10^{-23} J/K$ .

### 2.2.6 Pressure

In 1738, Swiss physician and mathematician Daniel Bernoulli published *Hydrodynamica* which laid the basis for the kinetic theory of gases. In this work, Bernoulli positioned the argument, still used to this day, that gases consist of great numbers of molecules moving in all directions, that their impact on a surface causes the gas pressure that we feel, and that what we experience as heat is simply the kinetic energy of their motion. The Clausius virial function is introduced in order to present the measurement of the pressure in a molecular dynamics simulation.

$$W(r_1, \dots, r_N) = \sum_{i=1}^N r_i \cdot F_i^{TOT} \quad (2.8)$$

Where  $r_i$  is the position of particle  $i$ ,

$F_i^{TOT}$  is the total force acting on particle  $i$ .

Then its statistical average over the molecular dynamics trajectory is:

$$\langle W \rangle = \lim_{t \rightarrow \infty} \frac{1}{t} \int_0^t d\tau \sum_{i=1}^N r_i(\tau) \cdot m_i \ddot{r}_i(\tau) \quad (2.9)$$

Integrating by parts:

$$\langle W \rangle = \lim_{t \rightarrow \infty} m_i \sum_{i=1}^N \frac{\dot{r}_i(t) \cdot \dot{r}_i(t) - \dot{r}_i(0) \cdot \dot{r}_i(0)}{t} - \lim_{t \rightarrow \infty} \frac{1}{t} \int_0^t d\tau \sum_{i=1}^N r_i(\tau) \cdot m_i |\dot{r}_i(\tau)|^2 \quad (2.10)$$

If the system is localized in a finite region of space and particles are not accelerating to infinity, then:

$$\lim_{t \rightarrow \infty} m_i \sum_{i=1}^N \frac{\dot{r}_i(t) \cdot \dot{r}_i(t) - \dot{r}_i(0) \cdot \dot{r}_i(0)}{t} = 0 \quad (2.11)$$

Therefore:

$$\langle W \rangle = - \lim_{t \rightarrow \infty} \frac{1}{t} \int_0^t d\tau \sum_{i=1}^N r_i(\tau) \cdot m_i |\dot{r}_i(\tau)|^2 \quad (2.12)$$

By the equipartition law of statistical mechanics:

$$\langle W \rangle = -DNk_B T \quad (2.13)$$

Where  $D$  is the dimensionality of the system (2 or 3),

$N$  the number of particles, and

$k_B$  is the Boltzmann constant.

The total force acting on a particle as composed of two contributions:

$$F_i^{TOT} = F_i + F_i^{EXT} \quad (2.14)$$

Where  $F_i$  is the internal force (arising from the intermolecular interactions), and

$F_i^{EXT}$  is the external force exerted by the container's walls.

Pressure (P) can be defined by considering a system enclosed in a parallelepipedic container with sides  $L_x$ ,  $L_y$ , and  $L_z$ , where volume  $V = L_x L_y L_z$  (shown in Figure 2.2).

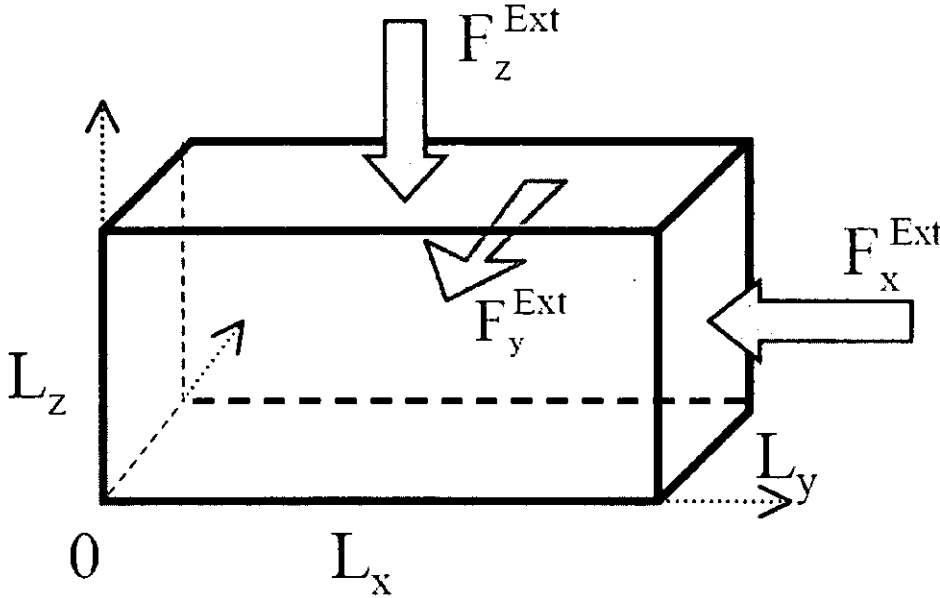


Figure 2.2 A schematic of the loading external force.

The total virial function can be written as a sum of internal and external virials:

$$\langle W^{TOT} \rangle = \langle W^{INT} \rangle + \langle W^{EXT} \rangle = -DNk_B T \quad (2.15)$$

The external part of the virial function for a container with coordinate origin on one of its corners can be described by:

$$\langle W^{EXT} \rangle = L_x (-PL_y L_z) + L_y (-PL_x L_z) + L_z (-PL_x L_y) = -DPV \quad (2.16)$$

Where  $-PL_y L_z$  is the external force  $F_x^{EXT}$  applied by the  $yz$  wall along the  $x$

directions to particles located at  $x=L_x$ .

Therefore the equation 2.15 can be written:

$$\left\langle \sum_{i=1}^N r_i \cdot F_i \right\rangle - DPV = -DNk_B T \quad (2.17)$$

or

$$PV = Nk_B T + \frac{1}{D} \left\langle \sum_{i=1}^N r_i \cdot F_i \right\rangle \quad (2.18)$$

This equation is known as the virial equation. All the quantities except the pressure  $P$  are easily accessible in a simulation, and therefore measure  $P$  become possible.

In the case of Lennard-Jones potential  $V(r)$ , the equation 2.18 becomes:

$$PV = Nk_B T + \frac{1}{D} \left\langle \sum_i \sum_{j>i} r_{ij} \frac{dV}{dr} \bigg|_{r_{ij}} \right\rangle \quad (2.19)$$

This expression has the additional advantage over equation 2.18 to be naturally suited to be used when periodic boundary conditions are present: it is sufficient to take them into account in the definition of  $r_{ij}$ .

### 2.2.7 Mean square displacement

In a molecular system, all the monomers in each molecular undertaking a random walk. From a given starting position, what distance are we likely to travel after many steps? This can be determined simply by adding together the steps, taking into

account the fact that steps backwards subtract from the total, while steps forward add to the total. Since both forward and backward steps are equally probable, we come to the surprising conclusion that the probable distance travelled sums up to zero! This is clearly a useless property to calculate (though it is perhaps a warning to drunkards). The mean square displacement (msd) is a measure of the average distance a molecule travels. The mean square displacement (MSD) of particles in a simulation can be described by its definition:

$$MSD = \langle |r(t) - r(0)|^2 \rangle \quad (2.20)$$

where  $\langle \dots \rangle$  denotes here averaging over all the atoms.

The “jumps” of particles to refold them into the box must be avoided when using periodic boundary conditions as contributing to diffusion.

The MSD contains information on the atomic diffusivity. If the system is solid, MSD saturates to a finite value, while if the system is liquid, MSD grows linearly with time. In this case it is useful to characterize the system behavior in terms of the slope, which is the diffusion coefficient  $D$ :

$$D = \lim_{t \rightarrow \infty} \frac{1}{6t} \langle |r(t) - r(0)|^2 \rangle \quad (2.21)$$

Number 6 in the above equation must be replaced by number 4 in two-dimensional systems.

### 2.2.8 Real space correlations

Real space correlation functions are typically of the form:  $\langle A(r)A(0) \rangle$  and are straightforward to obtain by molecular dynamics: one has to compute the quantity of

interest  $A(r)$  starting from the particle positions and velocities for several configurations, construct the correlation function for each configuration, and average over the available configurations.

The simplest example is the pair correlation function  $g(r)$ , which is essentially a density-density correlation.  $g(r)$  is the probability to find a pair a distance  $r$  apart, relative to what expected for a uniform random distribution of particles at the same density:

$$\rho g(r) = \frac{1}{N} \left\langle \sum_{i=1}^N \sum_{\substack{j=1 \\ (j \neq i)}}^N \delta(r - r_{ij}) \right\rangle \quad (2.22)$$

This function carries information on the structure of the system. For a crystal, it exhibits a sequence of peaks at positions corresponding to shells around a given atom. The positions and magnitude of the peaks are a ‘signature’ of the crystal structure (fcc, hcp, bcc, ...) of the system. For a liquid,  $g(r)$  exhibits its major peak close to the average atomic separation of neighbouring atoms, and oscillates with less pronounced peaks at larger distances. The magnitude of the peaks decays exponentially with distance as  $g(r)$  approaches 1. In all cases,  $g(r)$  vanishes below a certain distance, where atomic repulsion is strong enough to prevent pairs of atoms from getting so close.

One quantity often computed from  $g(r)$  is the average number of atoms located between  $r_1$  and  $r_2$  from a given particle,

$$\rho \int_{r_1}^{r_2} g(r) 4\pi r^2 dr \quad (2.23)$$

This allows defining coordination numbers also in situations where disorder is present.

The calculation of  $g(r)$  is intrinsically a  $O(N^2)$  operation, and therefore it can slow down considerably an optimized molecular dynamics program. If the behaviour at large  $r$  is not important, it might be convenient to define a cut-off distance, and use techniques borrowed from fast force calculations using short-ranged potentials to decrease the computational burden. It should also be noted that periodic boundary conditions impose a natural cut-off at  $L/2$ , where  $L$  is the minimum between the box sizes  $L_x, L_y, L_z$  in the three directions. For larger distance the results are spoiled by size effects.

## 2.3 EQUATIONS OF MOTION

In physics, equations of motion are equations that describe the behaviour of a system (e.g., the motion of a particle under an influence of a force) as a function of time. The equations of motion in molecular dynamics simulation are based on Newton's law:

$$F_i = m_i a_i \tag{2.24}$$

Where  $m_i$  is the mass of the particle,

$$a_i \text{ is the acceleration of the particle, } a_i = \frac{d^2 r_i}{dt^2}.$$

### 2.3.1 Lagrangian function

In the MD simulation system,  $N$  particles is described by using  $3N$  independent generalized coordinates  $q_i$  and  $3N$  velocities  $\dot{q}_i$ . The potential only depends on the positions  $q_i$ . The lagrangian function  $\mathcal{L} = \mathcal{L}(\{q_i\}, \{\dot{q}_i\}, t)$  is defined as:

$$\mathcal{L} = \mathcal{L}(\{q_i\}, \{\dot{q}_i\}, t) = E_{kin}(\{q_i\}, \{\dot{q}_i\}) - V(\{q_i\}) \quad (2.25)$$

Therefore, the equations of motion of the system in lagrangian form are:

$$\frac{d}{dt} \left( \frac{\partial \mathcal{L}}{\partial \dot{q}_i} \right) - \frac{\partial \mathcal{L}}{\partial q_i} = 0 \quad i = 1, 2, \dots, N \quad (2.26)$$

For the case of a set of spherical particles with equal mass moving in Cartesian coordinates with components  $q_i$  one obtains:

$$\mathcal{L} = \frac{1}{2} m \sum_i \dot{q}_i^2 - U(\{q_i\}) \quad (2.27)$$

Where  $m$  is the mass of the particle.

Therefore:

$$m\ddot{q}_i = -\frac{\partial U(\{q_i\})}{\partial q_i} = F_i \quad (2.28)$$

### 2.3.2 Hamiltonian function

Hamiltonian function is an alternative formulation of the equations of motion .The definition of the Hamiltonian function:

$$\mathcal{H} = \sum_i p_i \dot{q}_i - \mathcal{L} \quad (2.29)$$

Where  $p_i$  is a component of the momentum of particle  $i$ .

The equations of motion in the Hamiltonian form can be written as:



$$\frac{\partial \mathcal{H}}{\partial p_i} = \dot{q}_i \quad (2.30)$$

Therefore, integrate Newton's law, two key quantities in the molecular dynamics simulation can be obtained:

$$\begin{cases} d\vec{r}_i = \vec{v}_i dt \\ d\vec{v}_i = \vec{a}_i dt \end{cases} \quad (2.31)$$

Where  $\vec{r}_i$  is the position of the particle,

$\vec{v}_i$  is the velocities of the particle, and

$\vec{a}_i$  is the acceleration of the particle.

## 2.4 INTERMOLECULAR POTENTIALS AND FORCE CALCULATION

In molecular dynamics forces are derived from a potential energy function  $V$ , which depend on the particle coordinates:

$$F_i = -\nabla U(r_1, \dots, r_N) \quad (2.32)$$

From the classical equations of motion, a simple atomic system may be written:

$$U(r_1, \dots, r_N) = \sum_i \sum_{j>i} V(|r_i - r_j|) \quad (2.33)$$

The Lennard-Jones potential is a typical pairwise potential and probably the most commonly used one.

### 2.4.1 Lennard-Jones potential and its force calculation

#### a) Lennard-Jones potential

Neutral atoms and molecules are subject to two distinct forces in the limit of large distance and short distance: an attractive force at long ranges (van der Waals force, or dispersion force) and a repulsive force at short ranges. The Lennard-Jones potential is a simple mathematical model that represents this behavior. It was proposed in 1931 by John Lennard-Jones of Bristol University. The Lennard-Jones potential describes the Van der Waals interactions by using an attractive as two uncharged particle approach each other from a distance,  $r$  (shown in Figure 2.3) [6-13].

The change of the distance result these interactions attractively or repulsively is described by the following equation:

$$V_L = 4\varepsilon \left[ \left( \frac{\sigma}{r} \right)^{12} - \left( \frac{\sigma}{r} \right)^6 \right] \quad (2.34)$$

Where  $\varepsilon$  is the characteristic of the well depth,

$\sigma$  is the length scale,

the equilibrium distance of a pair molecules is  $r_0 = 2^{1/6} \sigma \approx 1.122\sigma$ .

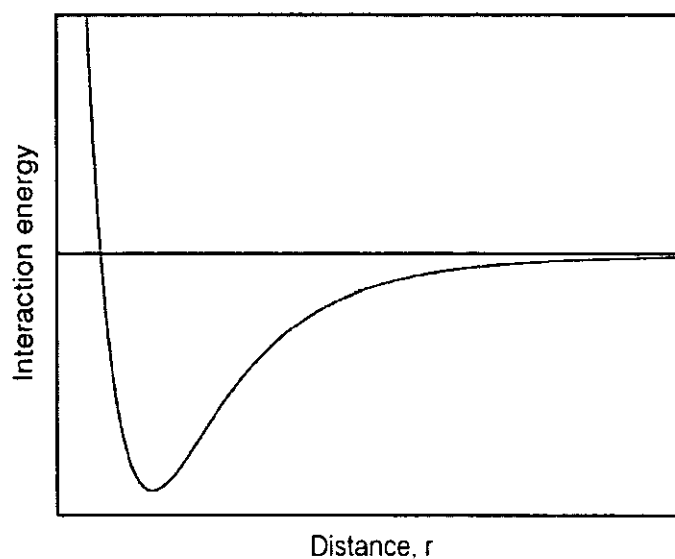
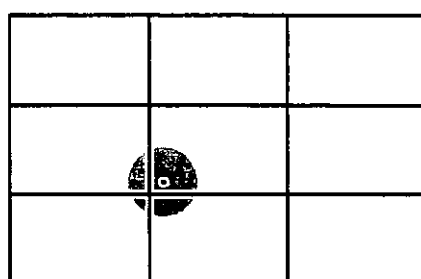
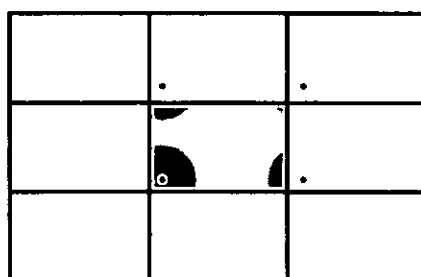


**Figure 2.3** The curve of Lennard-Jones potential.



(a)



(b)

**Figure 2.4** A sketch of periodic boundary condition (a) cut-off sphere in conventional way; (b) cut-off sphere partitioned under periodic boundary condition.

In order to reduce the computational work, the potential is always cut off at a distance

$r_c$  and set the potential to zero beyond that point (shown in Figure 2.4).

The Lennard-Jones potential with a cut-off radius (shown in Figure 2.5) is described by the following equation:

$$V_{LJ}(r) = \begin{cases} 4\epsilon \left[ \left( \frac{\sigma}{r} \right)^{12} - \left( \frac{\sigma}{r} \right)^6 \right] & r < r_c \\ 0 & r \geq r_c \end{cases} \quad (2.35)$$

Where  $\epsilon$  is the characteristic of the well depth,

$\sigma$  is the length scale,

the equilibrium distance of a pair molecules is  $r_0 = 2^{1/6}\sigma \approx 1.122\sigma$ , and

$r_c$  is the cut-off radius.

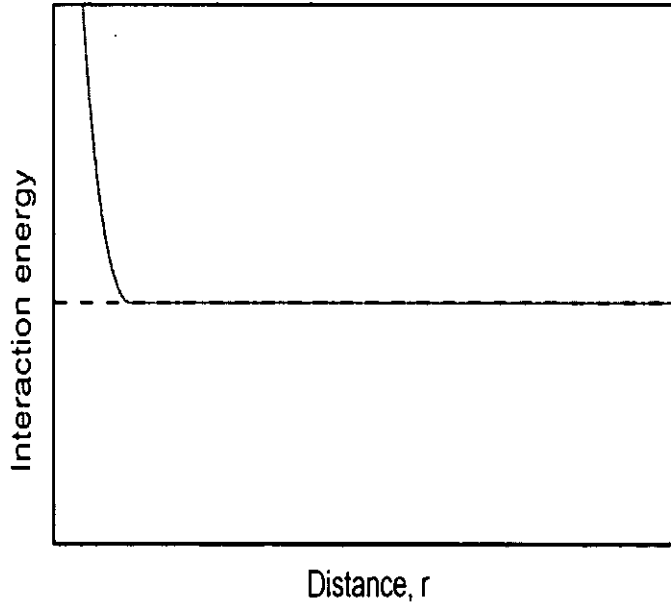


**Figure 2.5** The curve of Lennard-Jones potential with cut-off radius.

If the cut-off distance is large enough, the truncation error for each pair interaction will be minimal. But on the other hand, the number of interactions approximated by zero may be quite large and this may result an error in the total energy.

**b) Force calculation**

The force caused by Lennard-Jones potential is:

$$F_{LJ} = -\nabla V_{LJ}(r) = \frac{24\varepsilon}{\sigma^2} \left[ 2\left(\frac{\sigma}{r}\right)^{14} - \left(\frac{\sigma}{r}\right)^8 \right] \cdot \vec{r} \quad (2.36)$$

**2.4.2 Finitely-extensible non-linear elastic (FENE) potential and force calculation****a) FENE potential**

In polymer simulations, FENE potential is always used to join the neighbouring monomers in the same polymer chain, in order to ensure that the polymer chains cannot cross each other [14-22] (shown in Figure 2.6).

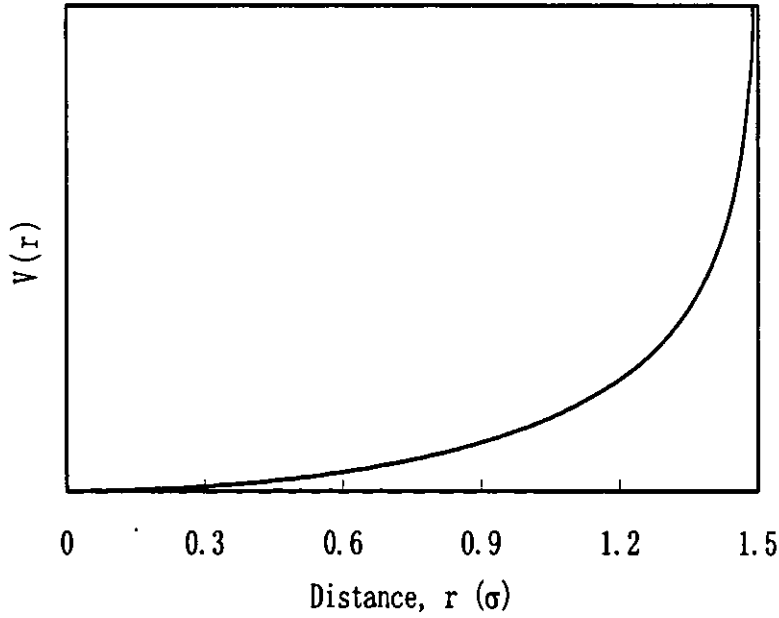


**Figure 2.6** The curve of FENE potential

The FENE potential can be described by the following equation:

$$V_{FENE}(r) = \begin{cases} -0.5kR_0^2 \ln(1 - (r/R_0)^2) & r < R_0 \\ \infty & r \geq R_0 \end{cases} \quad (2.37)$$

Where  $R_0$  is a finite extensibility, and  
 $k$  is a spring constant.

The most important of FENE potential is that it is an attractive potential and cannot be extended beyond  $r = R_0$ .

#### b) Force calculation

The force caused by FENE potential can be described by:

$$F_{FENE} = -\nabla V_{FENE}(r) = -\frac{kR_0^2}{R_0^2 - r^2} \cdot \vec{r} \quad (2.38)$$

#### 2.4.3 Lennard-Jones reduced units

According to the common practice of molecular dynamics simulations, all quantities will be presented in the reduced Lennard-Jones units, which is relative to the Lennard-Jones parameters (shown in Table 2.4.1).

**Table 2.1** Lennard-Jones reduced units.

Parameter	Reduced units	Relation to International System (IS)
Length	$r^*$	$r\sigma^{-1}$
Energy	$E^*$	$E\epsilon^{-1}$
Temperature	$T^*$	$k_B T\epsilon^{-1}$
Time	$t^*$	$t\sigma^{-1}\sqrt{\frac{\epsilon}{M}}$
Mass	$m^*$	$mM^{-1}$
Force	$F^*$	$F\sigma\epsilon^{-1}$
Pressure	$P^*$	$P\frac{\sigma^3}{\epsilon}$
Density	$\rho^*$	$N\sigma^3V^{-1}$

## 2.5 INTEGRATING THE EQUATIONS OF MOTION

Two popular integration methods for molecular dynamics calculations are used:

- Verlet algorithm
- Predictor-corrector algorithm

### 2.5.1 The Verlet algorithm

The Verlet algorithm is one of the most commonly used time integration algorithm in the molecular dynamics simulation [3, 12, and 23]. This algorithm is based simply on a truncated Taylor expansion of the particle coordinates:

$$r(t + \Delta t) = r(t) + v(t)\Delta t + \frac{1}{2}a(t)\Delta t^2 + \frac{\Delta t^3}{3!}\ddot{r} + \dots \quad (2.39)$$

Where  $\Delta t$  is the time step,

$a(t)$  is the instantaneous acceleration.

Then, integrate with Newton's law, that  $a(t)$  is just the force divided by the mass of the particle.

$$a(t) = -\frac{f(t)}{m} \quad (2.40)$$

Where  $f(t)$  is the instantaneous total force acting on the particle, and

$m$  is the mass of the particle.

### 2.5.2 The Euler scheme algorithm

This algorithm is not only one of the simplest, but also usually the best [3, 12, and 23].

It starts with a Taylor expansion of the coordinate of a particle, around time  $t$ :

$$r(t + \Delta t) = r(t) + v(t)\Delta t + \frac{f(t)}{2m}\Delta t^2 + \frac{\Delta t^3}{3!}\ddot{r} + O(\Delta t^4) \quad (2.41)$$

Similarly:

$$r(t - \Delta t) = r(t) - v(t)\Delta t + \frac{f(t)}{2m}\Delta t^2 - \frac{\Delta t^3}{3!}\ddot{r} + O(\Delta t^4) \quad (2.42)$$

Summing these two equations, then

$$r(t + \Delta t) + r(t - \Delta t) = 2r(t) + \frac{f(t)}{m}\Delta t^2 + O(\Delta t^4) \quad (2.43)$$

Or



$$r(t + \Delta t) \approx 2r(t) - r(t - \Delta t) + \frac{f(t)}{2m} \Delta t^2 \quad (2.44)$$

The velocity of the particle can also be obtained:

$$r(t + \Delta t) - r(t - \Delta t) = 2v(t)\Delta t + O(\Delta t^3) \quad (2.45)$$

Or

$$v(t) = \frac{r(t + \Delta t) - r(t - \Delta t)}{2\Delta t} + O(\Delta t^2) \quad (2.46)$$

This estimate of the new position and velocity contain an error which is of order  $\Delta t^4$  and  $\Delta t^2$ , respectively.

### 2.5.3 The leapfrog algorithm

The difference of this algorithm from the Verlet algorithm is evaluates the velocities at half-integer time steps and uses these velocities to compute the new positions [3, 24, 25]:

$$v\left(t + \frac{\Delta t}{2}\right) \equiv \frac{r(t + \Delta t) - r(t)}{\Delta t} \quad (2.47)$$

And

$$v\left(t - \frac{\Delta t}{2}\right) \equiv \frac{r(t) - r(t - \Delta t)}{\Delta t} \quad (2.48)$$

Therefore, the new positions base on the old positions and velocities can be obtained:

$$r(t + \Delta t) = r(t) + \Delta t \cdot v\left(t + \frac{\Delta t}{2}\right) \quad (2.49)$$

Integrate with the Verlet algorithm, we can have:

$$v\left(t + \frac{\Delta t}{2}\right) = v\left(t - \frac{\Delta t}{2}\right) + \Delta t \frac{f(t)}{m} \quad (2.50)$$

#### 2.5.4 Velocity-Verlet algorithm

This algorithm uses positions and velocities computed at equal times. In this algorithm, the new velocities can be computed only after the new positions are computed [3, 26].

Taylor expansion for the coordinates:

$$r(t + \Delta t) = r(t) + v(t)\Delta t + \frac{f(t)}{2m} \Delta t^2 \quad (2.51)$$

Then update the velocities:

$$v(t + \Delta t) = v(t) + \frac{a(t + \Delta t) + f(t)}{2m} \Delta t \quad (2.52)$$

For:

$$r(t + 2\Delta t) = r(t + \Delta t) + v(t + \Delta t)\Delta t + \frac{f(t + \Delta t)}{2m} \Delta t^2 \quad (2.53)$$

And equation 2.5.12 can be written as:

$$r(t) = r(t + \Delta t) - v(t)\Delta t - \frac{f(t)}{2m} \Delta t^2 \quad (2.54)$$

Then we can get:

$$r(t + 2\Delta t) + r(t) = 2r(t + \Delta t) + [v(t + \Delta t) - v(t)]\Delta t + \frac{f(t + \Delta t) - f(t)}{2m} \Delta t^2 \quad (2.55)$$

Integrate with equation 2.5.13, therefore:

$$r(t + 2\Delta t) + r(t) = 2r(t + \Delta t) + \frac{f(t + \Delta t)}{2m} \Delta t^2 \quad (2.56)$$

### 2.5.5 Beeman algorithm

Beeman's algorithm is a method for numerically integrating ordinary differential equations, generally position and velocity, which is closely related to verlet integration. It is generally more accurate in both position and velocity than most verlet schemes. It's most commonly seen in molecular dynamics simulations. This algorithm looks quite different from the Verlet algorithm [3].

$$r(t + \Delta t) = r(t) + v(t)\Delta t + \frac{4f(t) - f(t - \Delta t)}{6m} \Delta t^2 \quad (2.57)$$

And

$$v(t + \Delta t) = v(t) + \frac{2f(t + \Delta t) + 5f(t) - f(t - \Delta t)}{6m} \Delta t \quad (2.58)$$

It is easy to show that the positions of a particle satisfy the Verlet algorithm by using the above two equations. Moreover, the velocities are more accurate than in the original Verlet algorithm.

### 2.5.6 Predictor-corrector algorithm

Predictor-corrector algorithm is also one of the most commonly used methods and base on Taylor expansion to integrate the equations of motion [1, 4,5,11 and 27].

The basic idea of the predictor-corrector algorithm can be described by (shown in Figure 2.7):

- a) Find one point on the curve;
- b) Compute a tangent vector to the curve at that point;
- c) Step out a small amount along the tangent vector;
- d) Relocate the curve at a new point;
- e) Repeat step a) to step d) to the end.

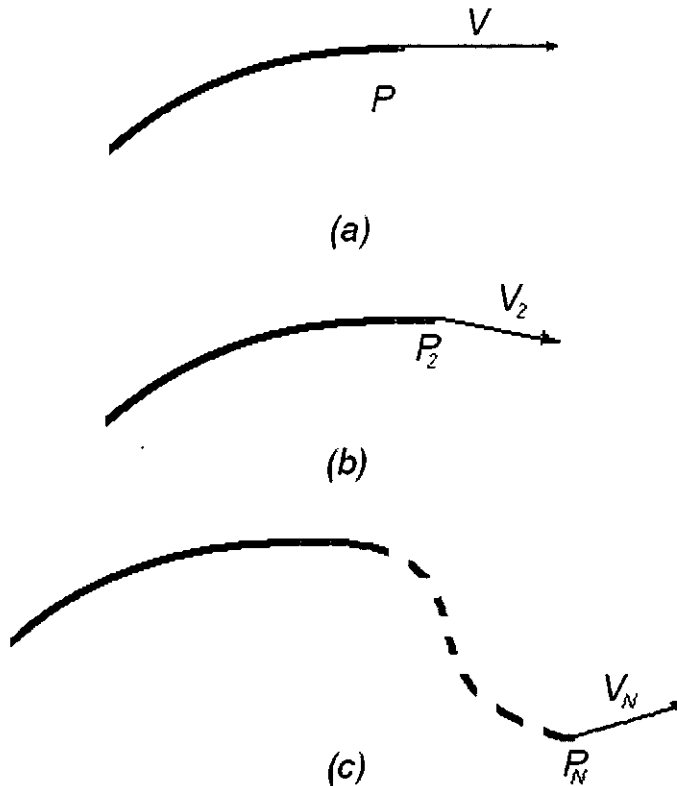


**Figure 2.7** the curve of how Predictor-corrector algorithm works.

Three major parts of predictor-corrector algorithm can be obtained:

- a) Predictor: The position  $r$ , velocity  $v$ , acceleration  $a$  and time derivative of the acceleration ( $\frac{\Delta t^3}{3!} \ddot{r}$  in equation 2.5.1) are all known at time  $t$ , one 'predicts' the same quantities at time  $t + \Delta t$  by using the Taylor expansion. Among these quantities are accelerations  $a$ .
- b) Force evaluation: The force is computed taking the gradient of the potential at the predicted positions. The resulting acceleration will be in general different from the 'predicted acceleration'. The difference between the two constitutes an 'error signal'.
- c) Corrector: This error signal is used to 'correct' positions and their derivatives. All the corrections are proportional to the error signal, the coefficient of proportionality being a 'magic number' determined to maximize the stability of the algorithm.

### 2.5.7 Periodic boundary condition

Molecular dynamics simulations usually focus on the macroscopic behaviour of the materials. However, due to the capacity limitation of computers, it is every difficult to simulate the particles more than 10 million at one time. These numbers of particles are still far below from the real size of systems, which result an issue at the system boundaries.

The states of particles near the boundaries are different from those of particles more fully surrounded by other particles, because the particles surrounded by boundaries have deficient bonds. Moreover, the particles' motion during the simulation course,

velocities to all particles must match the desired temperature by using the equation 2.7.

### 2.6.2 Equilibration

The equilibrium in the molecular dynamics simulation always means the thermodynamic equilibrium. Every time, the change of any parameter of the system will results the non-equilibrium of the system for a while. And then a new equilibrium will be reached. Therefore, the system moves from one equilibrium state to another. It may the temperature system, density, pressure of system or any other parameters which can affect the system.

Usually, the system should be measured in the equilibrium state. A physical quantity  $A$  generally approaches its equilibrium value exponentially with time:

$$A(t) = A_0 + C \exp\left(-\frac{t}{\tau}\right) \quad (2.59)$$

Where  $A(t)$  is a physical quantities averaged over a short time, and

$\tau$  is the relaxation time.

## 2.7 APPLICATIONS

Given the modelling capability of MD and the variety of techniques that have emerged, it can be used to solve many kinds of problems. Certain applications can be eliminated owing to the classical nature of MD. There are also hardware imposed limitations on the amount of computation that can be performed over a given period of time – be it an hour or a month – thus restricting the number of molecules of a given complexity that can be handled, as well as storage limitations having similar consequences (to some extent, the passage of time helps alleviate hardware

restrictions).

The phenomena that can be explored must occur on length and time scales that are encompassed by the computation. Some classes of phenomena may require repeated runs based on different sets of initial conditions to sample adequately the kinds of behaviour that can develop, adding to the computational demands. Small system size enhances the fluctuations and sets a limit on the measurement accuracy; finite-size effects – even the shape of the simulation region – can also influence certain results. Rare events present additional problems of observation and measurement.

Liquids represent the state of matter most frequently studied by MD methods. This is due to historical reasons, since both solids and gases have well-developed theoretical foundations, but there is no general theory of liquids. For solids, theory begins by assuming that the atomic constituents undergo small oscillations about fixed lattice positions; for gases, independent atoms are assumed and interactions are introduced as weak perturbations. In the case of liquids, however, the interactions are as important as in the solid state, but there is no underlying ordered structure to begin with.

The following list includes a somewhat random and far from complete assortment of ways in which MD simulation is used:

- Fundamental studies: equilibration, tests of molecular chaos, kinetic theory, diffusion, transport properties, size dependence, tests of models and potential functions. Such as, J. M. Haile has used the molecular dynamic simulation to study the Lennard-Jones fluid for obtaining results in the isoenthalpic–isobaric ensemble [29].
- Phase transitions: first- and second-order, phase coexistence, order parameters, critical phenomena. Such as Y. Abe, K. Tashiro used molecular dynamics

simulation to perform the ferroelectric phase transition of vinylidene fluoride-trifluoroethylene copolymers. And found that the transition behaviour was governed by the balance among the torsional potential energy barrier of the skeletal chains, the intermolecular van der Waals interaction, and the Coulombic interaction between the atomic charges. Additionally, the introduction of head-to-head and tail-to-tail abnormal linkages into the molecular chains expanded the cell volume and lowered the phase-transition temperature [30].

- **Complex fluids:** structure and dynamics of glasses, molecular liquids, pure water and aqueous, liquid crystals, ionic liquids, fluid interfaces, films and monolayer. Such as, V. Symeonidis, G. Em Karniadakis, B. Caswell used Dissipative particle dynamics (DPD) method simulate efficiently complex liquids and dense suspensions using only a few thousands of virtual particles and at speed-up factors of more than one hundred thousands compared to molecular dynamics [31].
- **Polymer:** chains, rings and branched molecules, equilibrium conformation, relaxation and transport processes. Such as, D. Brandell, A. Liivat, A. Aabloo and J. O. Thomas have studied short-chain poly(ethylene oxide) system by molecular dynamics simulation in order to probe the effect of chain length on the structure and properties of ionically conducting polymer electrolytes [40].
- **Solids:** defect formation and migration, fracture, grain boundaries, structural transformations, radiation damage, elastic and plastic mechanical properties, friction, shock waves, molecular crystals, epitaxial growth.
- **Biomolecules:** structure and dynamics of problems, protein folding, micelles, membranes, docking of molecules.



- Fluid dynamics: laminar flow, boundary layers, rheology of non-Newtonian fluids, unstable flow.

Molecular dynamics simulation has also been applied in nanoscience, especially in nanocomposites, such as mechanical behaviour [32], magnetic properties [33], binding energy [34, 35], etc.. Molecular dynamics simulation has also been used to study polymer clay nanocomposites, such as, failure mechanism [36, 37], dynamics fracture [31], and used to understanding fracture [39].

## REFERENCE

1. J. M. Haile, *Molecular dynamics simulation*, **Wiley**, (1992).
2. Frenkel, D. and B. Smit, *Understanding Molecular Simulation.*, **Academic Press**, San Diego, (1996).
3. Michael P. Allen, *Computational. Soft. Matter.*, **NIC. 23**: 1, (2004).
4. M. P. Allen and D. J. Tildesley, *Computer simulation of liquids*, Oxford, (1987).
5. G. Ciccotti and W. G. Hoover, Eds., *Molecular dynamics simulation of statistical-mechanical systems*, North-Holland, (1986).
6. G. C. Maitland, M. Rigby, E. B. Smith, and W. A. Wakeham, *Intermolecular forces: their origin and determination*, **Clarendon Press**, Oxford, (1981)
7. C. G. Gray, and K. E. Gubbins, *Theory of molecular fluids. 1. Fundamentals*, **Clarendon Press**, Oxford, (1984).
8. M. Sprik, Michael P. Allen, and Dominic. J. Tildesley, *Computer Simulation in Chemical Physics*, **397 NATOASI (C)**: 211, (1993).
9. A. J. Stone, *The Theory of Intermolecular Forces*, **Clarendon Press**, Oxford, (1996).
10. Michael P. Allen, Glenn T. Evans, Daan Frenkel, and Bela Mulder, *Adv. Chem. Phys.*, **86**, 1, (1993).

11. A. Rahman, *Phys. Rev. A*, **136**, 405, (1964).
12. L. Verlet, *Phys. Rev.*, **159**, 98, (1967).
13. J. Weeks, D. Chandler, and H. C. Andersen, *J. Chem. Phys.*, **54**, 5237, (1971).
14. K. Kremer, and G. S. Grest, *J. Chem. Phys.*, **92**, 5057, (1990).
15. B. Chen, M. G. Martin, and J. I. Siepmann, *J. Phys. Chem. B*, **102**, 2578, (1998).
16. S. K. Nath, F. A. Escobedo, and J. J. de Pablo, *J. Chem. Phys.*, **108**, 9905, (1998).
17. M. G. Martin and J. I. Siepmann, *J. Phys. Chem. B*, **102**, 2569, (1998).
18. J. R. Errington and A. Z. Panagiotopoulos, *J. Phys. Chem. B*, **103**, 6314, (1999).
19. M. Tsige, J. G. Curro, G. S. Grest, and J. D. McCoy, *Macromolecules*, **36**, 2158, (2003).
20. E. Garcia, M. A. Glaser, N. A. Clark, and D. M. Walba, *J. Molec. Struct. - THEOCHEM*, **464**, 39, (1999).
21. D. Reith, H. Meyer, and F. Muller-Plathe, *Comput. Phys. Commun.*, **148**, 299, (2002).
22. D. Reith, M. Putz, and F. Muller-Plathe, *J. Comput. Chem.*, **24**, 1624, (2003).
23. L. Verlet, *Phys. Rev.*, **165**, 201, (1968).
24. R. W. Hockney and J. W. Eastwood. *Computer simulations using particles*. Adam Hilger, Bristol, (1988).
25. R. P. Feynman, R. B. Leighton and M. Sands, *The Feynman Lectures on Physics, Vol. I*, Addison-Wesley, (1963).
26. W. C. Swope, H. C. Andersen, P. H. Berens, and K. R. Wilson. *J. Chem. Phys.*, **76**, 637, (1982).
27. C. W. Gear. *Numerical initial value problems in ordinary differential equations*. Prentice-Hall, Englewood Cliffs, NJ, (1971).
28. D. C. Rapaport. *The art of molecular dynamics simulation*. Cambridge

University Press, (1995).

29. J. M. Haile, *J. Chem. Phys.*, **73**, 2412, (1980).
30. Y. Abe, K. Tashiro, *J. Polym. Sci. B: Polym. Phys.*, **39**, 689, (2001).
31. V. Symeonidis, G. Em Karniadakis, B. Caswell, *Computing in Science and Engineering*, **7**, 39, (2005).
32. E. Chabert, C. Gauthier, R. Dendievel, L. Chazeau, and J.-Y. Cavaillé, GROUPE D'ETUDES DE METALLURGIE PHYSIQUE ET DE PHYSIQUE DES MATERIAUX VILLEURBANNE (FRANCE), Conference proceedings (2003).
33. H. Fukunga, N. Kitajiman, Y. Kanai; *Mater. trans. – JIM*, **37**, 641 (1996).
34. R. Toth, c, A. Coslanicha, M. Ferronea, M. Fermegliaa, S. Pricla, S. Miertusb and E. Chiellinic, **45**, 8075 (2004).
35. M. Fermeglia, M. Ferrone, S. Pricl; *Fluid Phase Equilibria*, **212**, 315 (2003).
36. Kelly L. Anderson, E. Manias, R.A. Vaia1, and B.L. Farmer; *Polymeric Materials: Science and Engineering*, **92**, 207 (2005).
37. Martin N. Bureau, Minh-Tan Ton-That, Florence Perrin-Sarazin; *Engineering Fracture Mechanics*, **73**, 2360 (2006).
38. P. Vashishta, Rajiv K. Kalia and A. Nakano; *Computer In Science & Engineering*, **5**, 56 (1999).
39. P. Vashishta, Rajiv K. Kalia and A. Nakano; *Computer In Science & Engineering*, **1**, 39 (1999).
40. D. Brandell, A. Liivat, A. Aabloo and J. O. Thomas, *J. Mater. Chem.*, **15**, 4338, (2005).

## CHAPTER 3

### PROGRAMME FOR MOLECULAR DYNAMICS SIMULATION OF FRACTURE AND ENERGY DISSIPATION

#### 3.1 INTRODUCTION

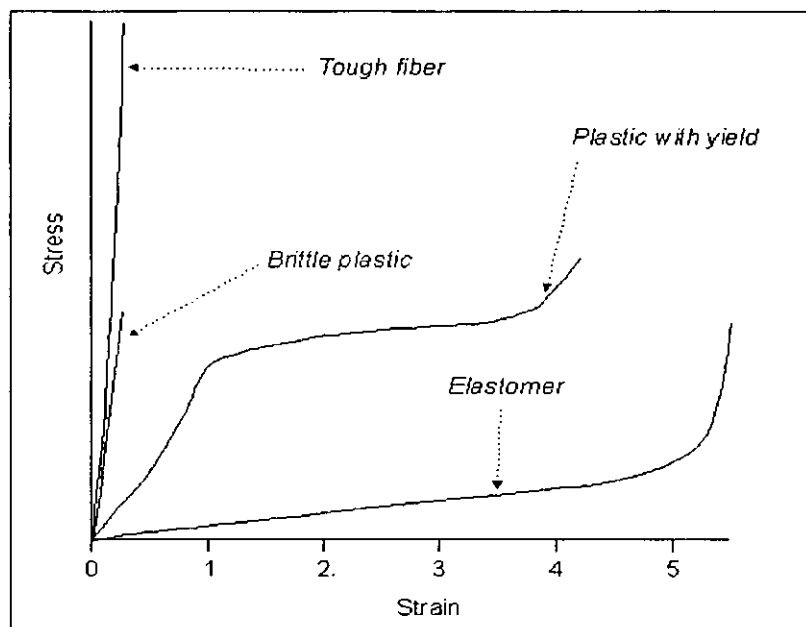


**Figure 3.1** Stress- strain curve of polymers.

A tensile test, also known as tension test, is probably the most fundamental type of mechanical test you can perform on material. Tensile tests are simple, relatively inexpensive, and fully standardized.

Tensile testing can be carried out to see how the material will react to forces being applied in tension by pulling on the specimen. As the material is being pulled, you will find its strength along with how much it will elongate.

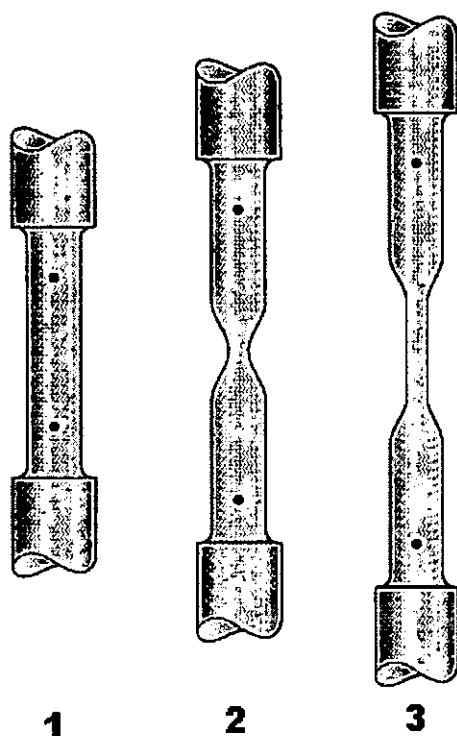


**Figure 3.2** deformation of specimen during the test.

As the loading increase, the specimen cross-sectional area decreases, becoming thinner, and increases in length before it fails completely. In this process, the volume of the specimen is kept constant.

Compressed (theoretical) elastic spring will return 100 percent of the potential energy as work when it is released. This theoretical energy is called the elastic potential energy of the spring. In reality, no spring is 100 percent efficient. Rather than return to its original state via the same path on the force-deformation curve as when it was compressed, a real spring will return via a different path because of friction in the spring and energy lost as heat and/or sound. This behaviour, called viscoelasticity, is identified by hysteresis, the difference between the loading and unloading portions of the load-deformation curve.

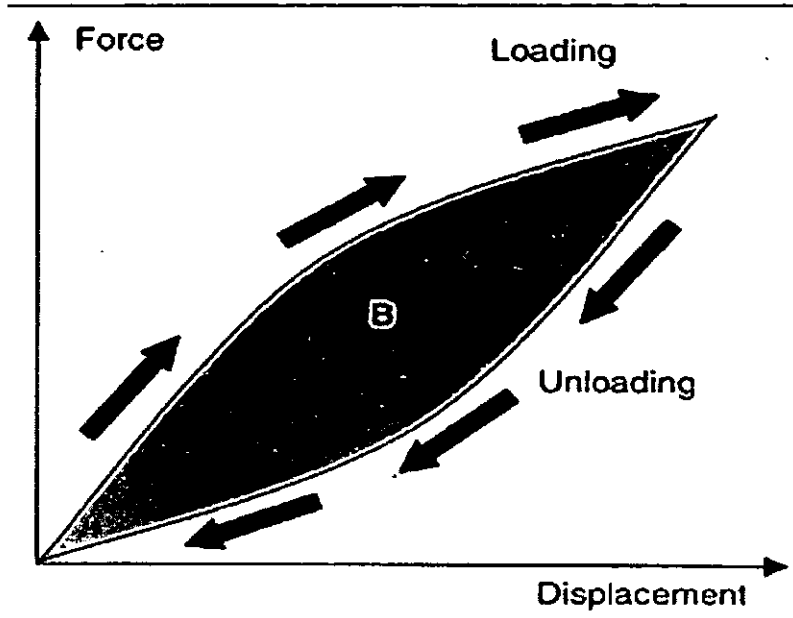


**Figure 3.3** Load- deformation curve of a viscoelastic material. B= dissipated energy.

Biaxial tests are usually used to investigate the response of these materials to cyclic loading. A particularly interesting question is whether a limit load exists, below which the excitations shake down, in the sense that the material does not accumulate further deformations. The role of the dissipated energy through out the experiment is the key for the characterization of the different regimes of responses (shown in Figure 3.3.).

The simulation includes 3 main parts shown in Figure 3.4, i.e., configuration part, simulation part and data output part.

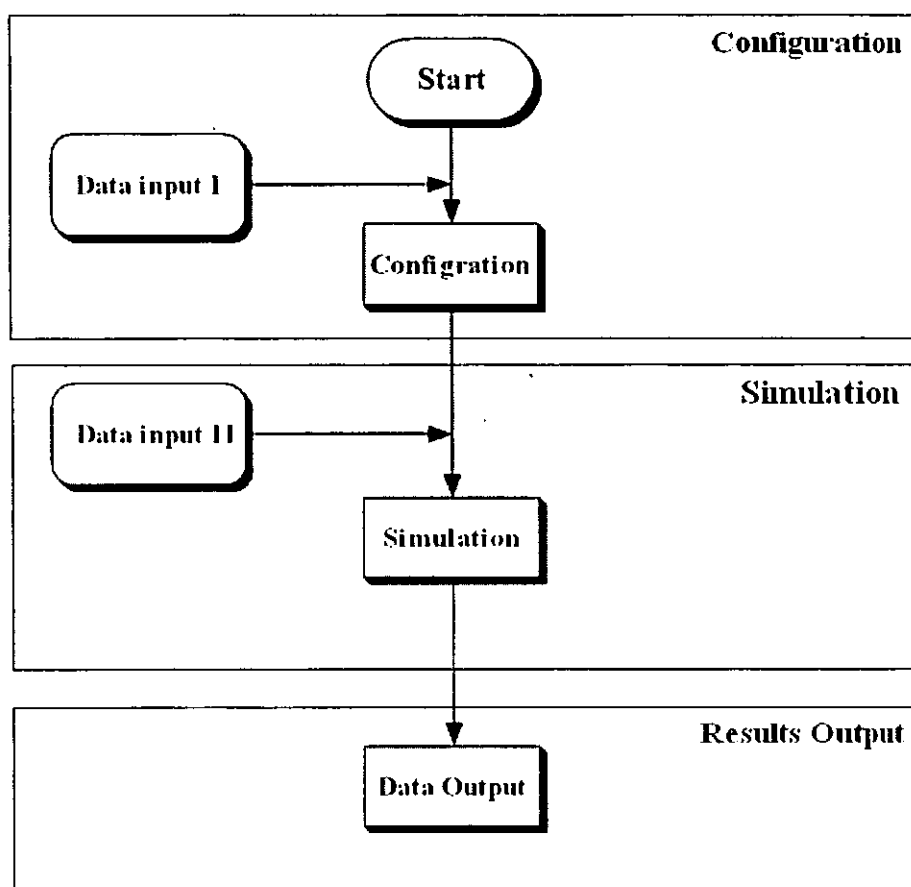


**Figure 3.4** Main flow chart of the simulation.

In the simulation, it is impossible to exhibit the shakage of the material directly. Then the vacancy introduced method will be used in the simulation. In this method, the top wall of simulation area move up and down in order to introduce the vacancy into system. Due to the periodic boundary condition, therefore, the actual volume of materials are not changed. (see Figure 3.5)

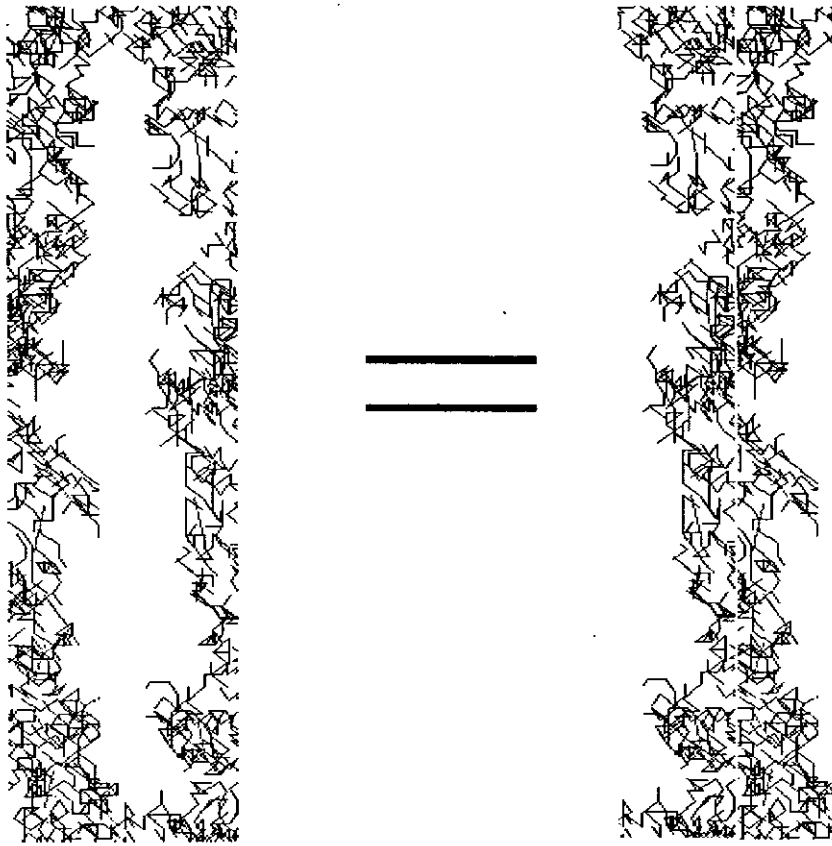


*Figure 3.5* Necking perform once in the simulation.

## **3.2 PROGRAMS FOR MOLECULAR DYNAMICS SIMULATION OF FRACTURE IN POLYMER COMPOSITES**

### **3.2.1 Configuration**

This is used to get the initial conditions of the material suppose, such as the numbers of polymer chains, the numbers of monomers in each polymer chain, the numbers of nanofillers, the dimensional condition setting of the nanofillers, temperature, pressure, etc.

#### **Initial state**



We assume that the simulation starts from an equilibrium state, and the nature of the initial configuration should have no influence whatever on the outcome of the simulation. The method in choosing the initial coordinates is to position the simulation units (molecular segments and nanoplatelets) at the sites of a lattice whose unit cell size is chosen to ensure uniform coverage of the simulation region. The lattices used in the simulation are the three dimensions face centered cubic (FCC) and simple cubic. A Monte Carlo procedure was used to avoid overlap, since the dynamics will produce the necessary randomization very quickly.

The function that generates an FCC arrangement follows:

---

```
void InitCoords ()
{
    VecR c, gap;
    Int j, n, nx, ny, nz;

    VDiv (gap, region, initUcell);

    n=0;
    for (nz=0; nz<initUcell.z; nz++) {
        for (ny=0; ny<initUcell.y; ny++) {
            for (nx=0; nx<initUcell.x; nx++) {
                VSet (c, nx+0.25, ny+0.25, nz+0.25);
                VMul (c, c, gap);
                VVSAdd (c, -0.5, region);
                for (j=0; j<4; j++) {
                    mol[n].r=c;
                    if (j !=3) {
```

---

```
        if (j != 0) mol [n].r.x += 0.5*gap.x;
        if (j != 0) mol [n].r.y += 0.5*gap.y;
        if (j != 0) mol [n].r.z += 0.5*gap.z;
    }
    ++n;
}
}
}
}
```

---

### **Initial velocities**

Similar considerations apply to the initial velocities, namely, that rapid equilibration renders that careful fabrication of a Maxwell distribution unnecessary. The function *VRand* used to producing a random unit vector in three dimensions. The following functions are used:

---

```
#define VScale (v, s)
    (v).x*=s,
    (v).y*=s

#define VVAdd(v1, v2)  VAdd (v1, v1, v2)

void InitVels ()
{
    int n;

    VZero (vSum);
```

---

```
DO_MOL {  
    VRand (&mol [n].rv);  
    VScale (mol [n].rv, velMag);  
    VVAdd (vSum, mol [n].rv);  
}  
DO_MOL VVSAdd (mol [n].rv, -1./nMol, vSum);  
}
```

```
void InitAccels ()
```

```
{  
    int n;
```

```
    DO_MOL VZero (mol [n],ra);
```

```
void VRand (VecR *p)
```

```
{  
    real s;  
  
    s=2.*M_PI*RandR ();  
    p->x=cos (s);  
    P->y=sin (s);  
}
```

---

### **Temperature adjustment**

Bringing the system to the required average temperature calls for velocity rescaling. If there is a gradual energy drift due to numerical integration error, further velocity adjustments will be required over the course of the run. The drift rate depends on a number of factors- the integration method, potential function, the value of  $\Delta t$  and the

ambient temperature.

Since  $T$  fluctuates there is no point in making adjustments based on instantaneous estimates. Instead, we can make use of the average  $\langle T \rangle$  values that are already available. The temperature adjustment (or velocity rescaling) function below would therefore be called from *SingleStep* immediately following the call *AccumProps* (2) used for summarizing the results. The functions are shown below:

---

```
void AdjustTemp ()
{
    real vFac;
    int n;
    vvSum=0
    DO_MOL vvSum +=VLenSq (mol[n].rv);
    vFac=velMag/sqrt (vvSum/ nMol);
    DO_MOL VScale (mol[n].rv, vFac);
}
```

```
void SingleStep ()
{
    ++ stepCount;
    timeNow= stepCount * deltaT;
    LeapfrogStep (1);
    ApplyBoundaryCond ();
    ComputeForces ();
    LeapfrogStep (2);
    EvalProps ();
    AccumProps (1);
}
```

---

```
if (stepCount % stepAvg ==0) {
    AccumProps (2);
    PrintSummary (stdout);
    AccumProps (0);
}
}

#define PropZero (v)
    v.sum =0.,
    v.sum2 =0.

#define PropAccum (v)
    v.sum +=v.val,
    v.sum2 +=Sqr (v.val)

#define PropAvg (v, n)
    v.sum /=n,
    v.sum2 =sqrt (Max (v.sum2/ n - Sqr (v.sum), 0.))

#define PropEst (v)
    v.sum,
    v.sum2

void AccumProps (int icode)
{
    if (icode ==0) {
        PropZero (totEnergy);
        PropZero (kinEnergy);
        PropZero (pressure);
```

---

```
} else if (icode ==1) {  
    PropAccum (totEnergy)  
    PropAccum (kinEnergy);  
    PropAccum (pressure);  
} else if (icode ==2) {  
    PropAvg (totEnergy)  
    PropAvg (kinEnergy);  
    PropAvg (pressure);  
}  
}
```

---

How frequently this adjustment is required, if at all, must be determined empirically; initially it should be omitted since it may interfere with energy conservation. If needed, the interval between adjustments would be specified by the variable

---

```
int stepAdjustTemp;
```

---

The value included in the input data

---

```
Name1 (stepAdjustTemp),
```

---

And the adjustment made by a call from *SingleStep*

---

---

---

```
if (stepCount % stepAdjustTemp == 0 ) AdjustTemp ();
```

---

A possible alternative would be to automate the scheme, applying the adjustment whenever the drift exceeds a given threshold.

Forcing the system to have the correct  $\langle T \rangle$  during the equilibration phase of the simulation uses separate estimates of  $\langle E_k \rangle$ . In SingleStep add (after the call to EvalProps)

---

```
if (stepCount < stepEquil ) AdjustTemp ();
```

---

### 3.2.2 Simulation

This part is the main part of the simulation, which included the equilibration of the system, potential and force calculate, etc..

#### Equilibration

Characterizing equilibrium is by no means an easy task. Averaging over a series of time steps will reduce the fluctuations, but different quantities relax to their equilibrium averages at different rates, and this must also be taken into account when trying to establish when the time is ripe to begin making measurements. Unfortunately, relaxation is generally quite rapid for nanofillers, but thousands times longer for polymers. Therefore, multi-time scale will be used in this simulation. Equilibration can be accelerated by starting the simulation at a higher temperature and later cooling by rescaling the velocities (this is similar, but not identical, to using a larger time step initially); too high a temperature will, however, lead to numerical instability.

One simple measure of equilibration is the rate at which the velocity distribution converges to its expected final form.

The Maxwell distribution:

$$f(v) = \frac{\rho}{(2\pi T)^{d/2}} e^{-v^2/2T} \quad (3.1)$$

In MD units which, after angular integration, becomes

$$f(v) \propto v^{d-1} e^{-v^2/2T} \quad (3.2)$$

The distribution can be measured by constructing a histogram of the velocity values  $\{h_n | n = 1, \dots, N_b\}$ , where  $h_n$  is the number of atoms with velocity magnitude between  $(n-1) \Delta v$  and  $n \Delta v$ ,  $\Delta v = v_m / N_b$ , and  $v_m$  is a suitable upper limit to  $v$ . The normalized histogram represents a discrete approximation to  $f(v)$ .

The function that carries out this computation is

---

```
#define VLen (v) sqrt (VDot (v, v))
#define Min (x1, x2)
  (((x1) < (x2)) ? (x1) : (x2))

void EvalVelDist ()
{
  Real deltaV, histSum;
  int j, n;
```

---



```
if (countVel == 0) {  
    for (j = 0; j < sizeHistVel; j++) histVel [j] = 0.;  
}  
deltaV=rangeVel / sizeHistVel;  
DO_MOL {  
    j = VLen (mol[n].rv) / deltaV;  
    ++ histVel [Min (j, sizeHistVel -1)];  
}  
++ countVel;  
if (countVel == limitVel) {  
    histSum = 0.;  
    for (j=0; j < sizeHistVel; j++) histSum += histVel [j];  
    for (j=0; j < sizeHistVel; j++) histVel [j] /= histSum;  
    PrintVelDist (stdout);  
    countVel = 0  
}  
}
```

---

Depending on the value of *countVel*, the function will, in addition to adding the latest results to the accumulated total, either initialize the histogram counts, or carry out the final normalization. Other kinds of analysis in subsequent case studies will involve functions that operate in a similar manner.

In order to use this function storage for the histogram array must be allocated, and a number of additional variables declared and assigned values. Variables are

---

```
real *histVel, rangeVel;  
int countVel, limitVel, sizeHistVel, stepVel;
```

---

And those included in the input data must be added to the array *namelist*,

---

```
NameI (limitVel),  
NameR(rangeVel),  
NameI (sizeHistVel),  
NameI (stepVel),
```

---

Allocation of the histogram array is included in *AllocArrays*,

---

```
AllocMem (histVel, sizeHistVel, real);
```

---

Initialization, in *SetupJob*, requires the additional statement

---

```
void SetupJob ()  
{  
    AllocArrays ();  
    stepCount = 0;  
    InitCoords ();  
    InitVels ();  
    InitAccels ();
```

---

```
AccumProps (0);  
countVel = 0;  
}
```

---

And the histogram function is called from *SingleStep* by:

---

```
if (stepCount >= stepEquil &&  
    (stepCount - stepEquil) % stepVel == 0) EvalVelDist ();
```

---

Histogram output is provided by the function

---

```
void PrintVelDist (FILE*fp)  
{  
    real vBin;  
    int n;  
  
    printf ("vdist (%.3f)\n", timeNow);  
    for (n = 0; n < sizeHistVel; n++) {  
        vBin = (n + 0.5) * rangeVel / sizeHistVel;  
        fprintf (fp, "%8.3f  %8.3f\n", vBin, histVel [n]);  
    }  
}
```

---

### **Motion in a force field**

The collision prediction process is not affected at all because the same uniform

acceleration is experienced by all nanofillers and monomers, so that the computation for determining the existence of a collision and when it occurs is independent of the field. Between collisions nanofillers and monomers follow parabolic rather than linear trajectories.

It is only the prediction of cell crossings that calls for special attention, because parabolic motion means that it is possible for an nanofiller or monomer to leave a cell through the face (or edge) of entry. The resulting changes to *PredictEvent* follow, where the force field *forceField* is assumed to act in the negative y direction; the algebraic problem solved here is locating the intersection of a parabola with a straight line.

---

```
Vec1 signDir
real h, h1, h2;

VCopy (w, mol[na]. inCell);
if (mol[na].rv.x >0.) ++ w.x;
signDir.x = (mol[na].rv.x <0);
If (forceField.y == 0. && mol[na].rv.y>0 ++w.y;
VMul (w, w, region);
VDiv (w, w, cells);
VSAdd (rs, mol[na].r, 0.5, region);
VVSub (w, rs);
WhenCross (x);
if (forceField.y !=0.) {
    h1 = Sqr (mol[na].rv.y) +2.*forceField.y * w.y;
    if (mol[na].rv.y >0.) {
        h2 = h1 + 2. * forceField.y * region.y/cells.y;
```

---

```
if (h2 > 0.) {  
    h= -sqrt (h2);  
    signDir.y =1;  
} else {  
    h= sqrt (h1);  
    signDir.y=1;  
}  
tm.y=-(mol[na].rv.y+h)/forceField.y;  
} else {  
    WhenCross (y);  
    signDir.y = (mol[na].rv.y < 0.);  
}
```

---

The role of *signDir* will become clear shortly when we continue with the discussion of changes to *PredictEvent*.

The function *UpdateMol* for updating positions must be modified to allow for parabolic trajectories, with the velocity also being updated.

---

```
void UpdateMol (int id)  
{  
    real tInt;  
  
    tInt = timeNow - mol[id].time;  
    VVSAdd (mol[id].r, tInt, mol[id].rv);  
    VVSAdd (mol[id].r, 0.5 * Sqr (tInt), forceField);
```

---

```
VVSAdd (mol[id].r, tInt, forceField);  
Mol[id].time = timeNow;  
}
```

---

Because local time variables are associated with each nanofiller or monomer, a similar modification is required in *PredictEvent* for the collision prediction.

---

```
VVSAdd (dr, -0.5 * Sqr (tInt), forceField);  
VVSAdd (dv, -tInt, forceField);
```

---

When checking for energy conservation, allowance should be made for the gravitational potential energy contribution.

### **Hard- wall boundaries**

The boundaries used in this study are all rigid, although the side walls could be replaced by periodic boundaries. These hard walls can be smooth, in which case collisions with the walls are energy-conserving, specular collisions, but in most situations the walls will be rough, so that after undergoing a collisions an nanofiller or monomer loses all memory of its prior velocity. Simply randomizing the velocity direction (and possibly magnitude) will achieve this effect.

Each wall is divided into a series of narrow strips with width typically equal to the monomer diameter; when an nanofiller or monomer collides with the wall the outcome alternates between specular collisions and velocity reversals, depending on

the trip involved- a kind of corrugation effect. If the wall is also attached to a thermal reservoir held at constant temperature, as is the case for the top and bottom walls, the velocity magnitude can be changed to the required value.

Collisions with the hard walls require a new form of processing, so an additional class of cell boundary event is introduced; in *SingleEvent*, all cell events are now identified by the modified test.

---

```
if (evldb < MOL_LIMIT + NDIM *2// evldb >= MOL_LIMIT +100)
```

---

The usual cell events are covered by the latter part of the test, while the former, together with `evldb >= MOL_LIMIT`, accounts for the wall collisions.

The function *ProcessCellCrossing* is modified to handle wall collisions as well as regular cell crossings.

---

```
VecR rs;  
VecI irs;  
real vFac, vv;  
int j, jj;  
  
j= evldb- MOL_LIMIT;  
if (j>=100) {  
    jj=j-100;  
} else {  
    jj=j/2;
```

---

```
VComp (cellRange [j %2], jj)=0;
VComp (mol[evldA].r, 0.5, region);
VDiv (rs, rs, roughWid);
VCopy (irs, rs)
if (jj !=0 && irs.x %2 ==0) mol[evldA].rv.x *=-1.;
if (jj !=1 && irs.x %2 ==0) mol[evldA].rv.x *=-1.;
if (thermalWall[jj]) {
    vv = VLenSq (mol[ecldA].rv);
    vFac = sqrt (NDIM * wallTemp[j % 2]/vv);
    VScale (mol[evldA].rv, vFac);
}
}
```

---

In *PredictEvent*, changes are required in determining the identity of the cell event about to be scheduled and the range of cells that must be examined.

---

```
#define LimitCells (t)
    if (mol[na].inCell.t +cellRangeT[0].t== -1
        cellRangeT[0].t=0;
    if (mol[na].inCell.t +cellRangeT[0].t==cells.t
        cellRangeT[0].t=0;

    VecI cellRangeT [2];

    dir= (tm.x <tm.y) ?0:1;
    evCode =100+dir;
```

---



```
if (VComp (mol[na].inCell, dir)==0 &&
    VComp (signDir, dir)==1) evCode = 2*dir;
else if (VComp (mol[na].inCell, dir)==Vcomp (cells, dir)-1 &&
    VComp (signDir)==0) evCode=2*dir +1;
ScheduleEvent (na, MOL_LIMIT +evCode, timeNow + VComp (tm, dir));
cellRangeT[0]= cellRange [0];
cellRangeT[1]= cellRange [1];
LimitCells (x);
LimitCells (y);
for (m1y = cellRangeT [0].y; m1y<= cellTangeT[1].y; m1y ++) {
}
```

---

Here, *cellRangeT* replaces *cellRange* for the limits of the nested x and y cell loops.

As formulated above, a nanofiller or monomer is deemed to collide with the wall when its centre reaches the wall position. While not affecting the results here, it is more sensible (and necessary if nanofillers of monomers of mixed sizes are involved) if the collision occurs when the wall-atom distance equals the atom radius. In the present case the only changes needed are to enlarge the region slightly and shift the initial coordinates.

### **Boundaries and driving force**

There are two kinds of boundary that must be considered in this problem- the region boundaries and the obstacle perimeter. Region boundaries can be made periodic so that the system recirculates, provided that any memory of nonuniform system is erased by, for example, periodically randomizing the velocities of all nanofillers and segments located very close to either end of the system. The obstacle boundary should be tough to ensure that the adjacent fluid layer is at rest, corresponding to the nanslip

boundary that occurs experimentally. There are various ways of accomplishing this; a particularly simple approach for two-dimensional system around a circular obstacle is to represent the obstacle as a ring of fixed atoms identical to those in the system.

The system is driven by superimposing a velocity bias in the motion direction when carrying out the velocity randomization; a constant external field could have been used instead.

### **3.2.3 Data output and graphing**

The major task of this part is output the data of result and draw the force/area vs distance curve and snapshot, etc..

#### **Snapshot**

Snapshot of the system configuration are stored on disk by the following function:

---

```
#define SCALE_FAC 32767.

void PutConfig ()
{
    VecR w;
    int blockSize, f0k, n;
    short *rl;
    FILE *fp;

    F0k=1;
    blockSize = (NDIM+1)*sizeof (real)+3*sizeof (int)+nMol*NDIM*sizeof (short);
    if ((fp=fopen (filename[FL_SNAP], "a"))!=0) {
        WriteF (blockSize);
```

---

```
WriteF (nMol);
WriteF (region) ;
WriteF (StepCount);
WriteF (timeNow);
AllocMem (rl,NDIM*nMol, short);
DO_MOL {
    VDiv (w, mol[n].r, region);
    VAddCon (w, w, 0.5);
    VScale (w, SCALE_FAC);
    VToLin (rl, NDIM *n, w);
}
WriteFN (rl, NDIM*nMol);
free (rl);
if (ferror (fp)) f0k=0;
fclose (fp);
} else f0k=0;
if (! F0k) ErrExit (ERR_SNAP_WRITE);
}
```

---

### 3.3 PROGRAMS FOR MOLECULAR DYNAMICS SIMULATION OF ENERGY DISSIPATION IN POLYMER NANOCOMPOSITES

#### 3.3.1 Configuration

This is used to get the initial conditions of the material suppose, such as the numbers of polymer chains, the numbers of monomers in each polymer chain, the numbers of nanofillers, the dimensional condition setting of the nanofillers, temperature, pressure, etc.

#### Initial state

We assume that the simulation start from an equilibrium state, and the nature of the initial configuration should have no influence whatever on the outcome of the simulation. The method in choosing the initial coordinates is to position the simulation units (molecular segments and nanoplatelets) at the sites of a lattice whose unit cell size is chosen to ensure uniform coverage of the simulation region. The lattices used in the simulation are the three dimensions face centred cubic (FCC) and simple cubic. A Monte Carlo procedure was used to avoid overlap, since the dynamics will produce the necessary randomization very quickly.

The function that generates an FCC arrangement follows:

---

```
void InitCoords ()
{
    VecR c, gap;
    Int j, n, nx, ny, nz;

    VDiv (gap, region, initUcell);

    n=0;
    for (nz=0; nz<initUcell.z; nz++) {
        for (ny=0; ny<initUcell.y; ny++) {
            for (nx=0; nx<initUcell.x; nx++) {
                VSet (c, nx+0.25, ny+0.25, nz+0.25);
                VMul (c, c, gap);
                VVSAdd (c, -0.5, region);
                for (j=0; j<4; j++) {
                    mol[n].r=c;
                    if (j !=3) {
```

---

```
        if (j !=0) mol [n].r.x+=0.5*gap.x;
        if (j !=0) mol [n].r.y+=0.5*gap.y;
        if (j !=0) mol [n].r.z+=0.5*gap.z;
    }
    ++n;
}
}
}
}
```

---

### **Initial velocities**

Similar considerations apply to the initial velocities, namely, that rapid equilibration renders that careful fabrication of a Maxwell distribution unnecessary. The function *VRand* used to producing a random unit vector in three dimensions. The following functions are used:

---

```
#define VScale (v, s)
    (v).x*=s,
    (v).y*=s

#define VVAdd(v1, v2)  VAdd (v1, v1, v2)

void InitVels ()
{
    int n;
```

---

```
VZero (vSum);  
DO_MOL {  
    VRand (&mol [n].rv);  
    VScale (mol [n].rv, velMag);  
    VVAdd (vSum, mol [n].rv);  
}  
DO_MOL VVSAdd (mol [n].rv, -1./nMol, vSum);  
}
```

```
void InitAccels ()
```

```
{  
    int n;
```

```
    DO_MOL VZero (mol [n],ra);
```

```
void VRand (VecR *p)
```

```
{  
    real s;
```

```
    s=2.*M_PI*RandR ();
```

```
    p->x=cos (s);
```

```
    P->y=sin (s);
```

```
}
```

---

### Temperature adjustment

Bringing the system to the required average temperature calls for velocity rescaling. If there is a gradual energy drift due to numerical integration error, further velocity adjustments will be required over the course of the run. The drift rate depends on a

number of factors- the integration method, potential function, the value of  $\Delta t$  and the ambient temperature.

Since  $T$  fluctuates there is no point in making adjustments based on instantaneous estimates. Instead, we can make use of the average  $\langle T \rangle$  values that are already available. The temperature adjustment (or velocity rescaling) function below would therefore be called from *SingleStep* immediately following the call *AccumProps* (2) used for summarizing the results. The functions are shown below:

---

```
void AdjustTemp ()
{
    real vFac;
    int n;
    vvSum=0
    DO_MOL vvSum +=VLenSq (mol[n].rv);
    vFac=velMag/sqrt (vvSum/ nMol);
    DO_MOL VScale (mol[n].rv, vFac);
}
```

```
void SingleStep ()
{
    ++ stepCount;
    timeNow= stepCount * deltaT;
    LeapfrogStep (1);
    ApplyBoundaryCond ();
    ComputeForces ();
    LeapfrogStep (2);
    EvalProps ();
}
```

---

```
AccumProps (1);
if (stepCount % stepAvg ==0) {
    AccumProps (2);
    PrintSummary (stdout);
    AccumProps (0);
}
}

#define PropZero (v)
    v.sum =0.,
    v.sum2 =0.

#define PropAccum (v)
    v.sum +=v.val,
    v.sum2 +=Sqr (v.val)

#define PropAvg (v, n)
    v.sum /=n,
    v.sum2 =sqrt (Max (v.sum2/ n - Sqr (v.sum), 0.))

#define PropEst (v)
    v.sum,
    v.sum2

void AccumProps (int icode)
{
    if (icode ==0) {
        PropZero (totEnergy);
        PropZero (kinEnergy);
```

---



```
    PropZero (pressure);  
  } else if (icode ==1) {  
    PropAccum (totEnergy)  
    PropAccum (kinEnergy);  
    PropAccum (pressure);  
  } else if (icode ==2) {  
    PropAvg (totEnergy)  
    PropAvg (kinEnergy);  
    PropAvg (pressure);  
  }  
}
```

---

How frequently this adjustment is required, if at all, must be determined empirically; initially it should be omitted since it may interfere with energy conservation. If needed, the interval between adjustments would be specified by the variable

---

```
int stepAdjustTemp;
```

---

The value included in the input data

---

```
Name1 (stepAdjustTemp),
```

---

And the adjustment made by a call from *SingleStep*

```
if (stepCount % stepAdjustTemp == 0 ) AdjustTemp ();
```

---

A possible alternative would be to automate the scheme, applying the adjustment whenever the drift exceeds a given threshold.

Forcing the system to have the correct  $\langle T \rangle$  during the equilibration phase of the simulation uses separate estimates of  $\langle E_k \rangle$ . In SingleStep add (after the call to EvalProps)

---

```
if (stepCount < stepEquil ) AdjustTemp ();
```

---

### 3.3.2 Simulation

This part is the main part of the simulation, which included the equilibration of the system, potential and force calculate, etc..

#### Equilibration

Characterizing equilibrium is by no means an easy task. Averaging over a series of time steps will reduce the fluctuations, but different quantities relax to their equilibrium averages at different rates, and this must also be taken into account when trying to establish when the time is ripe to begin making measurements. Unfortunately, relaxation is generally quite rapid for nanofillers, but thousands times longer for polymers. Therefore, multi-time scale will be used in this simulation. Equilibration can be accelerated by starting the simulation at a higher temperature and later cooling by rescaling the velocities (this is similar, but not identical, to using a larger time step initially); too high a temperature will, however, lead to numerical instability.

One simple measure of equilibration is the rate at which the velocity distribution converges to its expected final form.

The Maxwell distribution:

$$f(v) = \frac{\rho}{(2\pi T)^{d/2}} e^{-v^2/2T} \quad (3.3)$$

In MD units which, after angular integration, becomes

$$f(v) \propto v^{d-1} e^{-v^2/2T} \quad (3.4)$$

The distribution can be measured by constructing a histogram of the velocity values  $\{h_n | n = 1, \dots, N_b\}$ , where  $h_n$  is the number of atoms with velocity magnitude between  $(n-1) \Delta v$  and  $n \Delta v$ ,  $\Delta v = v_m / N_b$ , and  $v_m$  is a suitable upper limit to  $v$ . The normalized histogram represents a discrete approximation to  $f(v)$ .

The function that carries out this computation is

---

```
#define VLen (v) sqrt (VDot (v, v))
#define Min (x1, x2)
  (((x1) < (x2)) ? (x1) : (x2))

void EvalVelDist ()
{
  Real deltaV, histSum;
  int j, n;
```

```
if (countVel == 0) {
    for (j = 0; j < sizeHistVel; j++) hisVel [j] = 0.;
}
deltaV=rangeVel / sizeHistVel;
DO_MOL {
    j = VLen (mol[n].rv) / deltaV;
    ++ histVel [Min (j, sizeHistVel -1)];
}
++ countVel;
if (countVel == limitVel) {
    histSum = 0.;
    for (j=0; j < sizeHistVel; j++) histSum += histVel [j];
    for (j=0; j < sizeHistVel; j++) histVel [j] /= histSum;
    PrintVelDist (stdout);
    countVel = 0
}
}
```

---

Depending on the value of *countVel*, the function will, in addition to adding the latest results to the accumulated total, either initialize the histogram counts, or carry out the final normalization. Other kinds of analysis in subsequent case studies will involve functions that operate in a similar manner.

In order to use this function storage for the histogram array must be allocated, and a number of additional variables declared and assigned values. Variables are

---

```
real *histVel, rangeVel;
```

---

---

```
int countVel, limitVel, sizeHistVel, stepVel;
```

---

And those included in the input data must be added to the array *namelist*,

---

```
NameI (limitVel),  
NameR(rangeVel),  
NameI (sizeHistVel),  
NameI (stepVel),
```

---

Allocation of the histogram array is included in *AllocArrays*,

---

```
AllocMem (histVel, sizeHistVel, real);
```

---

Initialization, in *SetupJob*, requires the additional statement

---

```
void SetupJob ()  
{  
    AllocArrays ();  
    stepCount = 0;  
    InitCoords ();  
    InitVels ();  
    InitAccels ();  
    AccumProps (0);
```

---

```
countVel = 0;  
}
```

---

And the histogram function is called from *SingleStep* by:

---

```
if (stepCount >= stepEquil &&  
    (stepCount - stepEquil) % stepVel == 0) EvalVelDist ();
```

---

Histogram output is provided by the function

---

```
void PrintVelDist (FILE*fp)  
{  
    real vBin;  
    int n;  
  
    printf ("vdist (%.3f)\n", timeNow);  
    for (n = 0; n < sizeHistVel; n++) {  
        vBin = (n + 0.5) * rangeVel / sizeHistVel;  
        fprintf (fp, "%8.3f  %8.3f\n", vBin, histVel [n]);  
    }  
}
```

---

### **Motion in a force field**

The collision prediction process is not affected at all because the same uniform acceleration is experienced by all nanofillers and monomers, so that the computation

for determining the existence of a collision and when it occurs is independent of the field. Between collisions nanofillers and monomers follow parabolic rather than linear trajectories.

It is only the prediction of cell crossings that calls for special attention, because parabolic motion means that it is possible for an nanofiller or monomer to leave a cell through the face (or edge) of entry. The resulting changes to *PredictEvent* follow, where the force field *forceField* is assumed to act in the negative y direction; the algebraic problem solved here is locating the intersection of a parabola with a straight line.

---

```
Vec1 signDir
real h, h1, h2;

VCopy (w, mol[na]. inCell);
if (mol[na].rv.x >0.) ++ w.x;
signDir.x = (mol[na].rv.x <0);
If (forceField.y == 0. && mol[na].rv.y>0 ++w.y;
VMul (w, w, region);
VDiv (w, w, cells);
VSAdd (rs, mol[na].r, 0.5, region);
VVSub (w, rs);
WhenCross (x);
if (forceField.y !=0.) {
    h1 = Sqr (mol[na].rv.y) +2.*forceField.y * w.y;
    if (mol[na].rv.y >0.) {
        h2 = h1 + 2. * forceField.y * region.y/cells.y;
        if (h2 >0.) {
```

---

```
    h= -sqrt (h2);
    signDir.y =1;
} else {
    h= sqrt (h1);
    signDir.y=1;
}
tm.y=-(mol[na].rv.y+h)/forceField.y;
} else {
    WhenCross (y);
    signDir.y = (mol[na].rv.y < 0.);
}
```

---

The role of *signDir* will become clear shortly when we continue with the discussion of changes to *PredictEvent*.

The function *UpdateMol* for updating positions must be modified to allow for parabolic trajectories, with the velocity also being updated.

---

```
void UpdateMol (int id)
{
    real tInt;

    tInt = timeNow - mol[id].time;
    VVSAdd (mol[id].r, tInt, mol[id].rv);
    VVSAdd (mol[id].r, 0.5 * Sqr (tInt), forceField);
    VVSAdd (mol[id].r, tInt, forceField);
    Mol[id].time = timeNow;
```

---



}

---

Because local time variables are associated with each nanofiller or monomer, a similar modification is required in *PredictEvent* for the collision prediction.

---

```
VVSAdd (dr, -0.5 * Sqr (tInt), forceField);  
VVSAdd (dv, -tInt, forceField);
```

---

When checking for energy conservation, allowance should be made for the gravitational potential energy contribution.

### **Hard- wall boundaries**

The boundaries used in this study are all rigid, although the side walls could be replaced by periodic boundaries. These hard walls can be smooth, in which case collisions with the walls are energy-conserving, specular collisions, but in most situations the walls will be rough, so that after undergoing a collisions an nanofiller or monomer loses all memory of its prior velocity. Simply randomizing the velocity direction (and possibly magnitude) will achieve this effect.

Each wall is divided into a series of narrow strips with width typically equal to the monomer diameter; when an nanofiller or monomer collides with the wall the outcome alternates between specular collisions and velocity reversals, depending on the trip involved- a kind of corrugation effect. If the wall is also attached to a thermal reservoir held at constant temperature, as is the case for the top and bottom walls, the velocity magnitude can be changed to the required value.

Collisions with the hard walls require a new form of processing, so an additional class of cell boundary event is introduced; in *SingleEvent*, all cell events are now identified by the modified test.

---

```
if (evldb < MOL_LIMIT + NDIM *2// evldb >= MOL_LIMIT +100)
```

---

The usual cell events are covered by the latter part of the test, while the former, together with  $evldb \geq MOL\_LIMIT$ , accounts for the wall collisions.

The function *ProcessCellCrossing* is modified to handle wall collisions as well as regular cell crossings.

---

```
VecR rs;
VecI irs;
real vFac, vv;
int j, jj;

j= evldb- MOL_LIMIT;
if (j>=100) {
    jj=j-100;
} else {
    jj=j/2;
    VComp (cellRange [j %2], jj)=0;
    VComp (mol[evldbA].r, 0.5, region);
    VDiv (rs, rs, roughWid);
    VCopy (irs, rs)
```

---

```
if (jj !=0 && irs.x %2 ==0) mol[evldA].rv.x *=-1.;
if (jj !=1 && irs.x %2 ==0) mol[evldA].rv.x *=-1.;
if (thermalWall[jj]) {
    vv = VLenSq (mol[ecldA].rv);
    vFac = sqrt (NDIM * wallTemp[j % 2]/vv);
    VScale (mol[evldA].rv, vFac);
}
}
```

---

In *PredictEvent*, changes are required in determining the identity of the cell event about to be scheduled and the range of cells that must be examined.

---

```
#define LimitCells (t)
if (mol[na].inCell.t +cellRangeT[0].t== -1
    cellRangeT[0].t=0;
if (mol[na].inCell.t +cellRangeT[0].t==cells.t
    cellRangeT[0].t=0;

VecI cellRangeT [2];

dir= (tm.x <tm.y) ?0:1;
evCode =100+dir;
if (VComp (mol[na].inCell, dir)==0 &&
    VComp (signDir, dir)==1) evCode = 2*dir;
else if (VComp (mol[na].inCell, dir)==Vcomp (cells, dir)-1 &&
    VComp (signDir)==0) evCode=2*dir +1;
```

---

The system is driven by superimposing a velocity bias in the motion direction when carrying out the velocity randomization; a constant external field could have been used instead.

### 3.3.3 Data output and graphing

The major task of this part is output the data of result and draw the force/area vs distance curve and snapshot, etc..

#### Snapshot

Snapshot of the system configuration are stored on disk by the following function:

---

```
#define SCALE_FAC 32767.

void PutConfig ()
{
    VecR w;
    int blockSize, f0k, n;
    short *rl;
    FILE *fp;

    F0k=1;
    blockSize = (NDIM+1)*sizeof (real)+3*sizeof (int)+nMol*NDIM*sizeof (short);
    if ((fp=fopen (filename[FL_SNAP], "a"))!=0) {
        WriteF (blockSize);
        WriteF (nMol);
        WriteF (region) ;
        WriteF (StepCount);
```

---

```
WriteF (timeNow);
AllocMem (rl,NDIM*nMol, short);
DO_MOL {
    VDiv (w, mol[n].r, region);
    VAddCon (w, w, 0.5);
    VScale (w, SCALE_FAC);
    VToLin (rl, NDIM *n, w);
}
WriteFN (rl, NDIM*nMol);
free (rl);
if (ferror (fp)) f0k=0;
fclose (fp);
} else f0k=0;
if (! F0k) ErrExit (ERR_SNAP_WRITE);
}
```

---

# CHAPTER 4

## MOLECULAR DYNAMICS SIMULATION OF FRACTURE IN POLYMER/ CLAY NANOPATELET NANOCOMPOSITES

### 4.1 INTRODUCTION

In the last decade, nanostructured materials have excited considerable interest in the materials research community partly due to their potentially remarkable mechanical properties. In particular, layered silicate (montmorillonite clay)-reinforced polymer composites have shown considerable promise [1]. Both thermosets and thermoplastics have been incorporated with the layered silicate into nanocomposites [2], including polypropylene [3], polyethylene [4], polystyrene [5], poly(vinyl chloride) [6], polyurethane [7], epoxy [8], nylon [9], rubber [10], recycled poly(ethylene terephthalate) [11] and so on. The addition of clay into these polymers (those glass transition temperatures,  $T_g$ s, are lower than room temperature or nearby (or equal to) room temperature) enhances significantly the mechanical properties of the polymers. Series results indicate that tensile properties of polyurethane and styrene-butadiene and butadiene rubbers were enhanced by incorporation of clay [7,10]. The toughness of nylon6 was improved by addition of clay [9], which  $T_g$  is close to room temperature. However, for epoxy resins, the addition of clay resulted in the decrease in toughness [12]. Until recent, a toughed epoxy-organoclay nanocomposite has not been developed [13], in which hexahydrophthalic acid anhydride-cured bisphenol A diglycidyl ether was used as matrix material for hybrid nanocomposites containing compatibilized polyether liquid rubbers. Without compatibilization, the rubber does not phase separate and flexibilizes the epoxy resin. Toughness is enhanced at the expense of stiffness, strength, and glass temperature. It is believed that the compatibilized polyether liquid rubbers represent the key to toughening. The question

is why clay does work for the improvement of the mechanical properties of those polymers, which  $T_g$ s are lower than room temperature such as polyurethane and rubbers or nearby (or equal to) room temperature, and does not work well for the improvement of toughness of those polymers, which  $T_g$ s are higher than room temperature such as epoxy and polystyrene. Under what kinds of conditions, organoclay can enhance the toughness of epoxy and polystyrene.

## **4.2 MOLECULAR DYNAMICS SIMULATION OF FRACTURE IN POLYMER/ CLAY NANOCOMPOSITE**

### **4.2.1 Background of mechanical properties**

#### **a) Fracture toughness**

Fracture toughness is an indication of the amount of stress required to propagate a pre-existing flaw. It is a very important material property since the occurrence of flaws is not completely avoidable in the processing, fabrication, or service of a material/component. Flaws may appear as cracks, voids, metallurgical inclusions, weld defects, or design discontinuities. Since engineers can never be totally sure that a material is flaw free, it is common practice to assume that a flaw of some chosen size will be present in some number of components and use the linear elastic fracture mechanics (LEFM) approach to design critical components. This approach uses the flaw size and features, component geometry, loading conditions and the material property called fracture toughness to evaluate the ability of a component containing a flaw to resist fracture.

A parameter called the stress-intensity factor ( $K$ ) is used to determine the fracture toughness of most materials. A Roman numeral subscript indicates the mode of fracture and the three modes of fracture are illustrated in the Figure 4.1 Mode I fracture is the condition in which the crack plane is normal to the direction of largest tensile loading. This is the most commonly encountered mode and, therefore, for the

remainder of the material we will consider  $K_I$

The stress intensity factor is a function of loading, crack size, and structural geometry.

The stress intensity factor may be represented by the following equation:

$$K_I = \sigma \sqrt{\pi a \beta} \quad (4.1.)$$

Where:  $K_I$  is the fracture toughness

$\sigma$  is the applied stress

$a$  is the crack length

$\beta$  is a crack length and component geometry factor that is different for each specimen and is dimensionless.

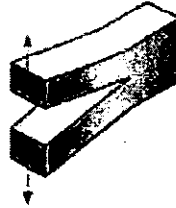


**Figure 4.1** Schematic map of fracture mode.

#### **b) Crack Growth as a Stability Problem**

Consider a body with flaws (cracks) that is subject to some loading; the stability of the crack can be assessed as follows. We can assume for simplicity that the loading is of constant displacement or displacement controlled type (like loading with a screw jack); we can also simplify the discussion by characterizing the crack by its area  $A$ . If we consider an adjacent state of the body as being one with a larger crack (area  $A+dA$ ), we can then assess the strain energy in the two states and evaluate the strain energy release rate. The rate is reckoned with respect to the change in crack area, so if



we use  $U$  for strain energy, the strain energy release rate is numerically  $dU/dA$ . It may be noted that for a body loaded in constant displacement mode, the displacement is applied and the force level is dictated by the stiffness (or compliance) of the body. if the crack grows in size, the stiffness decreases, so the force level will decrease. this decrease in force level under the same displacement (strain) level indicates that the elastic strain energy stored in the body is decreasing - is being released. Hence the term strain energy release rate which is usually denoted with symbol  $G$ . The strain energy release rate is higher for higher loads and larger cracks. If the strain energy so released exceeds a critical value  $G_c$ , then the crack will grow spontaneously. For brittle materials,  $G_c$  can be equated to the surface energy of the (two) new crack surfaces; in other words, in brittle materials, a crack will grow spontaneously if the strain energy released is equal to or greater than the energy required to grow the crack surface(s). The stability condition can be written as

$$\text{elastic energy released} = \text{surface energy created} \quad (4.2)$$

If the elastic energy releases is less than the critical value, then the crack will not grow; equality signifies neutral stability and if the strain energy release rate exceeds the critical value, the crack will start growing in an unstable manner. For ductile materials, energy associated with plastic deformations has to be taken into account. When there is plastic deformation at the crack tip (as occurs most often in metals) the energy to propagate the crack may increase by several orders of magnitude as the work related to plastic deformation may be much larger than the surface energy. In such cases, the stability criterion has to restated as

$$\text{elastic energy released} = \text{surface energy} + \text{plastic deformation energy} \quad (4.3)$$

Practically, this means a higher value for the critical value  $G_c$ . From the definition of  $G$ , we can deduce that it has dimensions of work (or energy)/area or force/length. For

ductile metals  $G_{Ic}$  is around 50 to 200 kJ/m<sup>2</sup>, for brittle metals it is usually 1-5 and for glasses and brittle polymers it is almost always less than 0.5. The I subscript here refers to mode I or crack opening mode as described in the section on fracture mechanics. The problem can also be formulated in terms of stress instead of energy, leading to the terms stress intensity factor  $K$  (or  $K_I$  for mode I) and critical stress intensity factor  $K_c$  (and  $K_{Ic}$ ). These  $K_c$  and  $K_{Ic}$  (etc) quantities are commonly referred to as fracture toughness, though it is equivalent to use  $G_c$ . Typical values for  $K_{Ic}$  are 150 MN/m<sup>3/2</sup> for ductile (very tough) metals, 25 for brittle ones and 1-10 for glasses and brittle polymers. Notice the different units used by  $G_{Ic}$  and  $K_{Ic}$ . Engineers tend to use the latter as an indication of toughness.

Tensile properties are the ability of a material to resist breaking under tensile stress. It is one of the most important and widely measured properties of materials used in structural applications. Tensile properties indicate how the material will react to forces being applied in tension. A tensile test is a fundamental mechanical test where a carefully prepared specimen is loaded in a very controlled manner while measuring the applied load and the elongation of the specimen over some distance. Tensile tests are used to determine the modulus of elasticity, elastic limit, elongation, proportional limit, and reduction in area, tensile strength, yield point, yield strength and other tensile properties.

For this test, shown in Figure 4.2, plastic samples are either machined from stock shapes or injection molded. The tensile testing machine pulls the sample from both ends and measures the force required to pull the specimen apart and how much the sample stretches before breaking.

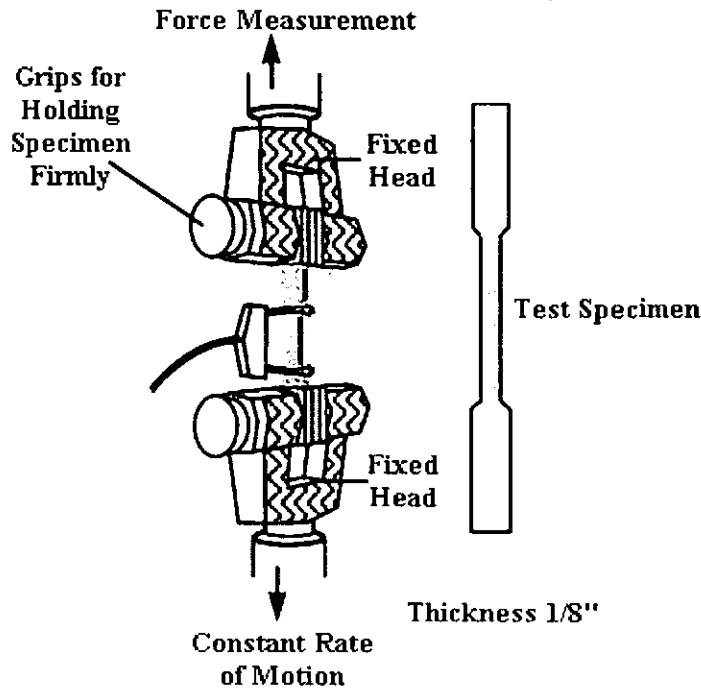


**Figure 4.2** Schematic of tensile test.

The main product of a tensile test is a load versus elongation curve which is then converted into a stress versus strain curve. Since both the engineering stress and the engineering strain are obtained by dividing the load and elongation by constant values (specimen geometry information), the load-elongation curve will have the same shape as the engineering stress-strain curve. The stress-strain curve relates the applied stress to the resulting strain and each material has its own unique stress-strain curve. A typical engineering stress-strain curve is shown below. If the true stress, based on the actual cross-sectional area of the specimen, is used, it is found that the stress-strain curve increases continuously up to fracture (shown in Figure 4.3.).

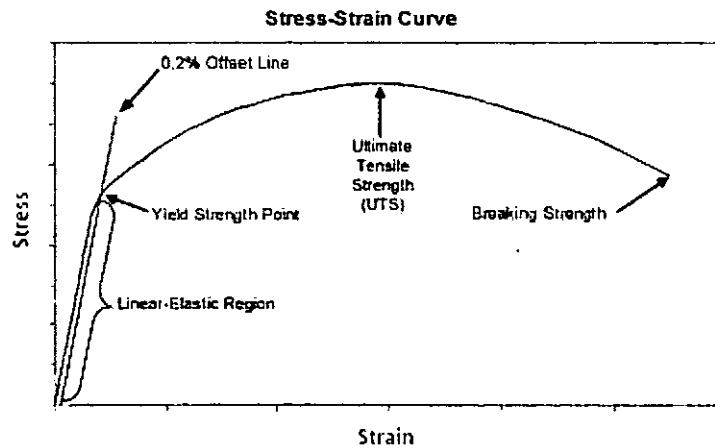


**Figure 4.3** Schematic of stress-strain curve.

**c) Ultimate tensile strength (UTS) or tensile strength at break:** The ultimate tensile strength (UTS) or, more simply, the tensile strength, is the maximum engineering stress level reached in a tension test. The strength of a material is its ability to withstand external forces without breaking. In brittle materials, the UTS will be at the end of the linear-elastic portion of the stress-strain curve or close to the elastic limit. In ductile materials, the UTS will be well outside of the elastic portion into the plastic portion of the stress-strain curve.

On the stress-strain curve Figure 4.3., the UTS is the highest point where the line is momentarily flat. Since the UTS is based on the engineering stress, it is often not the same as the breaking strength. In ductile materials strain hardening occurs and the stress will continue to increase until fracture occurs, but the engineering stress-strain curve may show a decline in the stress level before fracture occurs. This is the result of engineering stress being based on the original cross-section area and not accounting for the necking that commonly occurs in the test specimen. The UTS may not be completely representative of the highest level of stress that a material can support, but the value is not typically used in the design of components anyway. For ductile metals the current design practice is to use the yield strength for sizing static components.

However, since the UTS is easy to determine and quite reproducible, it is useful for the purposes of specifying a material and for quality control purposes. On the other hand, for brittle materials the design of a component may be based on the tensile strength of the material.

**d) Tensile Elongation:**

The ultimate elongation of an engineering material is the percentage increase in length that occurs before it breaks under tension. Ultimate elongation values of several hundred percent are common for elastomers and film/package polyolefins. Rigid plastics, especially fiber reinforced ones, often exhibit values under 5%. The combination of high ultimate tensile strength and high elongation leads to materials of high toughness.

**e) Tensile Modulus of Elasticity:**

The tensile modulus is the ratio of stress to elastic strain in tension. A high tensile modulus means that the material is rigid - more stress is required to produce a given amount of strain. In polymers, the tensile modulus and compressive modulus can be close or may vary widely. This variation may be 50% or more, depending on resin type, reinforcing agents, and processing methods. The tensile and compressive moduli are often very close for metals.

**f) Yield Point:**

In ductile materials, at some point, the stress-strain curve deviates from the straight-line relationship and Law no longer applies as the strain increases faster than the stress. From this point on in the tensile test, some permanent deformation occurs in the specimen and the material is said to react plastically to any further increase in load or stress. The material will not return to its original, unstressed condition when the load is removed. In brittle materials, little or no plastic deformation occurs and the material fractures near the end of the linear-elastic portion of the curve.

With most materials there is a gradual transition from elastic to plastic behaviour, and the exact point at which plastic deformation begins to occur is hard to determine. Therefore, various criteria for the initiation of yielding are used depending on the sensitivity of the strain measurements and the intended use of the data. For most engineering design and specification applications, the yield strength is used. The yield strength is defined as the stress required producing a small, amount of plastic deformation. The offset yield strength is the stress corresponding to the intersection of the stress-strain curve and a line parallel to the elastic part of the curve offset by a specified strain (in the US the offset is typically 0.2% for metals and 2% for plastics). In Great Britain, the yield strength is often referred to as the proof stress. The offset value is either 0.1% or 0.5%

To determine the yield strength using this offset, the point is found on the strain axis (x-axis) of 0.002, and then a line parallel to the stress-strain line is drawn. This line will intersect the stress-strain line slightly after it begins to curve, and that intersection is defined as the yield strength with a 0.2% offset. A good way of looking at offset yield strength is that after a specimen has been loaded to its 0.2 percent offset yield strength and then unloaded it will be 0.2 percent longer than before the test. Even though the yield strength is meant to represent the exact point at which the material becomes permanently deformed, 0.2% elongation is considered to be a tolerable amount of sacrifice for the ease it creates in defining the yield strength.

#### **g) Linear-Elastic Region and Elastic Constants**

As can be seen in the Figure 4.3, the stress and strain initially increase with a linear relationship. This is the linear-elastic portion of the curve and it indicates that no plastic deformation has occurred. In this region of the curve, when the stress is reduced, the material will return to its original shape. In this linear region, the line obeys the relationship defined as Hooke's Law where the ratio of stress to strain is a

constant.

The slope of the line in this region where stress is proportional to strain and is called the modulus of elasticity or Young's modulus. The modulus of elasticity ( $E$ ) defines the properties of a material as it undergoes stress, deforms, and then returns to its original shape after the stress is removed. It is a measure of the stiffness of a given material. To compute the modulus of elastic, simply divide the stress by the strain in the material. Since strain is unitless, the modulus will have the same units as the stress. The modulus of elasticity applies specifically to the situation of a component being stretched with a tensile force. This modulus is of interest when it is necessary to compute how much a rod or wire stretches under a tensile load.

There are several different kinds of moduli depending on the way the material is being stretched, bent, or otherwise distorted. When a component is subjected to pure shear, for instance, a cylindrical bar under torsion, the shear modulus describes the linear-elastic stress-strain relationship.

In conventional tensile test can only get the macroscopically results, these are statistical results of molecular motions from statistical thermodynamics. The conventional tensile test cannot open out the motions and interactions between each molecular then the computer molecular dynamics simulation is introduced. By virtue of the powerful operation ability of computer, to know what happening between the molecules during the test is possible. This chapter will discuss how nanofillers affect the fracture behaviour of polymers.

#### **4.2.2 Effect of incorporation of nanoplatelets on fracture**

From the published papers [1-11], it can be considered that nanoplatelets can affect to the polymers by the incorporation with them. But how the nanoplatelets affect a polymer is still not very clear from the microstructure point of view. How do the

interactions between molecules and interactions between molecules and nanoplatelets work? In this section, we will answer these questions.

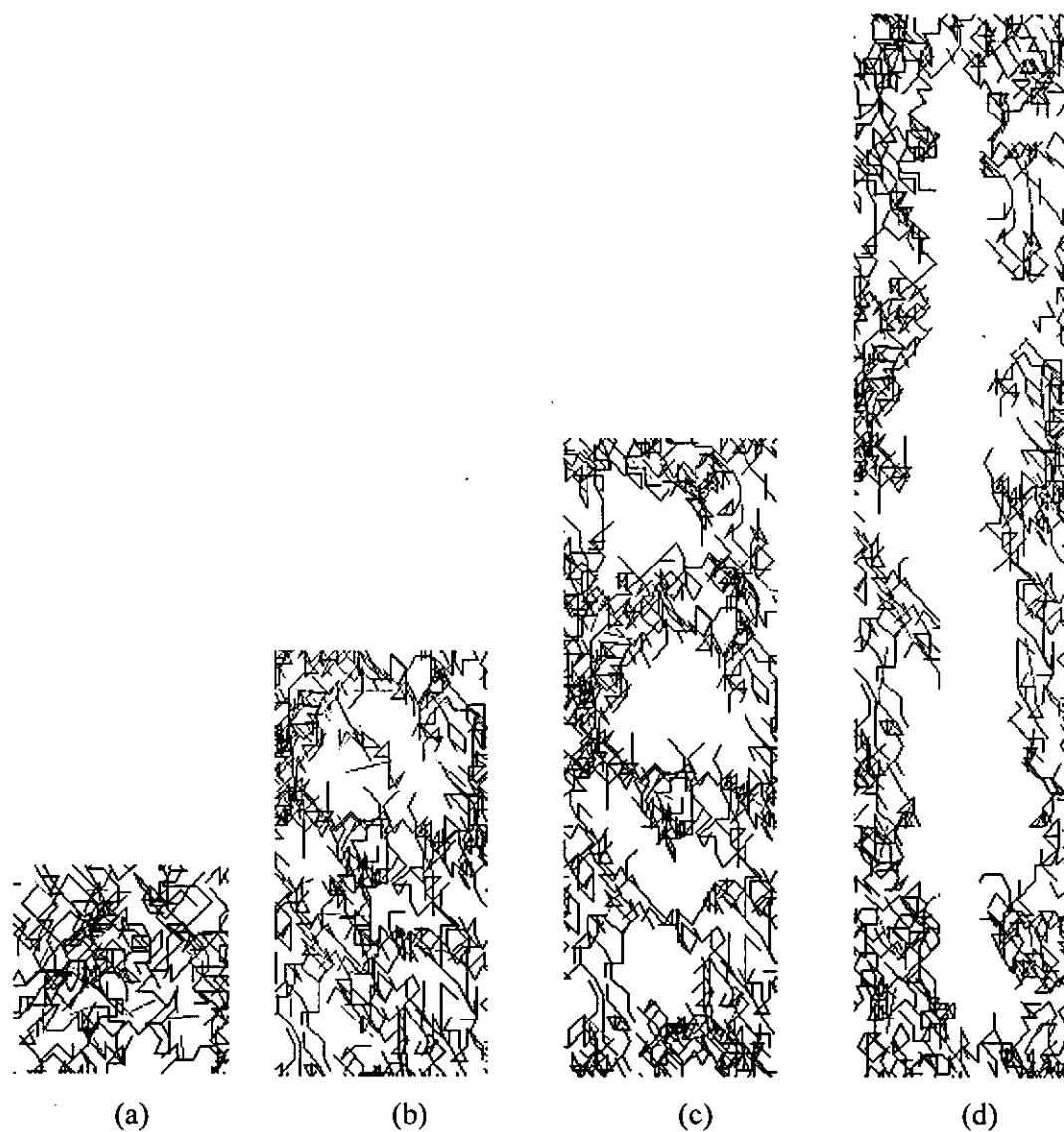


**Figure 4.4** Snapshots of the simulation at (a)0%, (b)100%, (c)200%, (d)400% elongation at  $1.1 T_g$  with 5wt.% nanoplatelets.



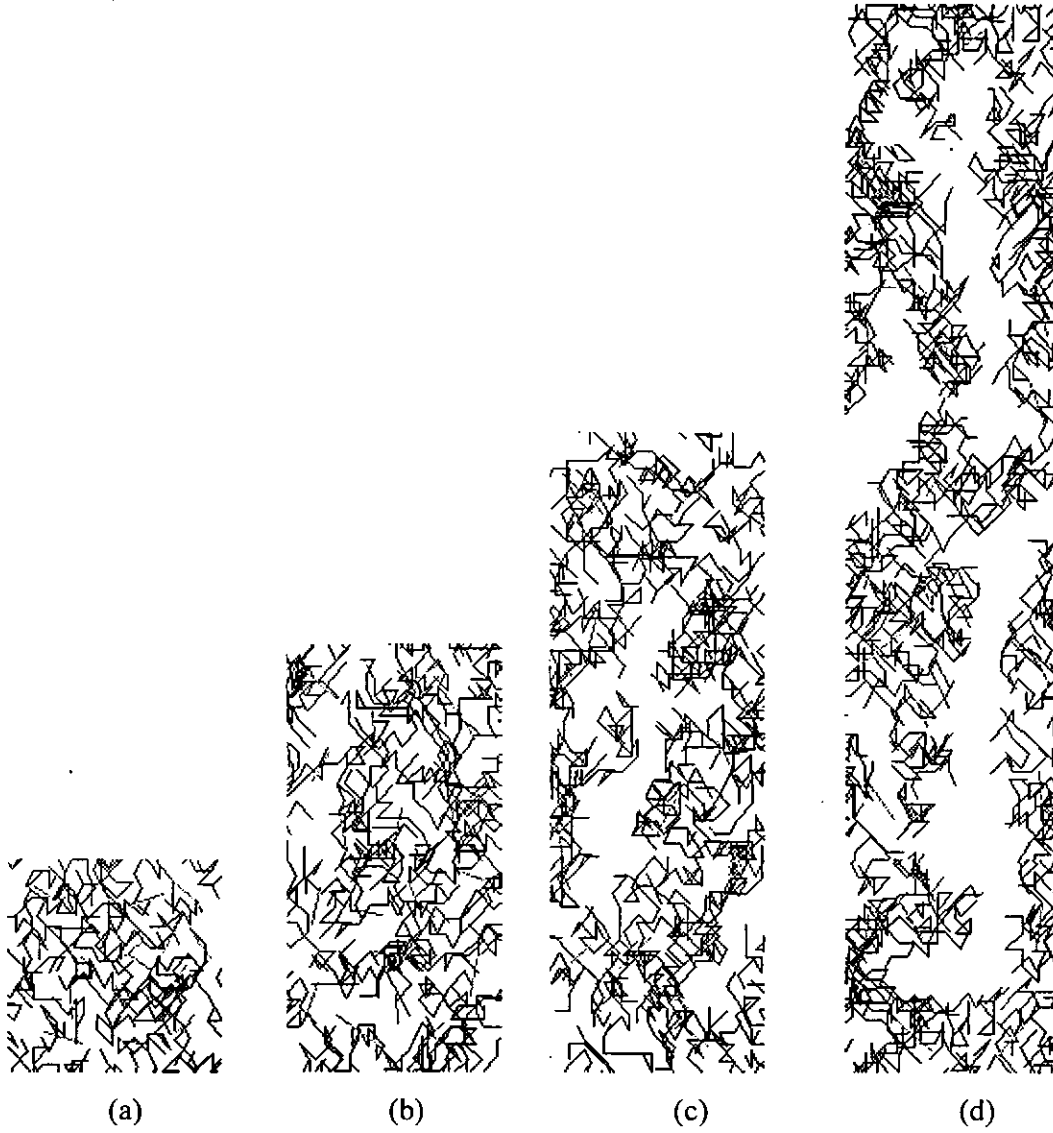


**Figure 4.5** MD snapshots looking from x- axis direction at at (a)0%, (b)100%, (c)200%, (d)400% elongation  $0.4 T_g$ ,  $\sigma_f = 3\sigma$ ,  $\varepsilon_{fp} = 4\varepsilon$  and  $\nu = 0.03\sigma/\tau$ , with 5wt.% nanoplatelets

Figures 4.4 shows a MD snapshots looking from x-axis direction at  $1.1 T_g$ .  $T_g (= \varepsilon/k_B)$  is the glass transition temperature of the polymer. Figures 4.5 shows a MD snapshots looking from x-axis direction at  $0.4 T_g$ . All MD snapshots corresponded to  $\sigma_f = 3\sigma$ ,

$\varepsilon_{fp} = 4\varepsilon$  and  $\nu = 0.03\sigma/\tau$ , which  $\sigma_f$  is the length scale of nanoplatelet,  $\varepsilon_{fp}$  is the characteristic energy of the nanoplatelet,  $\tau$  is the characteristic time, which is defined as  $\tau = \tau_{LJ} \equiv (m \sigma^2 / \varepsilon)^{1/2}$ . The effect of the difference of the relaxation time of the polymer and that of the nanoplatelet was not considered here. It can be seen that the polymer composite always presents a large amount of the nanoplatelets in the region around the cavities at above its  $T_g$

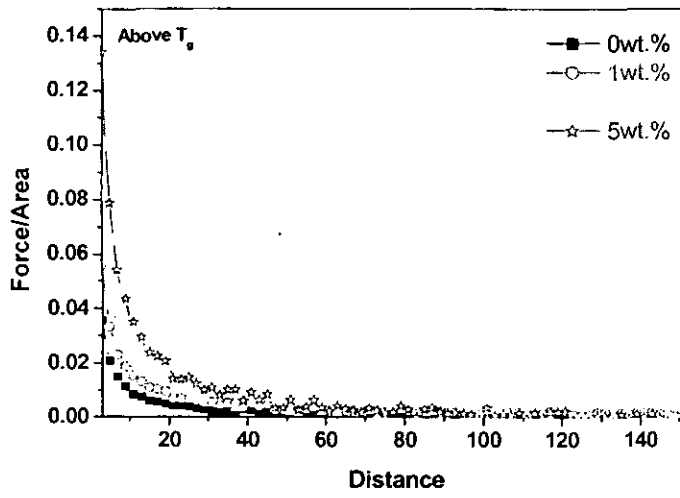


**Figure 4.6** Force/area curves vs. distance with different contents of the nanoplatelets at 1.1  $T_g$ .

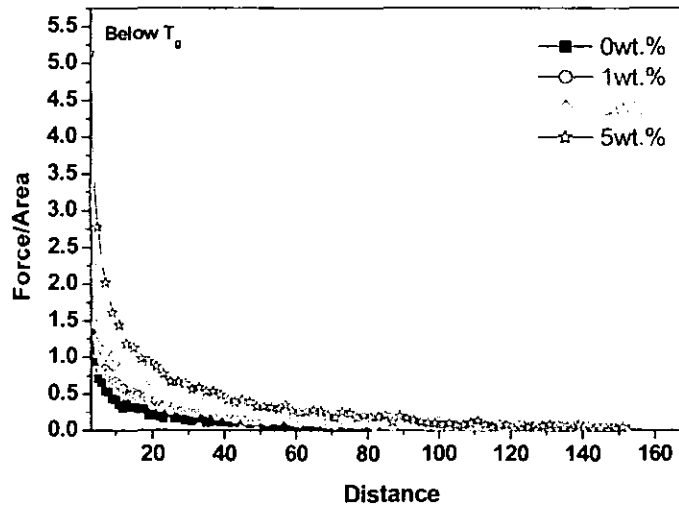


**Figure 4.7** Force/area curves vs. distance with different contents of the nanoplatelets at  $0.4T_g$ .

Figure 4.6 and 4.7. shows the Force/ area curves vs. distance with different contents of the nanoplatelets at  $1.1 T_g$  and  $0.4T_g$ , respectively. It can be seen that the addition of the nanoplatelets has a significant influence on the force/area curve vs. distance of the polymer nanocomposite at either above or below its  $T_g$ . With increasing the content of nanoplatelets, the strength of the force/area curve vs. distance increased.

Figures 4.8 and 4.9 show the normalized work,  $W^*$ , to failure.  $W^*$  is defined as the work to failure of the polymer nanocomposite after cavitation has occurred divided by the work to failure of non-nanoplatelet system. Results indicate that  $W^*$  is increased with increasing the content of the nanoplatelets for both of cases at above and below  $T_g$  of the polymer. It can be seen that the increase in  $W^*$  is not a linear with the content of the nanoplatelets at above  $T_g$  of the polymer (Figure 4.8). With increasing the content of the nanoplatelets, the magnitude of the increase is small in the range of between 1Wt.% and 3Wt.% of the nanoplatelets. At 5Wt.% of the nanoplatelets,  $W^*$  has a significant increase. Such phenomenon has been observed in polyurethane-

organoclay nanocomposites experimentally [14]. However there is a linear relationship between  $W^*$  and the content of the nanoplatelets at below  $T_g$  of the polymer (Figure 4.9). It can be found that the contribution of the nanoplatelets to the enhancement of the fracture strength of the polymer at below its  $T_g$  is less than at above its  $T_g$ . Nevertheless, the addition of the nanoplatelets can enhance the fracture strength for polymers at either above or below their  $T_g$ s when the difference of the relaxation time between the polymer and the nanoplatelet is not considered.

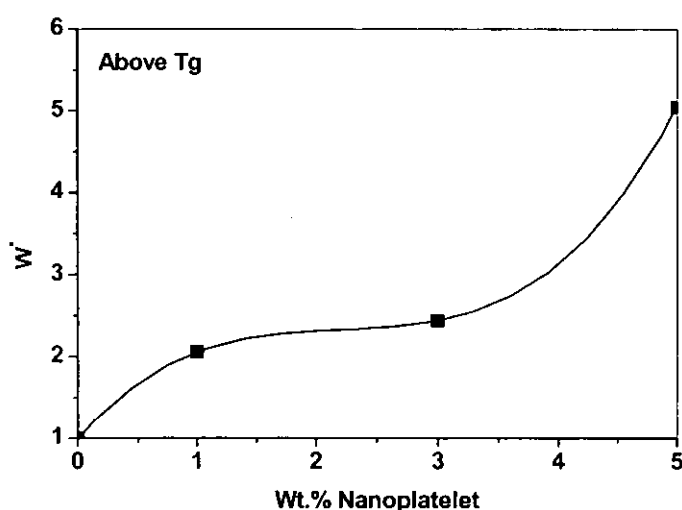


**Figure 4.8** Normalized work,  $W^*$ , to failure with content of nanoplatelets at 1.1  $T_g$ .

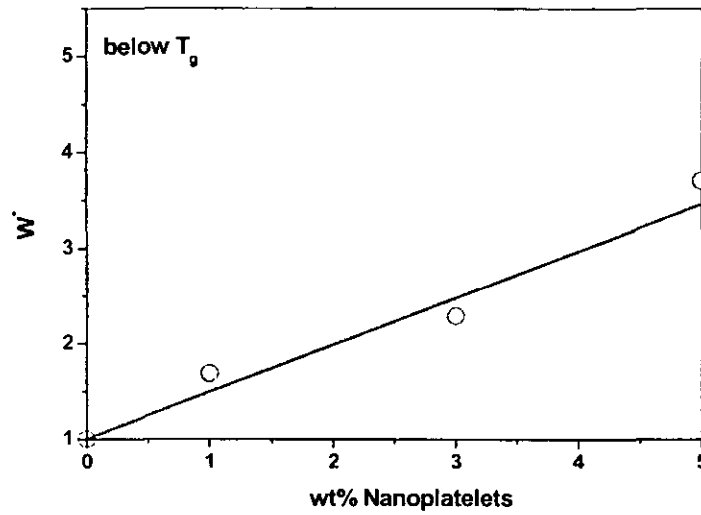


**Figure 4.9** Normalized work,  $W^*$ , to failure with content of nanoplatelets at  $0.4T_g$ .

During deformation of the polymer nanocomposite at above its  $T_g$ , the nanoplatelets could create temporary local regions in which physical crosslinks between the polymer chains could be formed because of the strong interaction between the polymer chains and the nanoplatelets, and the high mobility of the nanoplatelets.

The local region can make them much stronger to resist the growth of cavities and dissipate energy. At below its  $T_g$ , because the polymer is in the glassy state, the mobility of the nanoplatelets is restricted. Therefore it is very difficult to create the temporary local region, which will result in the weakness in the enhancement of the fracture strength. When the testing temperature is below  $T_g$ , because the polymer is in its glassy state, therefore it is difficult to create any temporary cross links or local region between polymer chains by the nanoplatelets. The enhancement of the failure strength of the polymer will be a little.

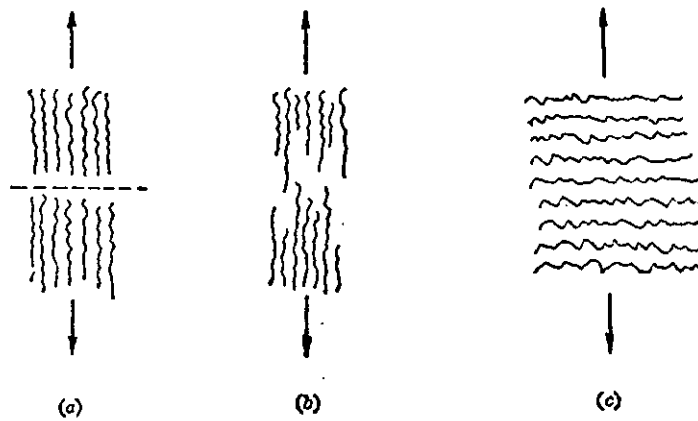


**Figure 4.10** Schematic of polymer fracture. (a). The break of chemical bonds; (b). The mutual slippages between molecules; (c). The destroy of Van der Waals interactions between molecules or hydrogen bonds.

The ability of the polymer to resist the breakage of loadings is the chemical bonds internal molecular, Van der Waals interactions between molecular and hydrogen bonds. Ignore all other complicated effects, the process of polymer fracture can be summarized in 3 types (shown in Figure 4.10),

- (a). Break of chemical bonds.
- (b). Mutual slippages between molecules.
- (c). Destroy of Van der Waals interactions between molecules or hydrogen bonds.

If the polymer fails in type a of Figure 4.10, the fracture of the polymer leads to the break of all chemical bonds. In fact, when the material is loaded, no structure can snap all chemical bonds in one section at the same time, even it is a crystal polymer with high orientation; If the polymer fails in type b of Figure 4.10, the fracture of the mutual slippages between molecules has to destroy all the Van der Waals interactions or hydrogen bonds. In type c of Figure 4.10, the array of molecules is plumbed with the direction of loading. Part of the Van der Waals interactions or hydrogen bonds of

polymers are destroyed, while the polymers fracture.

In a real material, the degree of polymer orientation is too low to form a perfect structure, even with high orientation. Due to limitation of the length of the real polymer chains, the polymer chains always have some unorientation part more or less. The breakage will occur in the Van der Waals interactions and hydrogen bonds in the unorientation part of material while the normal fracture of material occurs. After that, the stress will centralize to the main orientation polymer chains. Although the strength of chemical bonds is much stronger than the interactions between molecules (normally 10 to 20 times), but too less main orientation polymer chains withstand the loading directly, the material will fail at last. When the nanoplatelets are added into polymer, they will build up an extra vinculum by the interactions between nanoplatelets and polymer chains. Due to stronger interactions between nanoplatelets and polymer chains the more energy will be dissipated during the fracture. This is exhibited that the work to break in the mechanical processes will be increased. It can be considered that the additional dissipative energy is a result of the mobility of nanoplatelets. Since the size of nanoplatelets is comparable with the polymer chains (in our simulation the size of nanoplatelets is 0.6 times the radius of gyration of the polymer chain), the time scale for the motion of nanoplatelets and the polymer chains are also comparable. Therefore, during the deformation, the nanoplatelets can create temporary cross- links between the polymer chains, accordingly a local region can be created to enhanced strength and retard the growth of the cavity.

The effect of the nanoplatelets on the fracture of the polymer is also exhibited by the ability of the nanoplatelets to stop the growth of the cavity. As it is well known, polymer failure starts from crack [16]. The cavity nucleation is formed by crack diffusion. As the crack tip move through the polymer, the cavities merge to form a fracture plane. Finally, the polymer goes to fail.

Crack comes from craze. The craze always occurs near the surface of material [16]. The part which engenders the crack is called craze body. The craze body is different from the craze. The mass of craze body is not zero. It will include the orientational polymer (shown in Figure 4.11). The surface of craze is plumbed with the direction of outside loading.

The appearance of craze has the lowest stress called critical stress [16]. There is no craze occurred if the stress is lower than the critical stress. When the stress is higher than the critical stress, the more stress, the faster of the appearance and growth of craze. On the other hand, the appearance of craze also has the lowest elongational rate called critical elongational rate. The craze will occur once the elongation of material reaches the critical elongational rate [16]. The polymer chains in the craze are orientational, the craze does only orientate the molecules of the polymer which are in the craze, but also reduces the density. When the growth of craze reaches a limitation, the craze will fracture to a crack [16].

When the nanoplatelets are added into polymer, if the testing temperature is higher than its  $T_g$ , the Van der Waals interactions and hydrogen bonds will be formed between molecules and nanoplatelets. Thereby, the tensile strength of the material will be enhanced. This will be due to the enhancement of the critical stress of the material. On the other hand, the nanoplatelets will create temporary cross links between polymer chains. This will increase the toughness of the polymer, which will also make the polymer more difficultly to be elongated. Therefore, the more energy and outside loading will be needed to reach the critical elongational rate.



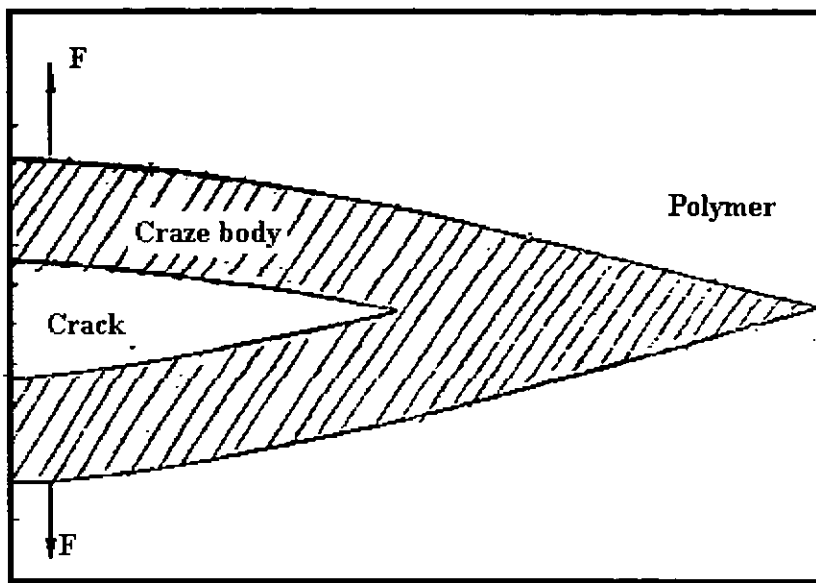


**Figure 4.11** Profile chart of crack tip. If the elongation reaches the critical elongation, then the craze body will become crack. As the crack tip increases incessantly, the crack moves through the material [15].

But the matter will be different when testing temperature is below  $T_g$  of the polymer. As we have discussed above, the enhancement of tensile strength by the nanoplatelets is limited. The enhancement of critical stress of material is limited. Therefore the contribution of the nanoplatelets to the material critical elongational rate will be very little.

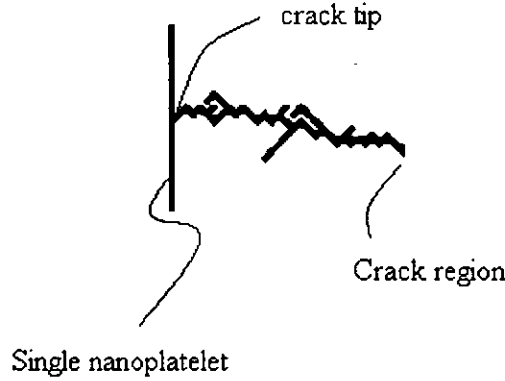


**Figure 4.12** Schematic of how the nanoplatelets stop crack as a barrier. In the figure, the crack was moving from the crack region. The nanoplatelet blocked the movement of crack on its way as a barrier.

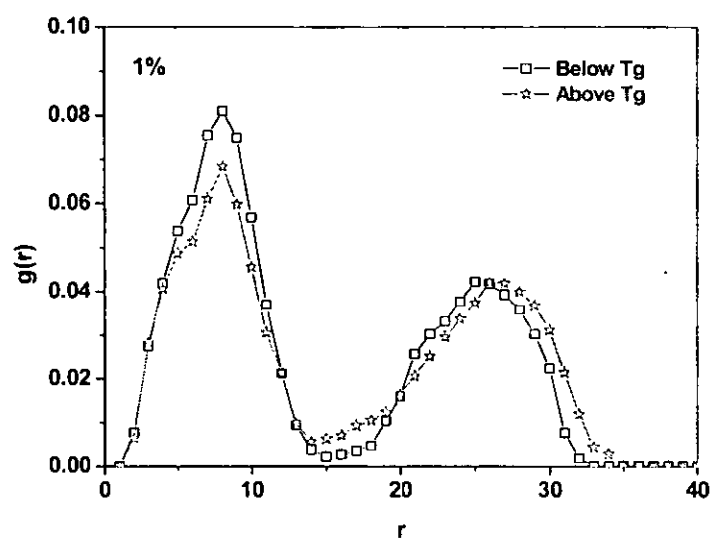
It can also be found in molecular dynamics simulation that nanoplatelets can defend the polymer effectively by stopping the growth of cracks. Normally, the toughness of the nanoplatelets is much higher than polymer chains. The size of the nanoplatelets is too large for the crack tip to move cross over, therefore the movement of the crack tip will be stopped by the nanoplatelets, Furthermore, and the growth of cavities will go to slow down [16].

Figure 4.13, 4.14 and 4.15 show the nanoplatelet – nanoplatelet correlation function with the contents of nanoplatelets various from 1% to 5% by weight. Correlation function is always connected to many properties of system, such as average potential energy and pressure etc. In our simulations, the effect of the ability of the nanoplatelets to resist cavity growth can be determined by calculating the nanoplatelet

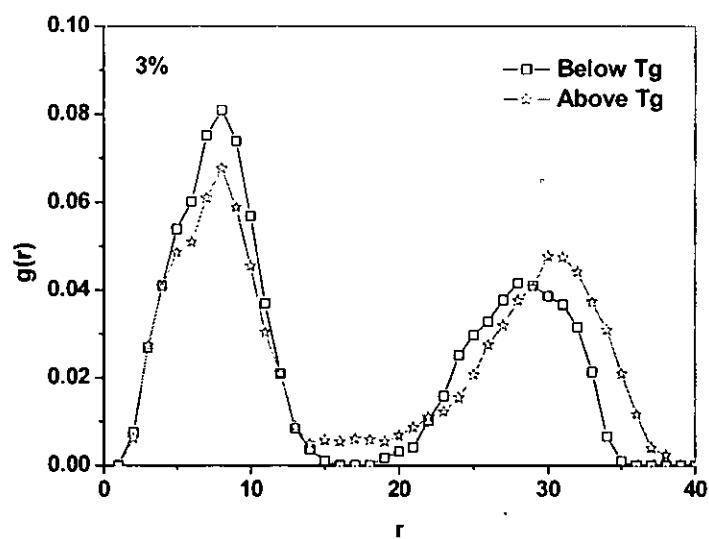
– nanoplatelet correlation function,  $g(r) = \frac{n(r)}{\sum n(r)}$  [17]. Where  $n(r)$  is the number

of the nanoplatelets that are located at a distance  $r$  from a given nanoplatelet.  $g(r)$  is normalized by the total number of nanoplatelet pairs in the system. The quantity of  $g(r)$  represents the relative frequency of nanoplatelets in the molecular dynamics simulation being situated near  $r$ , or simply means fluid density at position  $r$ . There are two peaks in  $g(r)$  shown in Figure 4.14, 4.15 and 4.16. The first peak of the system at above  $T_g$   $g(r)$  was shifted to the right and became slightly narrow and low than that below  $T_g$ . The second peak of  $g(r)$  above  $T_g$ , was shifted to the right compared with the second peak of  $g(r)$  below  $T_g$  as well. The height of second peak below  $T_g$  with the content of nanoplatelet from 1wt.% to 5wt.% shows no significant change, which seems that  $g(r)$  is not sensitive to the content of the nanoplatelet. The height of second peak above  $T_g$  with the content of nanoplatelet from 1wt.% to 5wt.% increase with increasing content of the nanoplatelets.

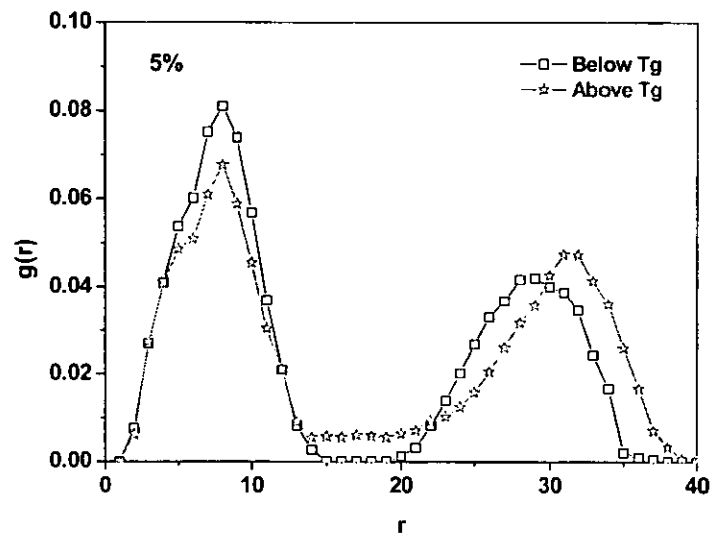
This means that the polymer could fail by cavitation. The second peak shows while the depletion of the nanoplatelets in the region where the cavity is formed. The amount of the nanoplatelets which were present in the simulation system of polymer nanocomposite that bridged the cavity was a measure of its ability to resist the growth of the cavity, as the more nanoplatelets was present, the more the force necessary for the growth of the cavity. Results shown in Figure 4.13, 4.14 and 4.15 indicate the ability of nanospace to resist the growth of the cavity is increased with increasing nanoplatelets. From Figure 4.13, it can be seen that the system at above  $T_g$  always shows a larger amount of the nanoplatelet present in the bridge region during the simulation than at below  $T_g$ . And as the increase of content of nanoplatelets, the amount of nanoplatelet present in the bridge region is increasing as well. Because the nanoplatelets have enough mobility to form the temporary bonds even the local region at above  $T_g$ , the temporary bonds and local region can dissipate energy superfluity. But the mobility of nanoplatelets will be reduced at below  $T_g$ .



**Figure 4.13** Nanoplatelet – nanoplatelet correlation function,  $g(r)$  with 1wt.% nanoplatelets.



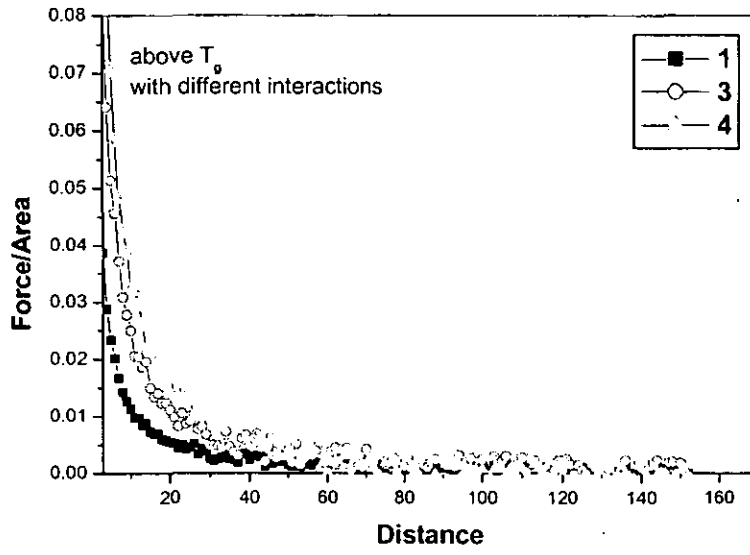
**Figure 4.14** Nanoplatelet – nanoplatelet correlation function,  $g(r)$  with 3wt.% nanoplatelets.



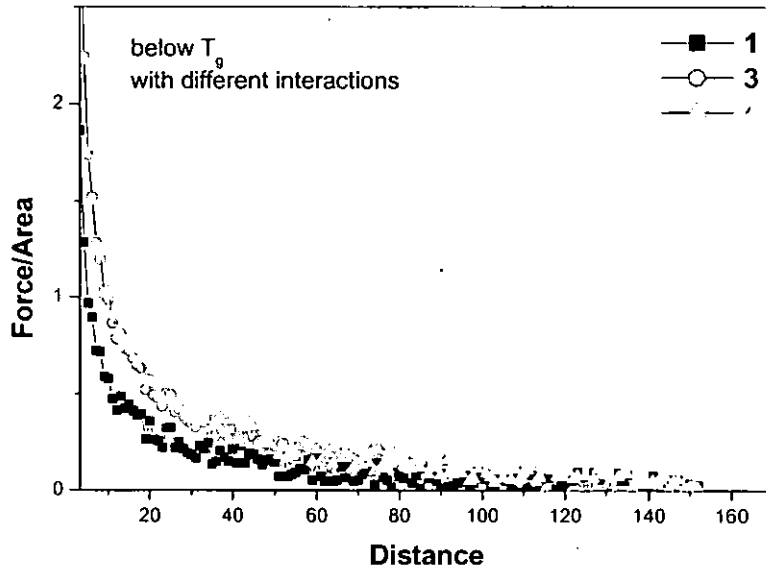
**Figure 4.15** Nanoplatelet – nanoplatelet correlation function,  $g(r)$  with 5wt.% nanoplatelets.

#### 4.2.3 Effect of interaction between nanoplatelets and polymers on fracture

In this section the interaction strength between molecules and nanoplatelets under a fixed content of nanoplatelets will be studied.



**Figure 4.16** Force/ Area vs distance with different interactions between nanoplatelets (3wt.%) and polymer chains, where  $\sigma_f = 3\sigma$ ,  $\varepsilon_{fp} = 4\varepsilon$ ,  $\nu = 0.03\sigma/\tau$  and with the temperatures above  $T_g$ ,  $T = 1.1\varepsilon/k_B$ .



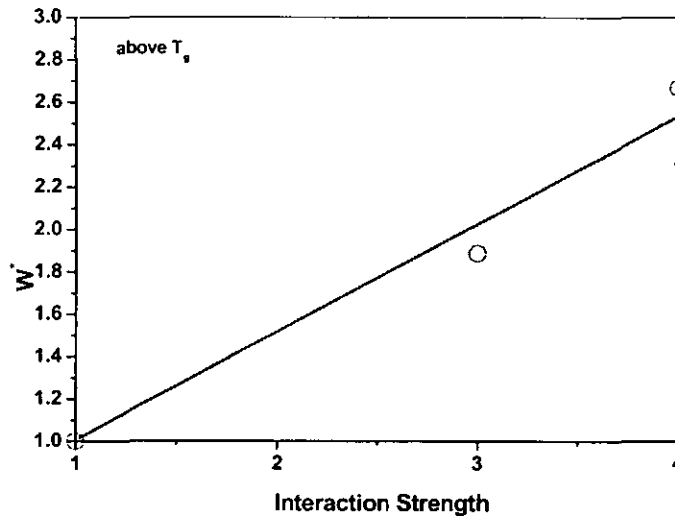
**Figure 4.17** Force/ Area vs distance with different interactions between nanoplatelets (3wt.%) and polymer chains, where  $\sigma_f = 3\sigma$ ,  $\varepsilon_{fp} = 4\varepsilon$ ,  $\nu = 0.03\sigma/\tau$  and with the temperatures below  $T_g$ ,  $T = 0.3\varepsilon/k_B$ .

Figure 4.16 and 4.17 show that the fracture strength and the extension at break of the polymer nanocomposite increased evidently while the interactions between nanoplatelets and polymer chains were boosted up where testing temperature was above  $T_g$ , but weak at testing temperature below  $T_g$ .

As discussed above the nanoplatelets can enhance the mechanical properties by interactions between the nanoplatelets and polymer chains. The increase of the interactions between nanoplatelets and polymer chains could include the increase of the Van der Waals interactions between molecules or hydrogen bonds or both of them. When the interactions are increased, the connection between nanoplatelets and polymer chains will be more compact. Therefore, much more energy will be needed

to break the connection between nanoplatelets and polymer chains.

Also the stability of the nanocomposite will be increased if the local region is more stable. It will be more difficult to make the polymer chains move from the original position to other. This will increase the difficulty of the orientation of the polymer chains when the external loading is added. This will resist the crack tip to move through the material and could be due to the enhancement of the resistibility to the growth of crack. Therefore, the effect of the increase of the interactions between the nanoplatelets and polymer chains could enhance the mechanical properties of polymer nanocomposites.



**Figure 4.18** Normalized work to failure,  $W^*$ , as a function of the different interactions between nanoplatelets (3wt.%) and polymer chains, where  $\sigma_f = 3\sigma$ ,  $\varepsilon_{fp} = 4\varepsilon$  and the pulling velocity was  $\nu = 0.03\sigma/\tau$  at the temperature above  $T_g$ ,  $T = 1.1\varepsilon/k_B$ .



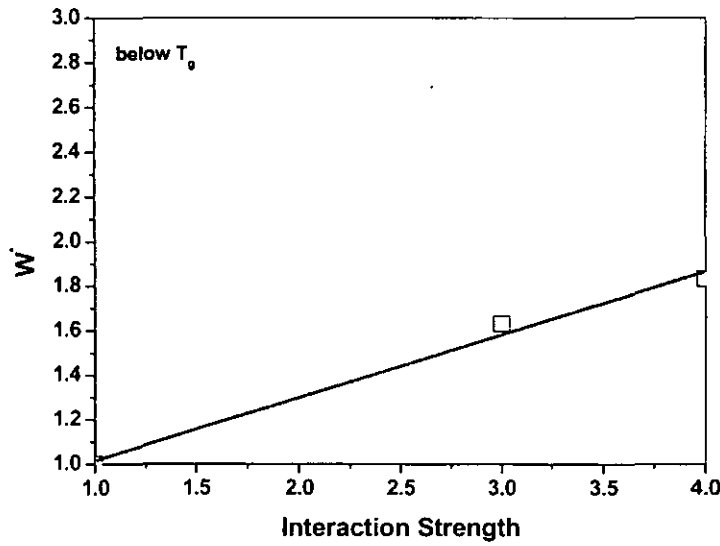


**Figure 4.19** Normalized work to failure,  $W^*$ , as a function of the different interactions between nanoplatelets (3wt.%) and polymer chains, where  $\sigma_f = 3\sigma$ ,  $\varepsilon_{fp} = 4\varepsilon$  and the pulling velocity was at the temperature below  $T_g$ ,  $T = 0.3\varepsilon/k_B$ .

Figure 4.18 and 4.19 show that when testing temperature is above  $T_g$ , the normalized work to failure,  $W^*$ , grow rapidly as the interactions between nanoplatelets and polymer chains is increased. The normalized work to failure was also increased when testing temperature was below  $T_g$ , but the range strength was reduced compared to above  $T_g$ .

The pair correlation function  $g(r)$  is related to the probability of finding the centre of a particle a given distance from the centre of another particle. For short distances, this is related to how the particles are packed together. For large distances, the probability of finding two particles with a given separation is essentially constant. The pair correlation function  $g(r)$  accounts for these factors by normalizing by the density; thus at large values of  $r$  it goes to 1, uniform probability. The following figure is a typical curve of pair correlation function of the Lennard-Jones liquid.

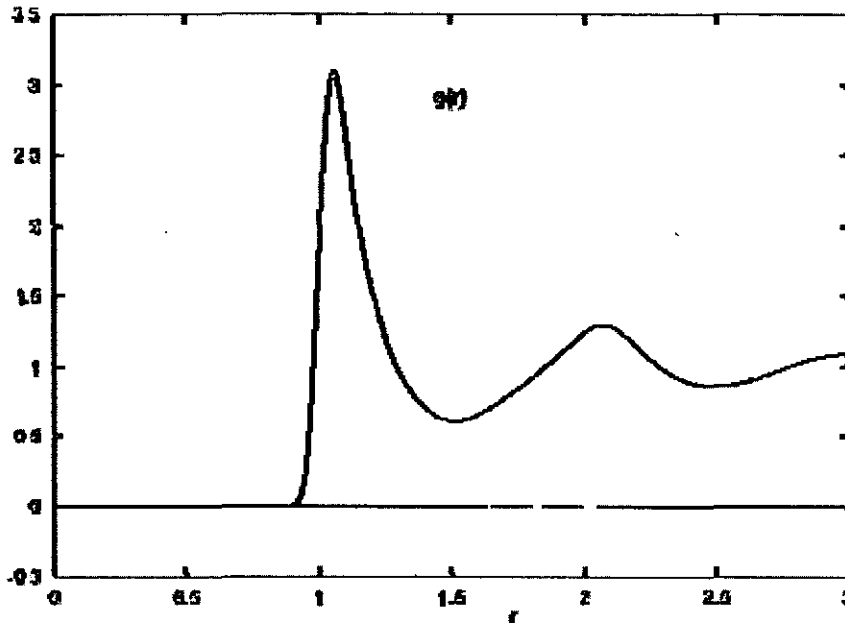


**Figure 4.20** Pair correlation function of the Lennard-Jones liquid

From Figure 4.20, it is found that there is only one peak in the  $g(r)$  curve of pair correlation function of the Lennard-Jones liquid, due to the density of liquid is uniformity.

Figure 4.21, 4.14, and 4.22 show the curve of nanoplatelet – nanoplatelet correlation function with the interaction strength between nanoplatelets and polymers. It was known from the nanoplatelet – nanoplatelet correlation function that the simulation system was failed by cavitation. It is found that there are no obvious variations of the first peak in heights of the successive maxima for the cases with different interaction strength, also, the positions remain almost unchanged. The ascending process of the temperature below  $T_g$  before reaching the first peak of  $g(r)$  is relatively abrupt because of the more strong pair interactions between nanoplatelets and polymer segments. Contrastively, the shape of  $g(r)$  above  $T_g$  shows a good agreement in the position and height of the first peak, but it appears slightly flat when the  $r$  is beyond the first neighbor distance. Since the height and position of the peak in pair

correlation function is the result of a delicate balance between the nanoplatelets and polymer chains contributions to polymer failure. As the interactions are increased, the bonds between nanoplatelets and polymer chains are more tightness. Thereby, the growth of cavities becomes more difficult, and formation of the temporary bonds between the nanoplatelets and polymer chains will cost much more energy. Therefore, as a result, the property of the material will be better while the interactions are increased.

From Figure 4.21 and 4.22, it can be seen that the system at above  $T_g$  always shows a larger amount of the nanoplatelet present in the bridge region during the simulation, than at below  $T_g$ , as shown in the former simulation, because the nanoplatelets have enough mobility from the more strong interactions to form the temporary bonds even the local region at above  $T_g$  and the temporary bonds and local region can dissipate energy superfluity. But the mobility of nanoplatelets will be reduced at below  $T_g$ .

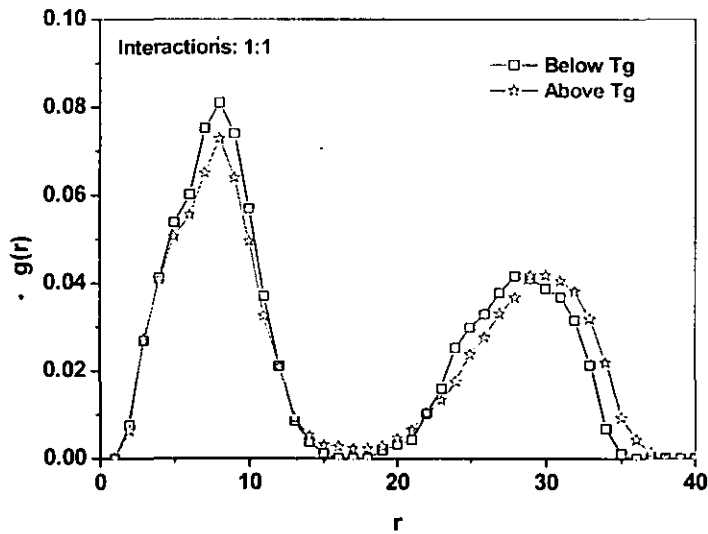


**Figure 4.21** Nanoplatelet – nanoplatelet correlation function,  $g(r)$  with interaction strength with 3wt.% nanoplatelets .

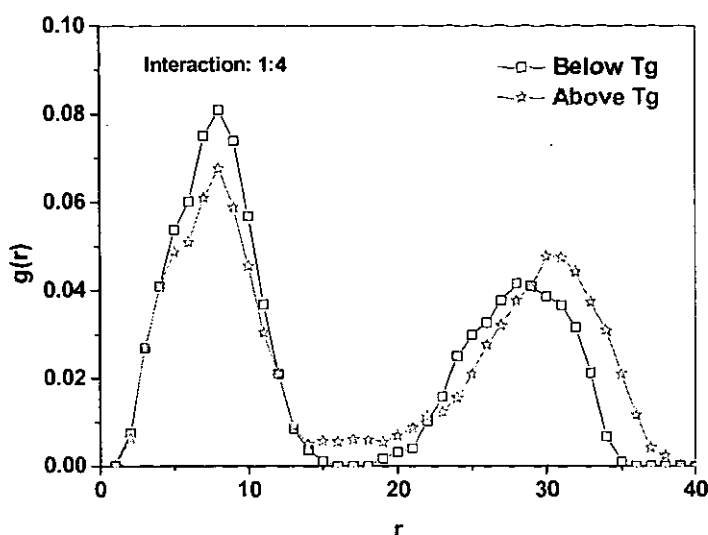


**Figure 4.22** Nanoplatelet – nanoplatelet correlation function,  $g(r)$  with the interaction strength with 3wt.% nanoplatelets.

It is clear that the mobility of the nanoplatelet is determined by both its size and the interaction strength with the polymer chains. But in our simulation the size of the nanoplatelet was fixed at 0.6 times of the gyration radius of the polymer chain. Therefore, the mobility of a nanoplate was only determined by the interactions between nanoplatelets and polymer chains. As the interaction strength is increased, the mobility of nanoplatelets will also be enhanced. It will more easily to create the temporary cross links and local region. The enhancement of the strength and the growth of the cavity retardation are more evident.

#### 4.2.4 Effect of relaxation time on fracture

Relaxation time is a general concept in physics for the characteristic time in which a system relaxes under certain changes in external conditions. In particular it measures the time-dependent response of a system to well-defined external stimuli. It is clear that the relaxation time of the nanoplatelet is different from that of a polymer. However, it is not clear whether there is the effect of the difference between the

relaxation time of the nanoplatelet and that of polymer chain on the fracture strength. Epoxy-organoclay, nylon-organoclay and polyurethane-organoclay nanocomposites have been investigated for more than 10 years [1]. The addition of organoclay always enhances the mechanical properties of polyurethane [7, 14], and also can improve the mechanical properties for nylons. However, the addition of organoclay does not result in the enhancement of the toughness of epoxy resins [12]. In order to understand these results, it is necessary to know whether and how the difference between the relaxation time of the nanoplatelet and that of polymer chain affects the fracture behaviour of the polymer. We believe that this investigation could provide some information for the design of polymer-organoclay nanocomposites with improved mechanical properties especially toughness.

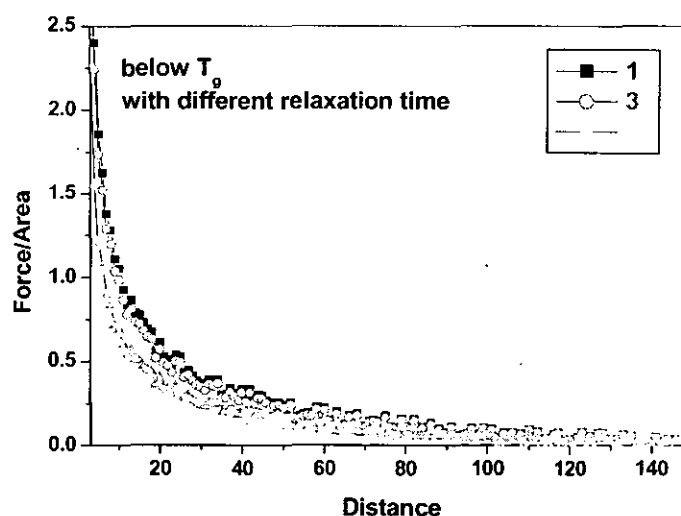


**Figure 4.23** The force/area curves vs. distance with different relaxation times at 1.1  $T_g$ .

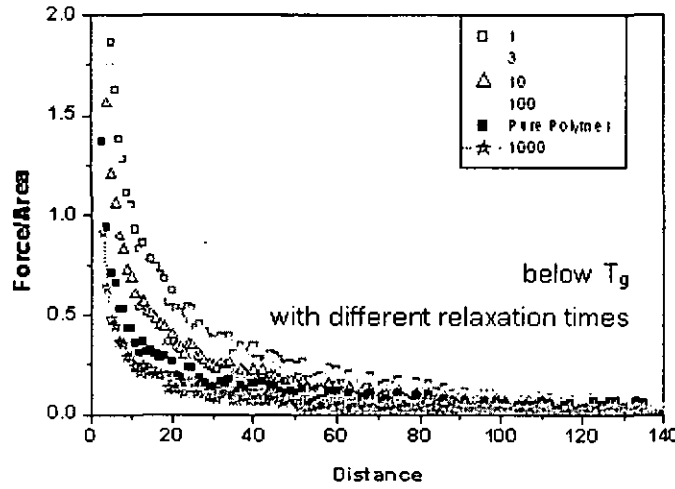


**Figure 4.24** The force/area curves vs. distance with different relaxation times at  $0.4T_g$ .

Figures 4.23 and 4.24 show force/area curves vs. distance as a function of the difference relaxation times at  $1.1 T_g$ , where  $\sigma_f = 3\sigma$ ,  $\varepsilon_{fp} = 4\varepsilon$ ,  $\nu = 0.03\sigma/\tau$  and 3Wt.% of nanoplatelets. The difference was defined as  $\tau_{\text{polymer}}/\tau_{\text{nanoplatelet}}=1,2,3$ , and  $n$ . It can be seen that when the polymer is at above its  $T_g$ , the effect of the difference between the relaxation times on the fracture strength of polymers is ignorable. For comparison, the force/area curve vs. distance for the pure polymer was also provided. It can be seen that when the polymer is at below its  $T_g$ , the effect of the difference of the relaxation times on the fracture strength of the polymer is significant. With increasing the difference, the strength of the curve decreases, i.e.  $W^*$  decreases. When the difference is big enough, the polymer will turn from tough to brittle.

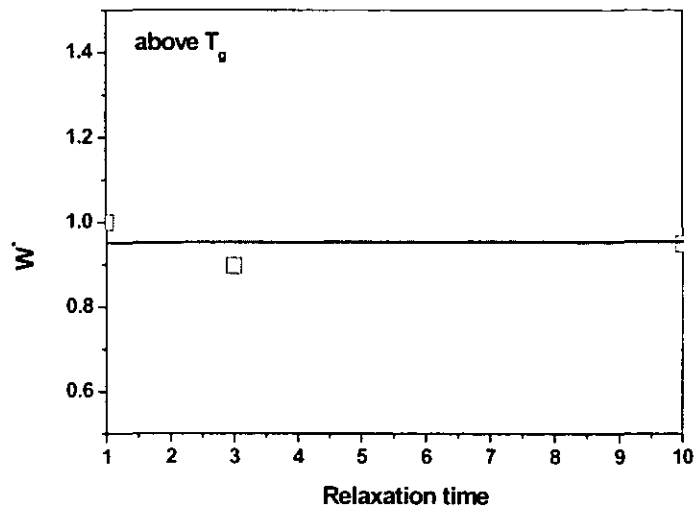


**Figure 4.25** Normalized work,  $W^*$ , to failure with relaxation time at  $1.1 T_g$  with 3wt.% nanoplatelets.

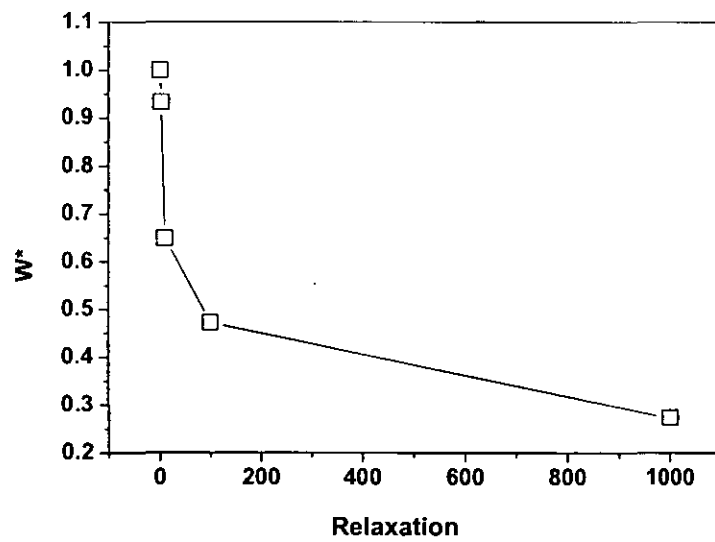


**Figure 4.26** Normalized work,  $W^*$ , to failure with relaxation time at  $0.4 T_g$  with 3wt.% nanoplatelets.

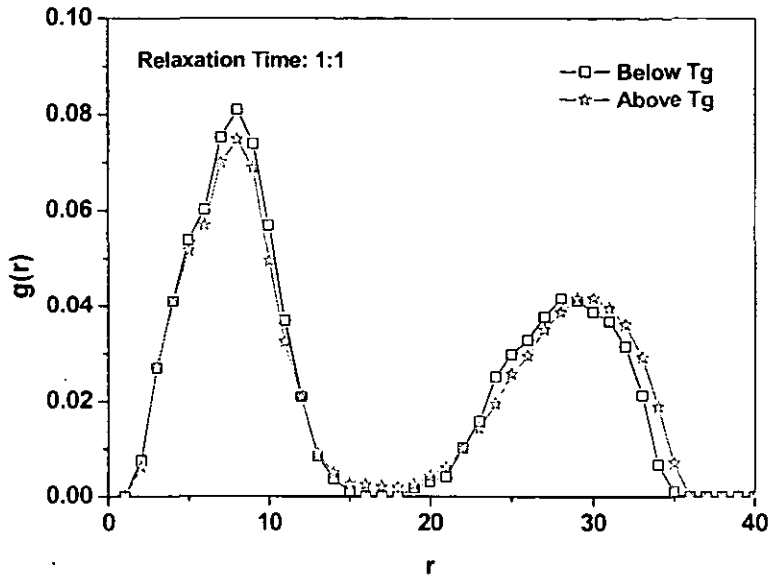


**Figure 4.27** Nanoplatelet – nanoplatelet correlation function,  $g(r)$  with relaxation time with 3wt.% nanoplatelets.

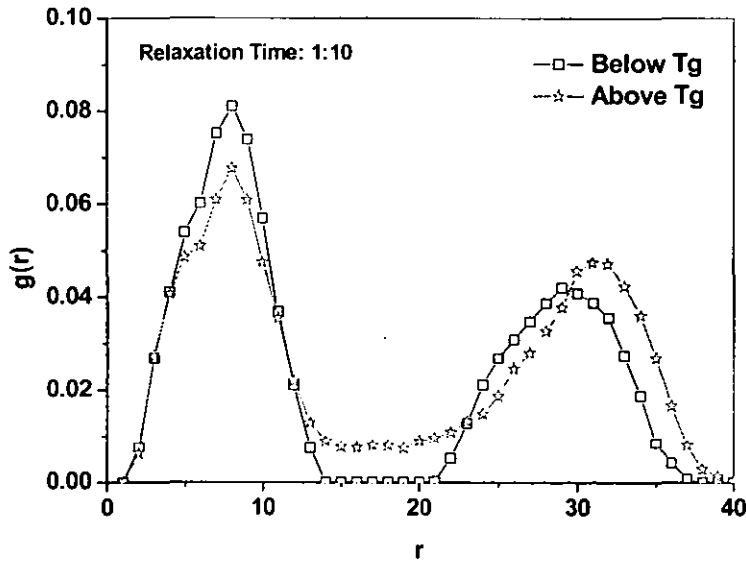


**Figure 4.28** Nanoplatelet – nanoplatelet correlation function,  $g(r)$  with relaxation time with 3wt.% nanoplatelets.



Figures 4.25. and 4.26. show the effect of relaxation time of the polymer on the failure work. The effect on normalized work to failure,  $W^*$ , was very little while testing temperature was above  $T_g$ ; but it was significant while testing temperature was below  $T_g$ . This indicates that when testing temperature is above  $T_g$ , the additional energy can be dissipated by the motion of nanoplatelets for any relaxation time system. When testing temperature is below  $T_g$ , the nanoplatelet energy dissipation reduces.

Figures 4.27, 4.14 and 4.28 shows the nanoplatelet – nanoplatelet correlation function with various relaxation times ratio, 1:1, 1:3 and 1:10. From Figures 4.27 and 4.28, the first peak of  $g(r)$  at above  $T_g$  is nearly the same with that below  $T_g$ , when the relaxation times ratio is 1:1. The position and height of the first peak of  $g(r)$  are very close for both above and below  $T_g$ . As the relaxation time ratio increases from 3 to 10, the first peak of  $g(r)$  above  $T_g$  became narrower and lower than that below  $T_g$ . The second peak of  $g(r)$  above  $T_g$ , is shifted to the right obviously compared with that below  $T_g$ . The height of second peak below  $T_g$  with increasing the relaxation times ratio from 1 to 10 changed significantly, which seems very sensitive to the relaxation times ratio.

The increase in the difference between the relaxation times will result in a significant decrease of the mobility of the nanoplatelets when the polymer nanocomposite is tested at below its  $T_g$ . The results imply that the addition of nanofillers could make the toughness of the polymer worse tested at below its  $T_g$ . A typical example is epoxy-organoclay nanocomposites [12].

When testing temperature is above  $T_g$ , of the polymer the internal friction of polymer nanocomposite could be limit while the polymer chains move. Therefore stress could be relaxed rapidly. If testing temperature is too low, too far away from  $T_g$ , due to the huge internal friction, the mobility of polymer chains is very low, Therefore the stress

relaxation of polymer chains would be very slow.

Because the relaxation time of the nanoplatelets was very short, the process of relaxation will complete in instant. When testing temperature is above  $T_g$ , the relaxation time of polymer is also short. When the polymer in the nanocomposite starts to be deformed by loading, the deformation process of the nanoplatelets and polymer could be almost completed at the same time. Therefore the different relaxation times between the nanoplatelets and polymer chains almost have no significant effect on the fracture in polymer nanocomposite.

Series research results [1,7, 10, 14] indicate that the addition of clay into these polymers, which  $T_g$ s is lower than room temperature or nearby (or equal to) room temperature has significant enhancement on the mechanical properties. Tensile properties and fatigue durability of polyurethane, which  $T_g$  is about  $-40^{\circ}\text{C}$ , were intensively enhanced by the incorporation of organoclay [14]. The tensile strength and strain at break for these polyurethane nanocomposites increased more than 150%. The fatigue durability was significantly improved more than 6 times. For poly(styrene-co-butadiene) (SBR) and butadiene (BR) rubbers [10], which  $T_g$ s are much lower than room temperature, the tensile strength, elongation and fatigue durability of SBR and BR were also improved significantly with the addition of organoclay. The toughness of nylon6 was improved by the addition of clay [9], which  $T_g$  is nearby room temperature. However, the addition of clay did not toughen epoxy resins [12]. Recently, a toughed epoxy-organoclay nanocomposite has been developed [13]. Hexahydrophthalic acid anhydride-cured bisphenol A diglycidyl ether was used as matrix material for hybrid nanocomposites containing compatibilized polyether liquid rubbers. In this case, epoxy toughness was enhanced. It is believed that the compatibilized polyether liquid rubbers represent the key to toughening. The compatibilized polyether liquid rubbers could form a stress relaxation interface between epoxy matrix and organoclay.

Overall, for these polymers, which Tgs are lower than room temperature, such as polyurethane, or nearby (or equal to) room temperature, such as nylon, the nanoplatelets can always enhance the mechanical properties. However, for these polymers, which Tgs are higher than room temperature, such as epoxy and polystyrene, the addition of the nanoplatelets does not work well for the improvement of toughness. If one wants the nanoplatelets to be working for toughening these polymers, it is necessary to build up a stress relaxation interface between the polymer matrix and the nanoplatelet, such as the modification of the surfaces of nanofillers using coupling agents [13,18,19], in order to reduce the effect of the difference between the relaxation time of the polymer and that of the nanoplatelet.

## REFERENCE

1. S.S. Ray, M. Okamoto, *Progress in Polymer Science*, , **28**, 1539, (2003).
2. P.C. LeBaron, Z.Wang, T.J.Pinnavaia, *Appl Clay Sci.* , **15**, 11, (1999).
3. M.C.Koo, M.J.Kim, M.H.Choi, S.O. Kim, I.J.Chung, *J Appl Polym Sci*, **88**, 1526, (2003).
4. B.Liao, M.Song, H.Liang, Y.X.Pang, *Polymer*, **42**, 10007, (2001).
5. B. Hoffmann, C.Dietricha, R.Thomann, C.Friedrich, R.Mu"lhaupt, *Macromol. Rapid Commun.* , **21**, 57, (2000).
6. H.Haiyan, P.Mingwang, L.Xiucuo, S.Xudong, Z.Liucheng , *Polymer International*, **53**, 225, (2004).
7. K.J.Yao, M.Song, D.J.Hourston, D.Z.Luo, *Polymer*, **43**, 1017, (2002).
8. J.H.Park, S.C.Jana, *Macromolecules*, **36**, 2758, (2003).
9. T.D.Fornes, P.J.Yoon, H.Keshkula, D.R.Paul, *Polymer*, **42**, 9929, (2001).
10. M.Song, C.W.Wong, J.Jin, M.A.Ansarif, Z.Y.Zhang, M.Richardson, *Polymer International* , **54**,560, (2005).
11. A.Pegoretti, J.Kolarik, C.Peroni, C.Migliaresi, *Polymer*, **45**, 2751, (2004).

12. Y.Wang, S.Y.Shen, G.S.Gai, C.S.Fu , *Composite Materials III. Key Engineering Materials*, **249**, 413, (2003).
13. J. Fröhlich, R. Thomann, R. Mülhaupt, *Macromolecules*, **36**, 7205, (2003).
14. M.Song, D.J.Hourston, K.J.Yao, J.K.H.Tay, M.A.Ansarif, *J.Appl.Polm.Sci*, **90**,3239, (2003).
15. H.H. Kausch, *Polymer fracture*, **Springer**, (1987).
16. Song M, Pang YX, *Journal of Macromolecular Science - Physics*, **B40**, 1151, (2001).
17. Aleksandar D, Salvatore T, and Frank H. S, *PHYSICAL REVIEW E* **71**, 011105, (2005).
18. K.Wang, L.Chen, J.S.Wu, M.Toh, C.B.He, A.F.Yee, *Macromolecules* ,38,799, (2005).
19. Z.Z.Yu, C.Yan, M.S.Yang , Y.W.Mai , *Polymer International*, **53**, 1093, (2004).

## **CHAPTER 5**

# **ENERGY DISSIPATION AND ENHANCEMENT OF FATIGUE DURABILITY OF POLYMER NANOCOMPOSITES**

### **5.1 INTRODUCTION**

High-molecular polymers, including their composites, exhibit viscoelastic properties. This means that they can be considered in certain conditions as a very thick non-Newtonian fluid, which is characterised among other things by viscosity, i.e. internal friction. When a polymer is being deformed, some motion of the molecular chains or their parts occur, which has associated with it a jump over a potential energy barrier [1, 2]. This results in the dissipation of a part of the strain energy, termed internal friction (damping). Investigations carried out for elastomers (rubber) [1, 3] have proved that during a cyclic deformation heating up takes place. The amount of energy dissipated in the form of heat depends primarily on the frequency and the amplitude of the strains as well as on the value of the loss modulus, which describes the internal friction in those materials. During sliding cyclic deformation of the materials occurs. This is mainly due to deviations of the contact surface shape, tolerance of machining (waviness, roughness, run out of the rotating element) as well as from the oscillatory character of the friction forces itself [4- 6].

In recent years, polyurethane nanocomposites have been investigated [7- 12]. One of the aims is to develop damping materials with improved fatigue durability [7, 13]. Fatigue is very general phenomenon in most materials and refers to the changes in properties resulting from the applied cyclic loads [14]. The failure mechanism of polymers must include breaking of bonds, a phenomenon depending on the polymer structure. Time-and frequency-dependent viscoelastic deformation can be also involved [14]. The mechanisms controlling the total fatigue life of polymers vary with

many morphological, thermal, mechanical and environmental factors [14-16].

Polyurethane elastomer (PU) is one of the most versatile materials today due to their biocompatibility [17, 18], elasticity [17], and abrasion resistance [17, 18]. PU generally consists of the two phases, which determined its physical properties. The hard-segment phase is made up of hydrogen-bonded stiff segments that are formed by a reaction of diisocyanate with chain extender. The extent of hard segments primarily determines the modulus of PUE. The flexible soft-segment phase, which is composed of polyether or polyester diol, predominately influences the elastic nature of PUE. One of important applications of PUE is as damping materials, such as the spring aids used in cars, which need to have excellent cyclic fatigue and tensile properties. In order to meet the demand for high performance damping material, which is rapidly and continuously growing in a variety of aerospace and civil systems, PUE/organoclay nanocomposites have been recently produced and studied in our laboratory. It has been found that introduction of small amount organoclay tensile strength increased by 120% and elongation at break increased by 100%, and its cyclic fatigue durability increased significantly compared to pure PUE [7, 13].

The nanocomposites offer attractive potential for diversification and application of traditional polymers. The many useful properties of polymers such as mechanical properties, thermal stability and barrier properties can be built by incorporation of only small amount of nano-sized organoclay into polymer hosts [13, 19- 22]. Compared with pure polymer or conventional composites, the nanocomposites have higher modulus [19- 21], greater strength [22], longer fatigue durability [8], higher heat resistance [19, 22] and lower gas permeability [23], better flame retardancy [24, 25] and etc. However, in fact, incorporation of fillers usually results in worsening cyclic fatigue property and reducing the elongation at break [18]. In understanding the questions of why and how the small amount of organoclay can improve physical properties of polymers a large number of the studies have been conducted [19]. The main reasons for these improvements are the stronger interfacial interactions between

the matrix and nanolayers, and size of the filler compared with conventional filler-reinforced systems [19]. However, the details of information concerning how and why the incorporation of organoclay can improve the fatigue durability of some polymers is still not clear yet. Therefore, the research into the deformation and fracture of polymer nanocomposites by fatigue is significantly important for their certain applications. However, from experiments, it is very difficult or nearly impossible to investigate the influence of the interactions between polymers and nanofillers, the nanofillers orientations internal the nanocomposites and nanofiller geometry to the energy dissipations of polymer matrix, due to the interactions between polymers and nanofillers cannot be set to a value you want in experiments, such as  $N$  times of interactions between polymers,  $N=1, 2, 3, \dots$ . The nanofiller orientations cannot be set to an angle you want to investigate, such as 0 degree, 90 degree, etc. limitation complexions. Also, the effect of nanofiller geometries cannot be investigated individually without other influences together. In order to solve above problems, the computer MD simulation is introduced. The computer MD simulations can implement the studies which experiments cannot. The major objective in this chapter is: investigate the influence of nanofillers to polymer fatigue durability and energy dissipations by using computer MD simulations. And validate the MD simulation results by comparison with experiments.

## **5.2 SIMULATION, AND EXPERIMENTS FOR COMPARISON**

### **5.2.1 Simulation**

#### **5.2.1.1 Model**

The polymer chain can be described in this simulation with a Bead-Spring Model [26- 28] which has been introduced in chapter 4. In the bead-spring model, the monomers are considered as hard spherical beads. The polymer chain is the hard beads connecting with unearthy spring. Each polymer chain has 64 monomer beads. Each bead has mass  $m$ . The interactions between any two beads observe a truncated 6-12 Lennard-Jones potential [27]. The potential is zero, if the distance between two

beads is equal or bigger than a cut-off radius. The characteristic time for a polymer chain is  $\tau_{LJ} \equiv (m\sigma^2/\epsilon)^{1/2}$ . Layered silicate is considered as a hard square flat panel without thickness.

The length of the nanoplatelet is 0.6 times the radius of gyration of the polymer chains. In the simulation, it is set that the density of the nanoplatelet is  $\rho_f = 3\rho$ , where  $\rho$  is the density of monomer. The interactions between the polymer chains and the nanoplatelets are mediated by a revised 6-12 Lennard-Jones potential. The details of the models are shown in chapter 4.

#### 5.2.1.2 Simulation

The total elements in the simulation system were 4096 (nanoplatelets + segments). Periodic boundary conditions were applied in x-axis and y-axis directions, while the z direction was bounded by walls. At the initial stage, the system was equilibrated, i.e., energy of the system is minimized and the nanoplatelets were uniformly distributed in the polymer matrix. The speed of the stretching along z-axis was  $v = 0.03 \sigma/\tau$ .  $\tau$  is the characteristic time, which is defined as  $\tau = \tau_{LJ} \equiv (m\sigma^2/\epsilon)^{1/2}$ . It was assumed that the failure never occurs at the interface between walls and the polymer matrix. For simulation,  $0.005\tau$  was used as time step. The FENE potential was used between the nearest neighbouring beads in a same polymer chain in order to keep all polymer chains did not cross each other.

The simulations were performed up to a maximum deflection of 50%, 100%, and 200% respectively. The stress on each simulation system was returned to zero at the end of each cycle. The simulation used in this chapter is NVT system. The temperature of the simulation is chosen in front and it is a constant during the whole simulation. In the experiments, the total volume of the sample was constant, even as it was put through 50, 100 and 200% deformations. This volume constant of sample in experiments was incarnate by the necking of sample during the experiments. The



necking of simulation area in simulation is actualized by the periodic boundary conditions. The total volume of the simulation area was also kept a constant by the periodic boundary condition in x direction and y direction even the vacuums are continued introduced into simulation area from z direction (shown in Figure 5.2.1.). The periodic boundary condition just like which the simulation was running on the surface of a cylinder. The elements of simulation disappear in an edge of the simulation area then appear on the other side of the simulation area.

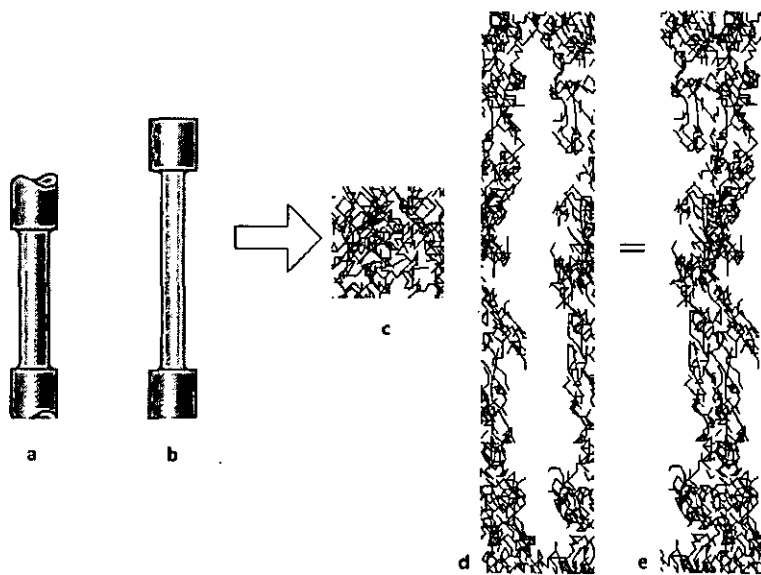


**Figure 5.1** Schematic map of the necking in experiments and how simulation area actualize necking during the simulation by the periodic boundary condition. a. experiment sample, b. necking in experiment after tension, c. snapshot of original simulation area, d. snapshot of simulation area after simulation, e. how to understand the necking of the simulation area during the simulation by the periodic boundary condition.

## 5.2.2. EXPERIMENTAL

### 5.2.2.1. Materials

Some mechanical properties have been tested in order to compare with the simulation results by using PU nanocomposites. The materials used to prepare PU nanocomposites are introduced in this paragraph.

### Isocyanate

Two types of isocyanate were used for preparation of polyurethane samples. One is HMDI, another is prepolymer MDI. The details are shown in Table 5.1.

**Table 5.1** Details of 4, 4 - methylenebis (cyclohexyl isocyanate).

4, 4 -methylenebis(cyclohexyl isocyanate)	
Commercial name:	HMDI or hydrogenated MDI
Molecular formula:	OCN-C <sub>6</sub> H <sub>10</sub> -CH <sub>2</sub> -C <sub>6</sub> H <sub>10</sub> -NCO
Molecular weight:	262
Equivalent weight:	262/2=131
Appearance:	colorless liquid
Density (at 20°C):	1.066
Fleshing point:	>110 °C

The hypostasis of the relative reactivity of two HMDI isocyanate groups is same (shown in Table 5.2.). The structure of HMDI contrast to other isocyanates, such as IPDI, even the first isocyanate group of IPDI reacts more rapidly than those of HMDI. But the second group reacts more slowly. Then, IPDI may not react any faster than HMDI [29]. In order to shorten the reaction time or reduce the reaction temperature, catalysts are always used. Organic tin compounds are generally very effective catalysts.

**Table 5.2.** Reactivity of HMDI relative to IDI, MDI. HDI and IPDI.

	Relative rate constant	K1	K2
TDI	Toluene diisocyanate	400	33
MDI	4,4 -Diphenylmethane diisocyanate	320	110
HDI	2,6-Hexamethylene diisocyanate	1	0.50

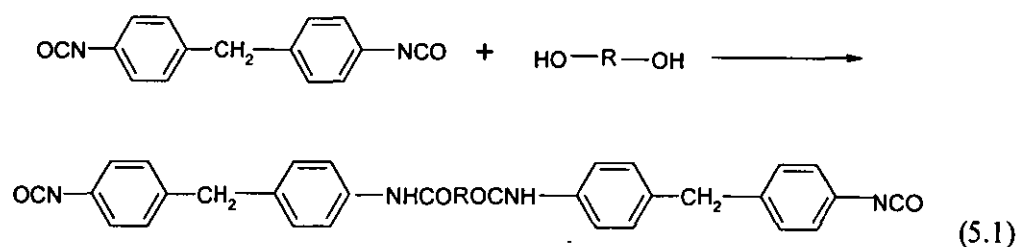
HMDI	4,4 -Dicyclohexylmethane diisocyanate	0.57	0.40
IPDI	3-Isocyanatomethyl-3,5,5-trimethylcyclohexyl isocyanate	0.62	0.23

The particular prepolymer used in this chapter was the addition product of modified MDI, to the prepolymer intermediate; the dihydric glycol must be linear and reacted with the MDI [30], which is commercially produced by Hyperlast Ltd (UK). The details are shown in Table 5.3.

**Table 5.3.** Details of modified MDI

Modified MDI	
Appearance:	Colourless Liquid at 25 °C
NCO content (%):	23 %
Viscosity:	120-180 cpa at 25 °C
Specific gravity:	1.21-1.23 at 25 °C

The MDI is much more environment friendly, and has lower toxicity than toluene diisocyanate (TDI) and many other diisocyanate (shown in following equation).



### ***Polyols***

Polyol is an organic compound having more than one hydroxyl (-OH) group per molecule [29]. In the polyurethane industry, the term includes polymeric compounds containing alcoholic hydroxyl groups such as polyethers, and polyesters, used as reactants in polyurethane. In this experiment, the polyether polyol was chosen as soft

segment, which details are as follows (details shown in Table 5.4). It was supplied by Elastogran (UK).

**Table 5.4.** Details of polyether polyol

Commercial name :	Lupranol 2090
Appearance:	Colorless liquid
Molecules weight:	6000
OHV:	28 mgKOH/g
Viscosity (at 25°C):	1125mpa.s
Function:	3
Structure:	$\begin{array}{c} \text{CH}_2\text{--}[\text{O--CH}_2\text{--CH}(\text{CH}_3)]_m\text{--CH}_2\text{CH}_2\text{--OH} \\   \\ \text{CH}_2\text{--}[\text{O--CH}_2\text{--CH}(\text{CH}_3)]_n\text{--CH}_2\text{CH}_2\text{--OH} \\   \\ \text{CH}_2\text{--}[\text{O--CH}_2\text{--CH}(\text{CH}_3)]_l\text{--CH}_2\text{CH}_2\text{--OH} \end{array}$

### Chain Extender

Some low molecular weight reactants are named as chain extenders [30].

1,4-Butanediol is a very important chain extender. 1,4-Butanediol was supplied by Aldrich company, which details are as follows.

**Table 5.5.** Details of 1,4-Butanediol

Trade name:	1, 4-butanediol
Appearance:	Colorless liquid
Structure:	HO-(CH <sub>2</sub> ) <sub>4</sub> -OH
Molecular weight:	90
Equivalent weight:	90/2 = 45
Melt point:	16°C
Flesh point:	230°C
Density:	1.017 g/cm <sup>3</sup>

### Catalysts

Catalyst is a substance that causes or accelerates a chemical reaction when added to the reactants in a minor amount, and that is not consumed in the reaction[30]. There are two catalysts used in these formulations. One is DABCO-33LV supplied by Air Products and Chemicals, Inc. DABCO-33LV is a mixture of Triethylenediamine and di(propylene glycol). Another is stannous 2-ethylhexanoate supplied by the Sigma Chemical Company.

### Organoclay

There are two types of clays used in the experiments: Cloisite 30B and Cloisite20A. Cloisite 20A is a natural montmorillonite modified with a quaternary ammonium salt, which details are as follows.

**Table 5.6.** Details of Cloisite 20A

Commercial name:	Cloisite 20A
Organic modifier:	methyl, tallow, bis- 2- hydroxyethyl, quaternary ammonium
Modifier Concentration:	95meq/100g
Moisture:	< 2%
Density:	1.98g/cm <sup>3</sup>
Colour:	off white
X-Ray result:	d <sub>001</sub> =24.2Å
Structure:	$  \begin{array}{c}  \text{CH}_3 \\    \\  \text{CH}_3 - \text{N}^+ - \text{HT} \\    \\  \text{HT}  \end{array}  $

Where HT is Hydrogenated Tallow (~65% C18; ~30% C16; ~5% C14)

Cloisite 30B is a natural montmorillonite modified with a quaternary ammonium salt, which details are as follows.

**Table 5.7.** Details of Cloisite 30B

Commercial name:	Cloisite 30B
Organic modifier:	Dimethyl, dihydrogenated tallow, quaternary ammonium chloride
Modifier Concentration:	95meq/100g
Moisture:	< 2%
Density:	1.77g/cm <sup>3</sup>
Colour:	off white
X-Ray result:	d <sub>001</sub> =18.5Å
Structure:	$  \begin{array}{c}  \text{CH}_2\text{CH}_2\text{OH} \\    \\  \text{CH}_3 - \text{N}^+ - \text{T} \\    \\  \text{CH}_2\text{CH}_2\text{OH}  \end{array}  $

Where T is Tallow (~65% C18; ~30% C16; ~5% C14)

#### 5.2.2.2. Sample Preparation

- 1) Polyether polyol 2090 was mixed with organoclay and stirred for 24h at 60°C, the organoclay concentration was 0%, 1%, 3% and 5%. Then the mixtures were degassed under vacuum for 20min.
- 2) The mixture was mixed with 1, 4-butanediol of Dabco-33LV, stannous 2-ethyl hexanoate and 4, 4'-methylene bis(cyclohexyl isocyanate) at room temperature for 1min and was vacuum degassed for 3min.
- 3) Then the viscous prepolymer was poured into an O-ring metal mould and cured at 50°C for 24h to obtain a 2mm-thick sheet.
- 4) Finally, the sample was post-cured for a week at 80°C.

#### 5.2.2.3. Hysteresis Test

Hysteresis tests were performed using a Hounsfield testing machine at room temperature. In the hysteresis mode, the specimens were stretched to 50%, 100% or

200% strain at a crosshead rate of 50mm/min and then allowed to retract at the same rate to the unstretched state. The hysteresis, defined as the amount of dissipated energy during cyclic loading, was determined from the area enclosed by the hysteresis loop. For any given cycle (n), the dissipation energy is calculated by

$$\Delta E(n) = \oint \sigma d\varepsilon \quad (5.2)$$

Where  $\Delta E$  is dissipated energy,  $\sigma$  is stress,  $\varepsilon$  is strain. Permanent set taken as the strain at which a zero load is measured on the unloading cycle.

#### 5.2.2.4. *Cyclic Fatigue Test*

In a conventional fatigue test, the specimen was subjected to cyclic loading and number of cycles to failure was recorded. In this study the cyclic fatigue life of the PUE nanocomposites was measured in uniaxial tension in a Hampden dynamic testing machine (Northampton, UK), using dumb-bell test-pieces. The tests were performed at room temperature, at a constant maximum deflection of 100%, and a test frequency of 1.44Hz. Strain on each test-piece was relaxed to zero at the end of each cycle. All the reported results are the average of, at least, ten measurements.

#### 5.2.2.5. *Wide-Angle X-ray Diffraction (WAXD)*

Wide angle X-ray diffraction (WAXD) was used to measure the d-spacing of PUE/organoclay nanocomposites. X-ray diffraction experiments were performed on film samples on a Bruker X-ray diffractometer (AXS D8 Advance) using  $K_{\alpha}$  ( $\lambda = 0.54\text{nm}$ ) radiation. Samples were scanned at a rate  $0.24^{\circ}/\text{min}$  from ca.  $1$  to  $15^{\circ}$  in  $2\theta$ .

### 5.3 Energy dissipation in exfoliation polymer/ organoclay nanocomposites

### **5.3.1 Introduction**

The energy dissipation, or the friction phenomenon between two contacting parties which slide with respect to each other, is in general taken to denote the conversion of orderly translational energies into disorderly vibrational energies, such as the balls on the pool table. There are exactly two opposing forces which slow down the balls till they come to a complete rest. These are air resistance force, and the frictional force. But because the air resistance on such dense objects as pool balls is very small, we will disregard its effects. Thus friction is the major drag force to the balls and this force exist between the two surfaces which are in contact: one from the cloth of the table and the other from the balls. The friction causes the balls on the table that are sliding to slow down. This means that the kinetic energy of the balls decrease and eventually to zero when the balls come to rest. With zero external force on the pool table, the energy of the system must be conserved. Then, the kinetic energy has been dissipated through friction. In the nanocomposites, matters are held together by series of bonds that exist between molecules, between molecules and clays and between clays themselves. When the surface of an object comes in contact with another, there is a new attraction between the two surfaces and the overall effect of this is the frictional force, it can be a van der Waals' interaction, or a chemic bonding internal the composites or a hydrogenolysis. This force is a drag force and thus opposes the direction in which an object is moving.

### **5.3.2 Results and discussion**

Hysteresis test is a simple method for analysis of the nature of energy dissipation in a polymer, which is contributed to internal friction between polymer chains [32]. Polymer/ organoclay nanocomposites consist of nano-sized particles dispersed in a polymer matrix, which could influence viscoelastic nature and induce extra energy dissipation due to the existence of internal friction at interface between polymer chains and the surface of clay layers. Energy dissipation mechanism for polyurethane/ organoclay nanocomposites should include both internal friction between polymer chains and internal friction between polymer chains and the surface of nanolayers.



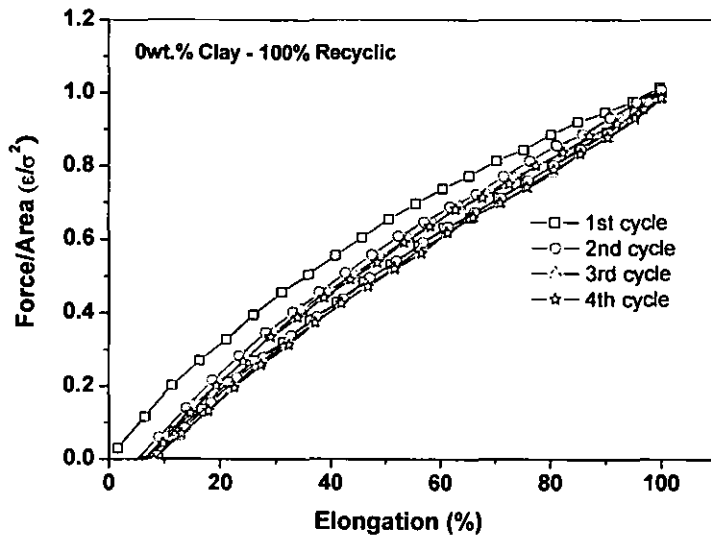


**Figure 5.2** Hysteresis curves for polymer nanocomposite with 0wt.% organoclay content, subjected to 100% strain

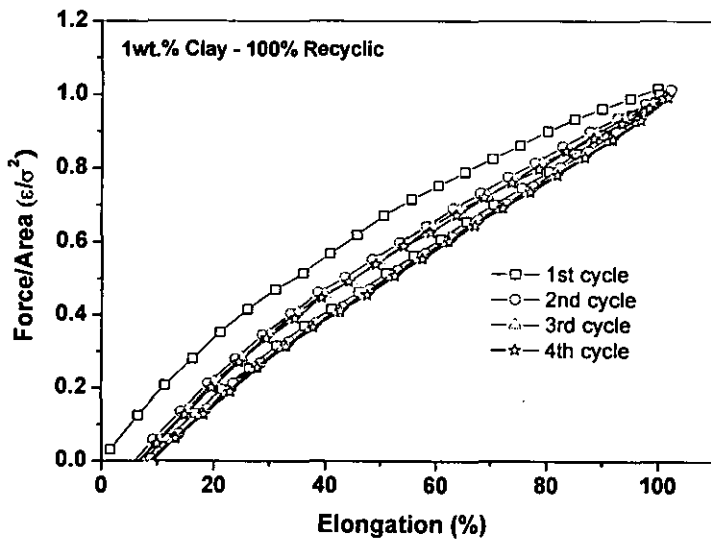


**Figure 5.3** Hysteresis curves for polymer nanocomposite with 1wt.% organoclay content, subjected to 100% strain

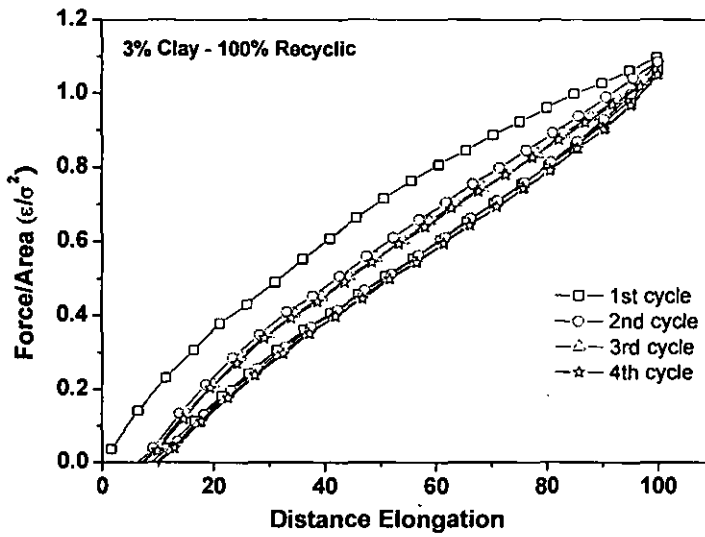


**Figure 5.4** Hysteresis curves for polymer nanocomposite with 3wt.% organoclay content, subjected to 100% strain

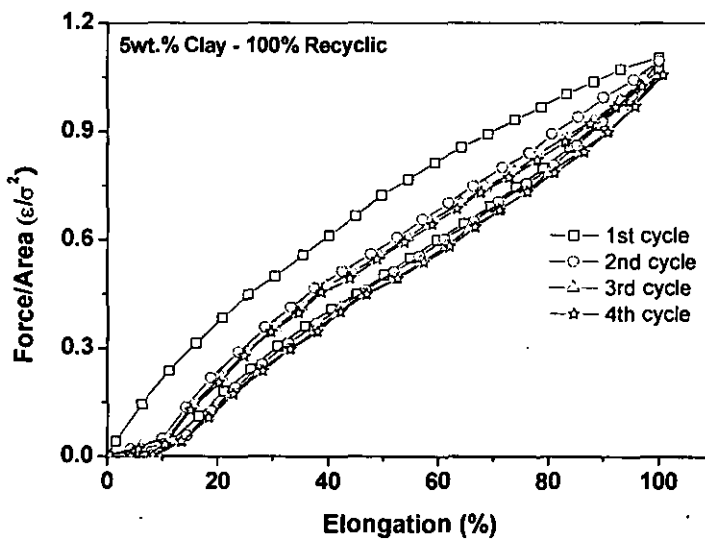


**Figure 5.5** Hysteresis curves for polymer nanocomposite with 5wt.% organoclay content, subjected to 100% strain

Figure 5.2 to Figure 5.5 show the typical hysteresis curves of PU nanocomposites with 0%, 1%, 3% and 5% organoclay by weight subjected to 100% strain for loading and unloading cycles 1, 2,

3 and 4, respectively. It can be found in Figure 5.1 to Figure 5.4 that the dissipated energy, which is the area enclosed by the cycle line, is increasing as the content of nanofillers is increasing.

The internal friction between polymer chains was not change in this 4 systems because the polymer matrix is the same in this 4 simulation systems. Because the energy dissipation of polymer/ organoclay nanocomposites are not only included internal friction between polymer chains but also included internal friction between polymer chains and the surface of nanolayers and the internal friction between nanolayers, therefore as the content of nanolayers increase, it is easy to understand the enhancement of the dissipated energy of polymer nanocomposite

Obviously, the dissipated energy in the 1<sup>st</sup> cycle is much greater than in following cycles was energy dissipation unchange observed after the additional cycles.

Permanent set is phenomenon characterized by the incomplete recovery of a material to its original length after being strained. It was noticed that the effect of nanofillers on permanent change of structure related to strain magnitude subjected to the materials. When the sample was stressed at lower strain of 50%, the addition of organoclay did not make any extra displacement (permanent set). By contrast, at strain of 100%, the addition of organoclay only resulted in a slight increase in displacement and at large strain of 200%, it was significantly increased, which means that the irreversible changes of microstructure took place resulting from the addition of organoclay (see following figures).

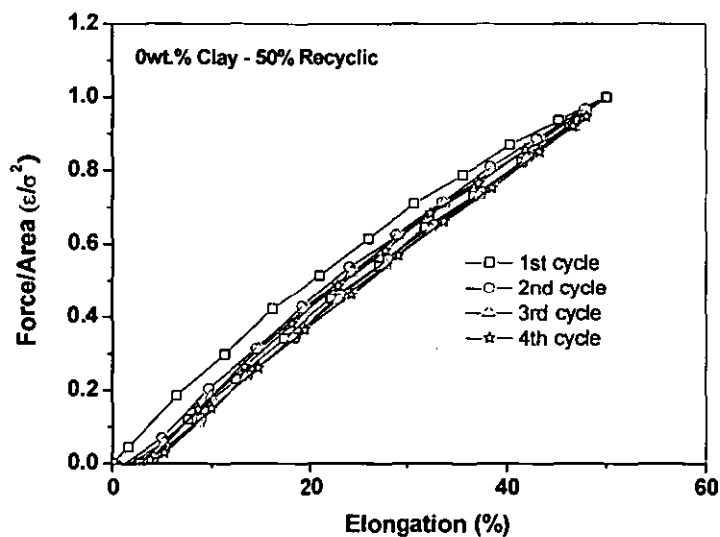


**Figure 5.6** Hysteresis curves for polymer nanocomposite with 0wt.% organoclay content, subjected to 50% strain

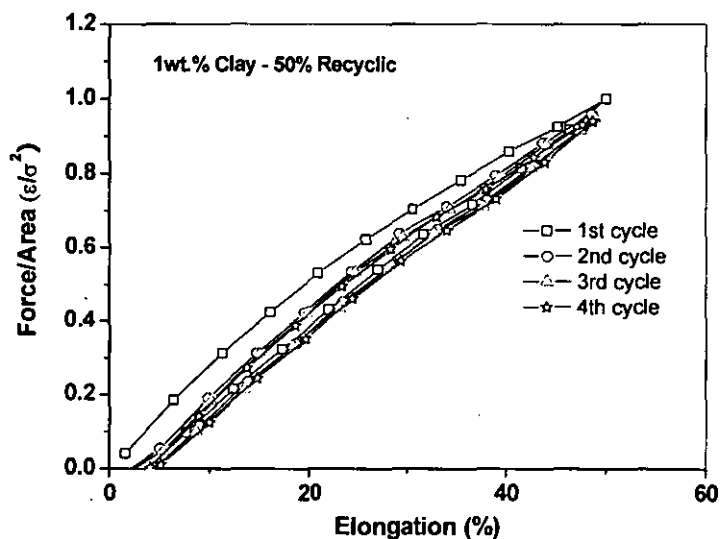


**Figure 5.7** Hysteresis curves for polymer nanocomposite with 1wt.% organoclay content, subjected to 50% strain

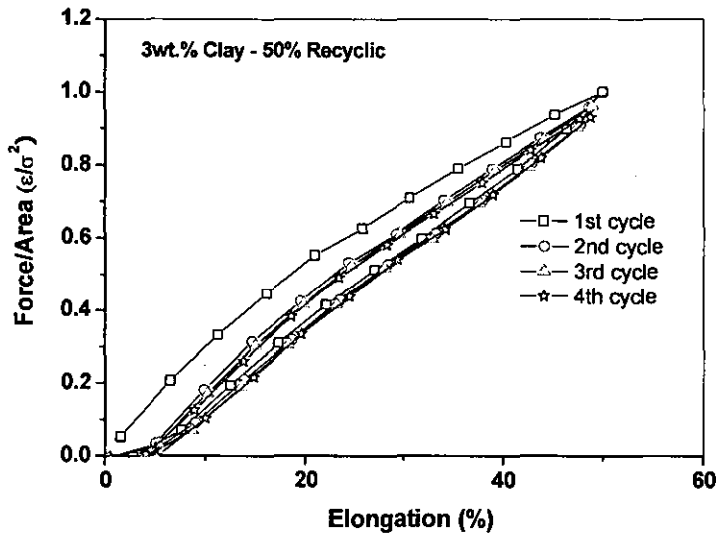


**Figure 5.8** Hysteresis curves for polymer nanocomposite with 3wt.% organoclay content, subjected to 50% strain

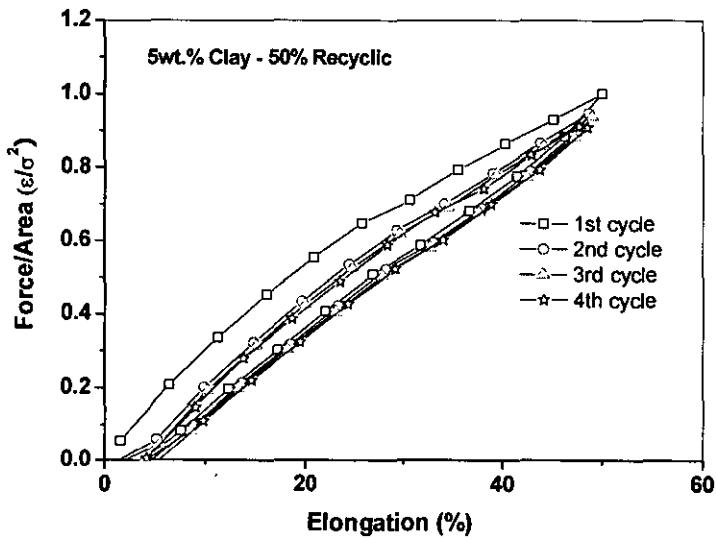


**Figure 5.9** Hysteresis curves for polymer nanocomposite with 5wt.% organoclay content, subjected to 50% strain

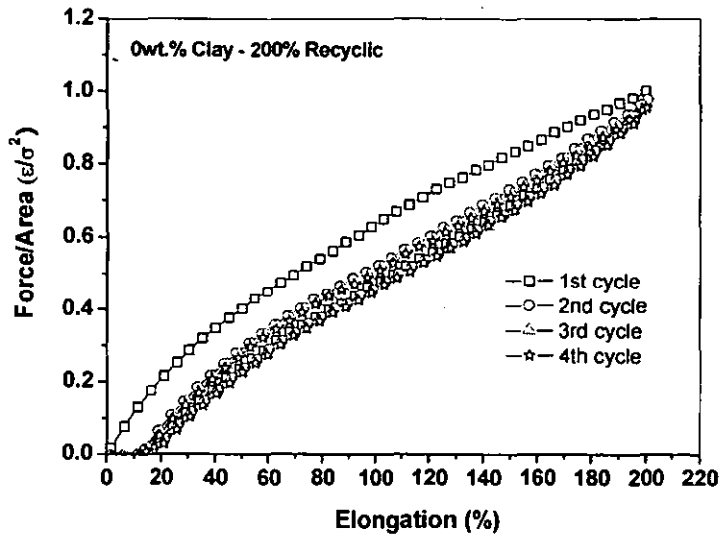


**Figure 5.10** Hysteresis curves for polymer nanocomposite with 0wt.% organoclay content, subjected to 200% strain

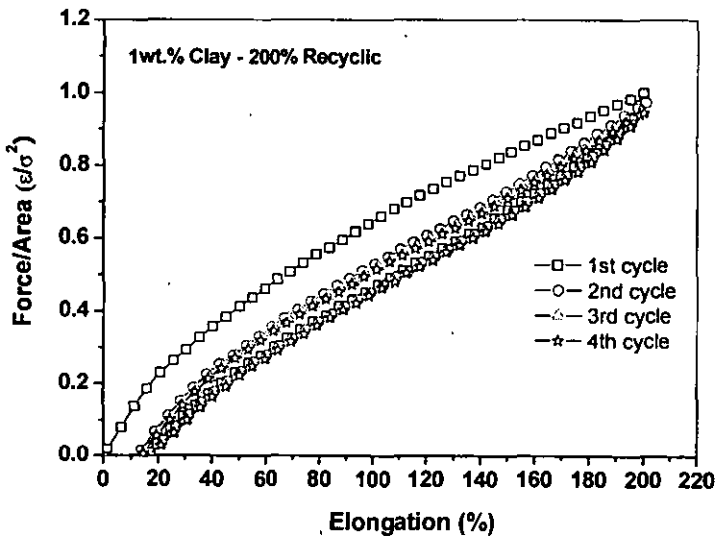


**Figure 5.11** Hysteresis curves for polymer nanocomposite with 1wt.% organoclay content, subjected to 200% strain

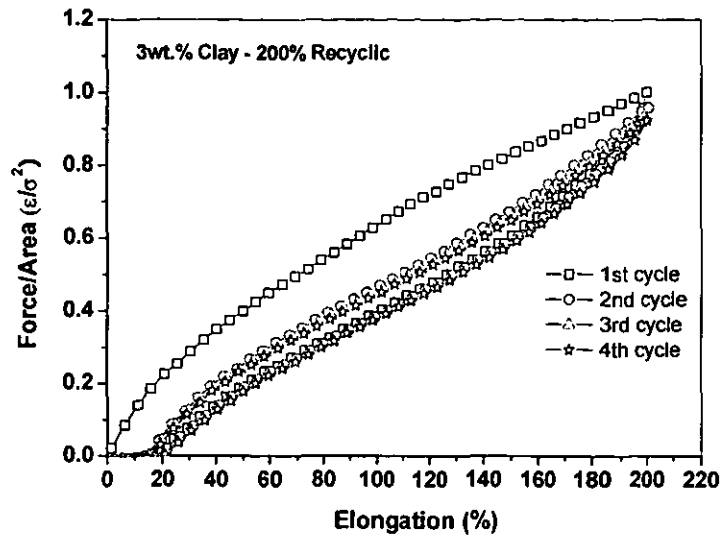


**Figure 5.12** Hysteresis curves for polymer nanocomposite with 3wt.% organoclay content, subjected to 200% strain

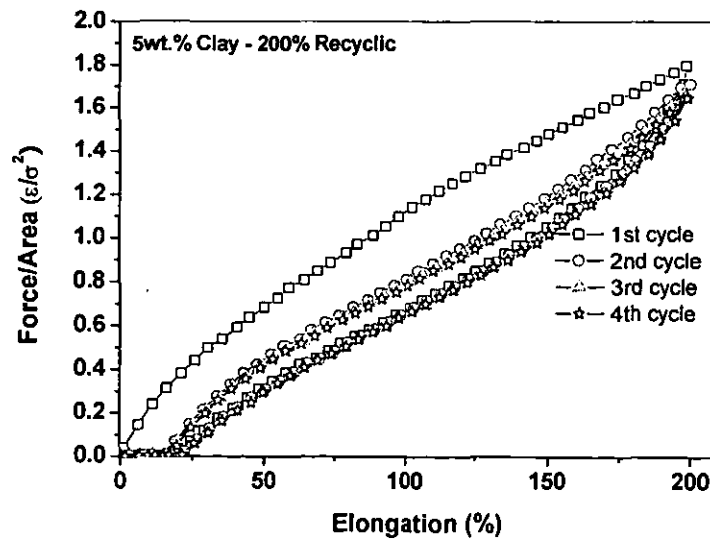


**Figure 5.13** Hysteresis curves for polymer nanocomposite with 5wt.% organoclay content, subjected to 200% strain

For a polymer/organoclay nanocomposite system, the deformation behaviour is related to both interconnecting polymer chains and nanoplatelets. It can be considered that the additional energy loss caused by the incorporation of organoclay may be contributed to frictional sliding at the interface between the surfaces of the organoclay layer and polymer molecules, and the orientation of nanoplatelets. Additionally, if the nanoplatelets are unable to return to their original positions when the force is removed this also in turn disrupts the polymer chains to relax. So the polymer nanocomposites show higher hysteresis and permanent set value than that of the pure polymer. As a consequence, the additional energy loss could come from two parts: the frictional sliding at the interface and the orientation of the nanoplatelets. From the permanent set it can be assumed that the orientation of the nanoplatelets in the nanocomposites exhibited reversible behaviour if the extension was 50%. So in this case the additional energy loss in the nanocomposites could be contributed to only the frictional sliding part.

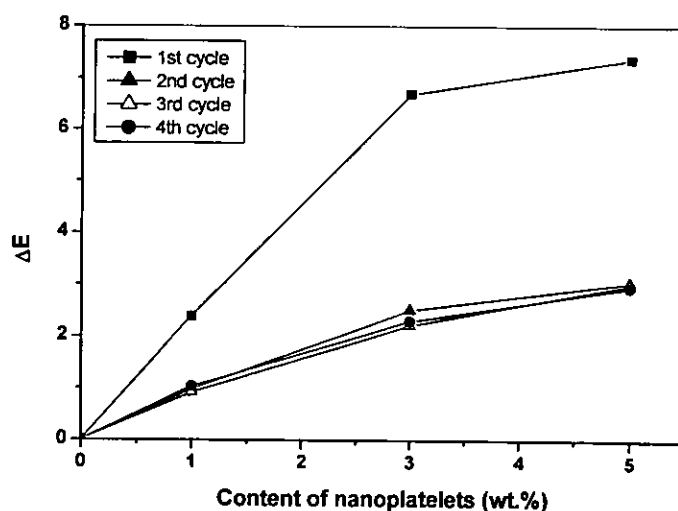


**Figure 5.14** Effect of organoclay content on dissipated energy in PU nanocomposites at 100% strain

Because of the permanent set after the initial loading, the reloaded specimen had long



gauge length and smaller cross-sectional area. The stress and strain response for the loading and reloading cycles in Figure 5.10 to Figure 5.13 were calculated as shown in Figure 5.14 indicating that incorporation of organoclay caused additional energy loss.

When the organoclay content was lower than 5% the effect of organoclay on energy loss was significant. These are agreement with experimental results as discussed above. Table 5.14 lists the simulation results of dissipated energy in the PU nanocomposites for first cycle at strain ratios of 50%, 100% and 200%, respectively. In comparison with experimental results the same trend on the energy loss in the nanocomposites were suggested, except the nanocomposite with 5wt.% organoclay content at 200% strain. For this system the discrepancy between the experimental and the simulation data may be arisen from the dispersion of organoclay in the PU matrix. For higher organoclay content systems, it is difficult to maintain good dispersion quality of organoclay experimentally due to higher viscosity of the mixture. In our previous studies we found that in the formation of PU nanocomposites by an in-situ polymerisation, the viscous behaviour of polyol-organoclay mixture was strongly influenced by the amount of the organoclay. The viscosity was slightly increased when the organoclay was added up to 3wt.%, but with further increasing organoclay content to 5wt.%, the viscosity of the mixture increased to three times than that containing 3wt.% organoclay [13]. Therefore, for the system with 5wt.% organoclay content the individual dispersion of clay layer into the polymer was more difficult to be achieved. Because of the poor dispersion of nanoplatelets, although the much more amount of organoclay was added the interfacial contact areas between polymer chains and surfaces of nanolayers could be not increased significantly. This may be one main explanation of why the additional dissipated energy was not significant when organoclay content was 5wt.%. The simulation process was based on the theory which may limit to consider the effect of the mixture viscosity on organoclay dispersion. So that at large cyclic deformation of 200%, the effect could be more obvious.

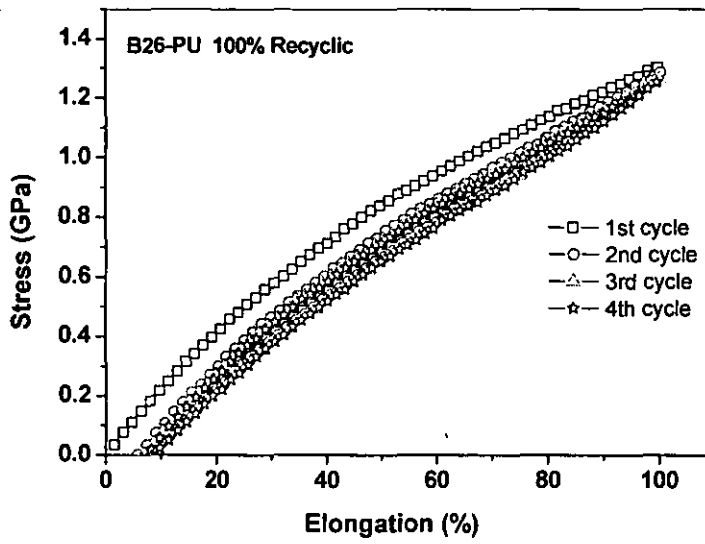
**Table 5.8** Simulation results of dissipated energy in the polymer nanocomposites.

Clay content (%)	Distance Elongation (%)		
	50	100	200
0	3.77	10.39	27.55
1	4.46	12.79	30.69
3	6.02	17.09	39.40
5	6.47	17.77	71.80

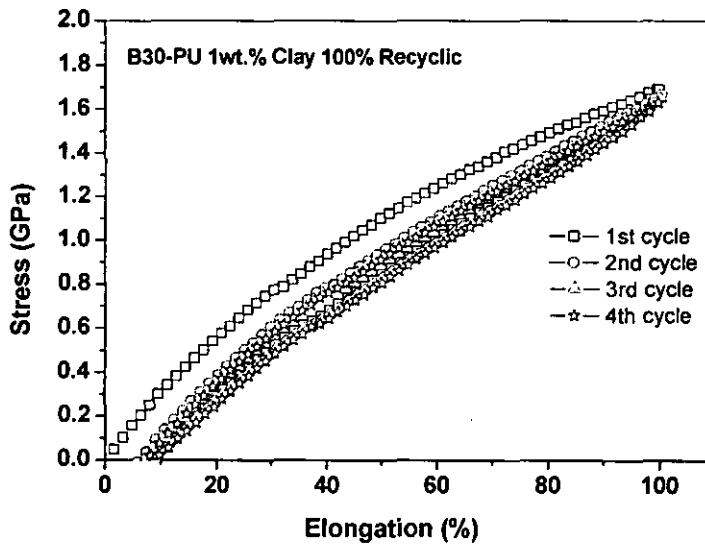
In this study, the effect of organoclay on energy dissipation in exfoliated polymer/organoclay nanocomposites was investigated. Incorporation of organoclay induced an additional energy loss. The effect of organoclay on permanent set was related to strain magnitude. The mechanism of additional energy dissipation caused by organoclay in polymer matrix could be understood, which was contributed to both frictional sliding at interface between polymer chains and the surface of nanolayers and orientation of the nanoplatelets. The simulation results clearly revealed that the nanoplatelets exhibited reversible orientation behaviour at low strain of 50% suggesting that additional energy loss was only contributed by frictional sliding at the interface, whereas the orientation of nanoplatelets at large strain of 200% showed more irreversible deformation behaviour suggesting that the additional energy loss rising from both the interfacial frictional sliding and the orientation of the nanoplatelets. The additional energy dissipation was also influenced by the strength of interactions between polymer chains and clay platelets. The stronger interactions the more energy dissipated.

### 5.3.3 Experimental comparison

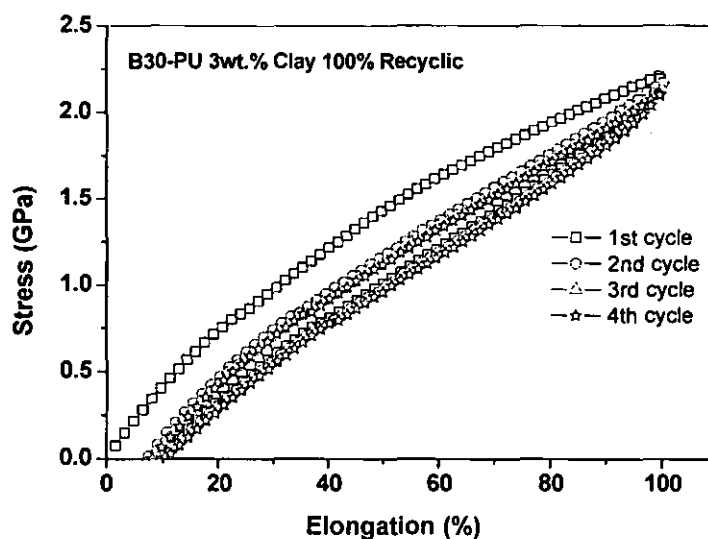
In order to testify the simulation results, some experiments corresponding the simulations were carried out. The results of experiments are shown below:



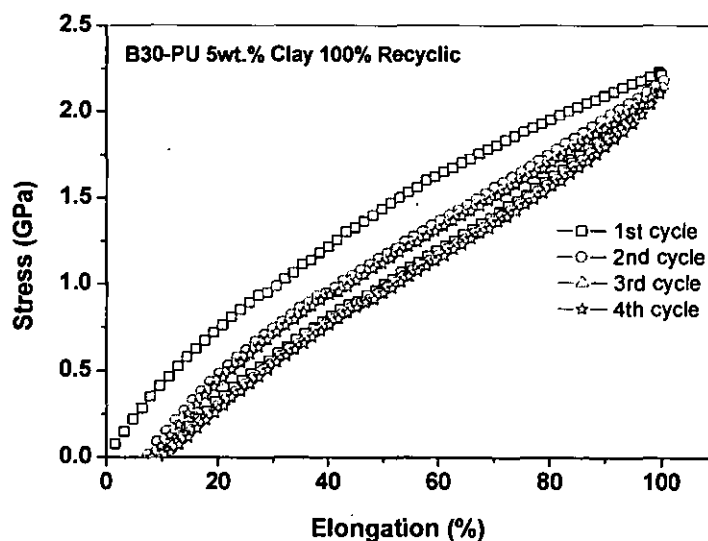
**Figure 5.15** Hysteresis curves for PU nanocomposites with 0wt.% organoclay content, subjected to 100% strain



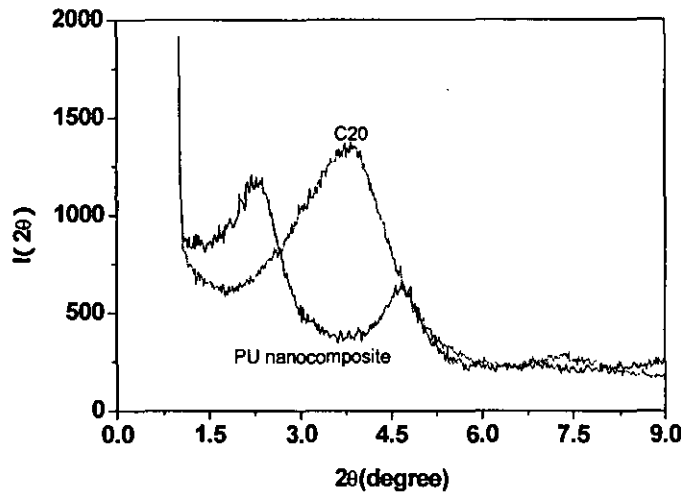
**Figure 5.16** Hysteresis curves for PU nanocomposites with 1wt.% organoclay content, subjected to 100% strain



**Figure 5.17** Hysteresis curves for PU nanocomposites with 3wt.% organoclay content, subjected to 100% strain



**Figure 5.18** Hysteresis curves for PU nanocomposites with 5wt.% organoclay content, subjected to 100% strain



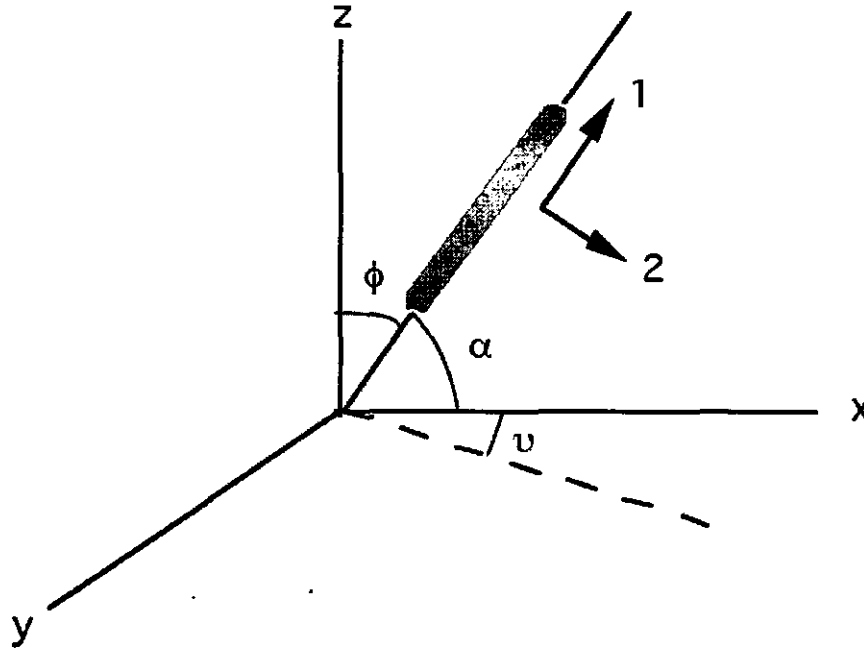
**Figure 5.19** Wide-angle x-ray diffraction patterns for C20-clay and PU/C20-clay nanocomposite (5Wt% C20)

Figure 5.14 to Figure 5.17 shows the typical hysteresis curves of PU nanocomposites with 0wt.%, 1wt.%, 3wt.% and 5wt.% organoclay by weight subjected to 100% strain for loading and unloading cycles 1, 2, 3 and 4, respectively. From these figures the same results can be found with the simulation results. The permanent set of specimen is occurred in the 1<sup>st</sup> cycle. The dissipated energy during the test is increased with the growth of clay content.

The formation of intercalated PUE/organoclay nanocomposites was confirmed by WAXD. Generally, the *d*-spacing of organoclay in polymer nanocomposites depend on the interactions between polymer chains and organoclay [33]. Figure 5.18 shows WAXD for C20-clay and PU/C20-clay nanocomposite with 5wt.% organoclay. There was an observed increase in the *d*-spacing in the nanocomposite as compared to the organoclay. This expresses that the PUE chains were intercalated into the layers of the organoclay, which indicates the samples are typical intercalated PUE/organoclay nanocomposites.

### 5.3.4 Orientation factor of nanofillers

Orientation factor is an important parameter in understanding of the effect of nanofillers on energy dissipation.



**Figure 5.20** Chain segment and coordinate system

The average square end-to-end distance of a random coil molecule is given by:

$$\langle r^2 \rangle_0 = Cnl^2 \quad (5.3)$$

Where  $C$  is the characteristic ratio that depends on the segmental flexibility,  $l$  is the bond length and  $n$  is the number of bonds. A fully oriented molecule has the end-to-end distance:

$$r_{\infty} = l \cos \alpha n \quad (5.4)$$

Where  $\alpha$  is the angle between the chain axis and the individual bonds of the extended chain. The strain ( $\lambda$ ) necessary to reach the completely extended state is given by:

$$\lambda = \frac{r_{\infty}}{((r^2)_0)^{1/2}} = \frac{\cos \alpha \sqrt{n}}{\sqrt{C}} \quad (5.5)$$

The Hermans orientation function ( $f$ ) is probably the quantity most frequently used to characterize the orientation, which relates optical birefringence to segmental orientation. A brief derivation is presented here. The first assumption made is that the polarizability associated with each chain segment can be described by a component parallel to the chain axis ( $p_1$ ) and a component perpendicular ( $p_2$ ) to the same chain axis (Figure 5.20). The orientation of the chain segment with respect to coordinate system is schematically shown in Figure 5.20. It is assumed that the electrical vector of the propagating light is along the z-axis. The electrical field parallel to the chain axis is  $E_z \cos \phi$  and the polarization along the chain segment is given by  $p_1 E_z \cos \phi$ . The contribution of this polarization to the polarization along the z axis amounts to  $p_1 E_z \cos^2 \phi$ .

The contribution to polarization along z from the transverse polarization of the segment (i.e. along vector 2; Figure 5.19) is by analogy equal to  $E_z p_2 \sin^2 \phi$ . The total polarization along the z-axis caused by the electrical vector in the z direction ( $P_{zz}$ ) is equal to the sum of these two contributions:

$$P_{zz} = E_z (p_1 \cos^2 \phi + p_2 \sin^2 \phi) \quad (5.6)$$

The polarizability in the z direction ( $p_{zz}$ ) is given by:

$$p_{zz} = \frac{P_{zz}}{E_z} = p_1 \cos^2 \phi + p_2 \sin^2 \phi \quad (5.7)$$

Let us now consider the case where the electrical vector is oriented along the x-axis. The polarizability in the x direction ( $p_{xx}$ ) becomes:

$$p_{xx} = p_1 \cos^2 \alpha + p_2 \sin^2 \alpha \quad (5.8)$$

which, since  $\cos \alpha = \cos \nu \sin \varphi$ , may be modified to:

$$p_{xx} = p_2 + (p_1 - p_2) \sin^2 \varphi \cos^2 \nu \quad (5.9)$$

The polarizability tensor ( $p_{ij}$ ) can be converted to the corresponding refractive index tensor ( $n_{ij}$ ) according to the Lorentz-Lorenz equation:

$$\frac{n_{ij}^2 - 1}{n_{ij}^2 + 2} = \left( \frac{4}{3} \pi \right) p_{ij} \quad (5.10)$$

Insertion of Eqs. (5.8) and (5.9) in Eq. (5.10) yields the expressions:

$$\frac{n_{zz}^2 - 1}{n_{zz}^2 + 2} = \left( \frac{4}{3} \pi \right) (p_1 \cos^2 \varphi + p_2 \sin^2 \varphi) \quad (5.11)$$

$$\frac{n_{xx}^2 - 1}{n_{xx}^2 + 2} = \left( \frac{4}{3} \pi \right) (p_2 + (p_1 - p_2) \sin^2 \varphi \cos^2 \nu) \quad (5.12)$$

The birefringence ( $\Delta n$ ) and the average refractive index  $\langle n \rangle$  are defined as follows:

$$\Delta n = n_{zz} - n_{xx} \quad (5.13)$$



$$\langle n \rangle = \frac{1}{2} (n_{xx} + n_{zz}) \quad (5.14)$$

Combination of equation 5.13 and 5.14 yields the expressions:

$$n_{xx} = \langle n \rangle - \frac{\Delta n}{2} \quad (5.15)$$

$$n_{zz} = \langle n \rangle + \frac{\Delta n}{2} \quad (5.16)$$

Subtraction of Eq. (5.11) from Eq. (5.12) yields:

$$\frac{n_{zz}^2 - 1}{n_{zz}^2 + 2} - \frac{n_{xx}^2 - 1}{n_{xx}^2 + 2} = \frac{6\langle n \rangle \Delta n}{(n_{zz}^2 + 2)(n_{xx}^2 + 2)} \approx \frac{6\langle n \rangle \Delta n}{(\langle n \rangle^2 + 2)^2} \quad (5.17)$$

Insertion of Eqs. (5.15) and (5.16) into Eq. (5.17) yields, after algebraic simplification, the following expression:

$$\Delta n = \frac{(\langle n \rangle^2 + 2)^2}{6\langle n \rangle} \frac{4\pi}{3} (p_1 - p_2) (1 - \sin^2 \vartheta - \sin^2 \vartheta \cos^2 \nu) \quad (5.18)$$

A great number of segments are considered and the assumption made at this stage is that orientation is uniaxial. All angles  $\nu$  are equally probable. The average square of the cosine of  $\nu$  may be calculated as follows:

$$\langle \cos^2 \nu \rangle = \frac{1}{2\pi} \int_0^{2\pi} \cos^2 \nu = \frac{1}{2} \quad (5.19)$$

Insertion of equation 5.19 in equation 5.18 and averaging for all segments over all theta angles give:

$$\Delta n = \frac{(\langle n \rangle^2 + 2)^2 4\pi}{6 \langle n \rangle} (p_1 - p_2) \left( 1 - \frac{3 \langle \sin^2 \theta \rangle}{2} \right) \quad (5.20)$$

Hermans orientation function ( $f$ ) is defined as

$$f = \frac{\Delta n}{\Delta n_0} = 1 - \frac{3 \langle \sin^2 \theta \rangle}{2} = \frac{3 \langle \cos^2 \theta \rangle - 1}{2} \quad (5.21)$$

where the maximum (intrinsic) birefringence  $\Delta n_0$  is given by

$$\Delta n_0 = \frac{(\langle n \rangle^2 - 2)^2 4\pi}{6 \langle n \rangle} (p_1 - p_2) \quad (5.22)$$

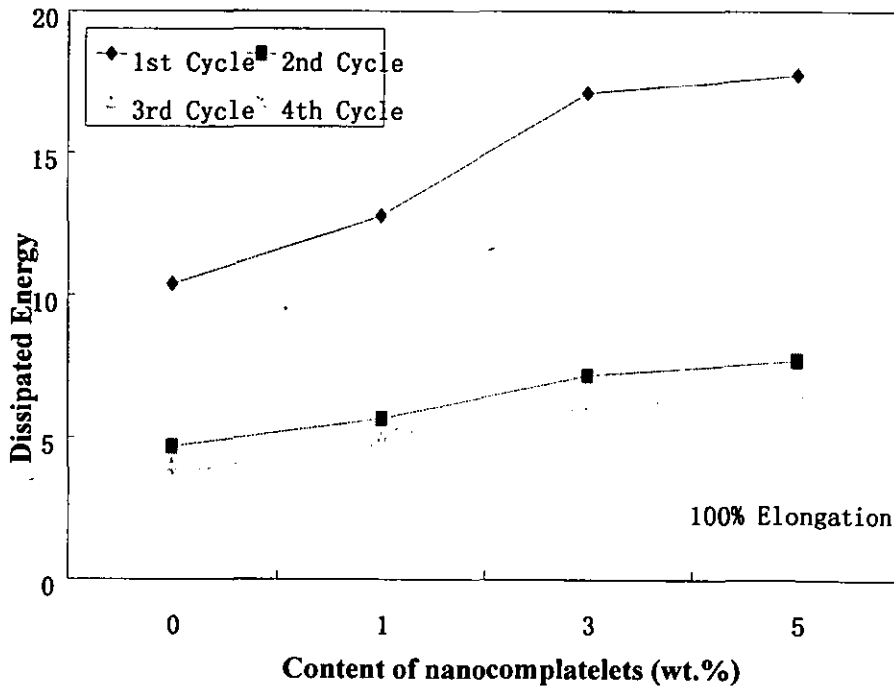


**Figure 5.21** Dissipated energy at 100% elongation

Figure 5.21 shows the dissipated energy with elongation the content of nanoplatelets various from 0wt.% to 5wt.% at 100%.

It can be seen clearly from Figure 5.21, the energy dissipated at the first cycle is much greater than that at the following cycles, and the dissipated energies almost were the same at the second, third, and the forth cycle representing by the equal quantity.

This results represented as that the dissipated energies of the first cycle are greater than the following cycles because the permanent orientation of the additional nanoplatelets only occurred in the first time of material stressing which can be seen in Table 5.15 and Figure 5.22.

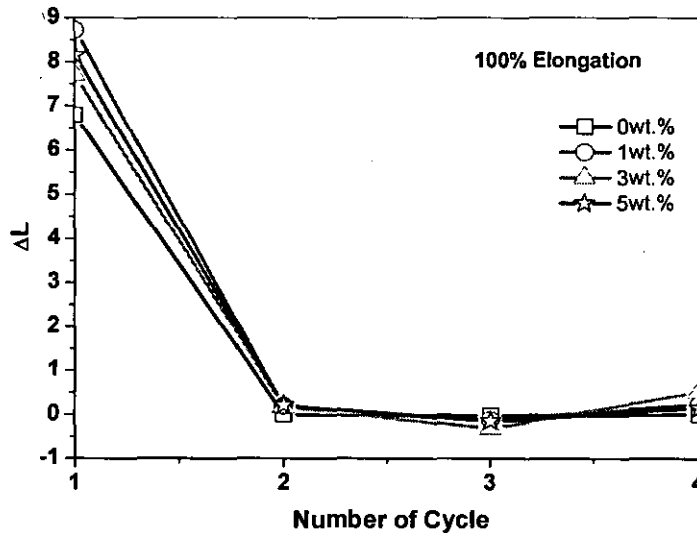


**Figure 5.22** The permanent set occurred in each cycle.

It can be found that the orientation of the nanoplatelets almost is reversible within deformation of 100%. The dissipated energy in 2<sup>nd</sup>, 3<sup>rd</sup> and 4<sup>th</sup> cycles is the same, although the orientation of nanoplatelets occurred. This indicates that the orientation with deformation of 100% does not contribute any extra heat to the polymer matrix.

**Table 5.9.** Variation of orientation factor (5wt.% nanoclay)

Number of cycle \\Elongation (%)	0	50	100	50	0
Cycle 1	0	0.23611	0.68533	0.23714	0.00007
Cycle 2	0.00007	0.23712	0.68437	0.23611	0.00003
Cycle 3	0.00003	0.23519	0.68447	0.23650	0.00004
Cycle 4	0.00004	0.25632	0.68488	0.23679	0.00003

According to the above analysis, it is clear the addition of nanoplatelets leads to the increase in energy dissipation, which mainly results from the friction of polymer chains and the surface of the nanoplatelets.

As we have discussed, the material will cause the orientation of the additional nanoplatelets while the material was stressed. The orientation of nanoplatelets included both large angles orientation and small angle orientation. We believe that only the small angle orientation is resumable. The small angle orientation will be reverted to the original position while the stress of material is unloaded. The energy dissipated which are absorbed while the material stressing will be released again (see Figure 5.23).

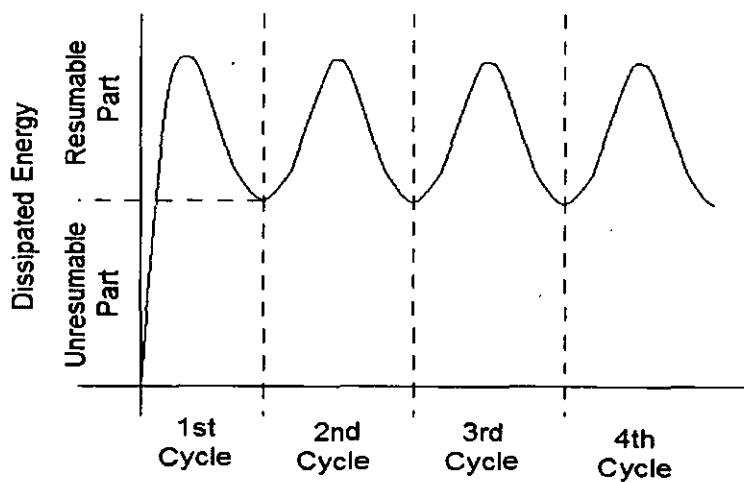


**Figure 5.23** Schematic map of the relationship between the unresumable dissipated energy and the resumable dissipated energy in the recyclic test

It is considered that the large angle orientation is beyond retrieved and cannot be reverted to the original position while the stress of material is unloaded. And the energy dissipated which are absorbed while the material stressing cannot be released again after the stress of the material is removed. This type of the orientation of the addition of nanoplatelets is permanent.

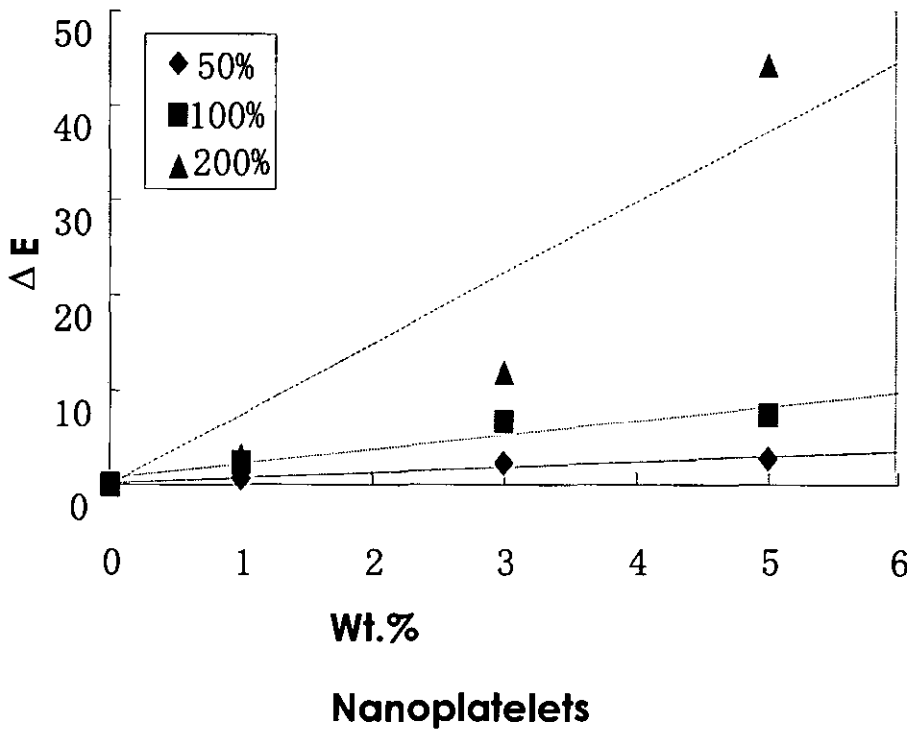


**Figure 5.24** Dissipated energy of the 1st cycle of the polymer nanocomposites recyclic simulation versus nanoplatelets content at different deformations (50%, 100%, and 200%).

Figure 5.24 shows the dissipated energy in the 1<sup>st</sup> cycle of the polymer nanocomposites recyclic simulation versus nanoplatelets content at deformations various from 50% to 200%. The  $\Delta E$  in the figure is defined as:

$$\Delta E = |E_2 - E_1| \quad (5.23)$$

Where  $\Delta E$  is the energy difference between the 1<sup>st</sup> and 2<sup>nd</sup> cycle of the simulation,  $E_2$  is the dissipated energy in the 2<sup>nd</sup> cycle of the simulation, and  $E_1$  is the dissipated energy in the 1<sup>st</sup> cycle of the simulation.

The results shown in Figure 5.24 indicate  $\Delta E$  increased with increasing the content of additional nanoplatelets. Moreover, the increase of  $\Delta E$  is significant as the material deformation increased to 200%.

## **5.4 Enhancement of fatigue durability by incorporation of clay and its mechanism**

### **5.4.1 Introduction**

The cyclic fatigue is a type of time-dependent failure which was a machine part or structure. The failure is due primarily to repeated cyclic stress from a maximum to a minimum caused by a dynamic load. A familiar example of a fatigue failure is the final fracture of a piece of wire that is bent in one direction then the other for a number of cycles. This type of behaviour is termed low-cycle fatigue and is associated with large stresses causing considerable plastic deformation with failure cycles,  $N_f$ , in the range of  $<10^2$  to  $10^4$ . The other basic type of fatigue failure is termed high-cycle fatigue and is characterized by loading which causes stress within the elastic range of the material and many thousands of cycles of stress reversals before failure occurs often with  $N_f > 10^5$  (sometimes  $>10^2$  to  $10^4$ ).

Fatigue has been a major concern in engineering for over 100 years, and there is a very large amount of literature available. The importance of an knowledge of fatigue in engineering design is emphasized by one estimation that 90 percent of all service failures of machines are caused by fatigue and 90 percent of these fatigue failures result from improper design.

Fatigue failures of normally ductile materials in structural and machine members are very much different in appearance than failure under a static loading. Under quasi-static loading of the tensile test, considerable plastic flow of the material precedes fracture and the fracture surface has a characteristic fibrous appearance. This fibrous appearance can also be noted in the ductile part of the fracture surface of Charpy impact specimens. A fatigue crack, however, appears entirely different. The crack begins at a surface, often at the point of high stress concentration. Once the crack begins, the crack itself forms an area of even higher stress concentration (also stress intensify factor), and it proceeds to propagate progressively with each application of load until the remaining stressed area finally becomes so small that it cannot support the load statically and a sudden fracture results. In fatigue failures, then, a characteristic appearance is always evident. The fatigue portion begins at the point of high-stress concentration and spreads outward showing concentric rings (known as beach marks) as it advances with repeated load. The final fracture surface has the same appearance as that of a ductile tensile specimen with a deep groove. The fracture is brittle due to constraint of the material surrounding the groove and has a crystalline appearance. The failure was not because the material crystallized as is sometimes supposed; it always was of crystalline structure.

Fatigue cracks, then, begin at a point of high-stress concentration. The severity of those stress concentrations will vary, even with carefully prepared laboratory specimens. In addition, the rapidity with which the crack propagates will vary. The cracks are irregular and will follow various paths around regions of stronger metal. A consequence of this manner of crack propagation is wide variation in time to failure of a number of seemingly identical test specimens loaded with the same load. For this reason a number of statistical procedures have been developed for interpreting fatigue data.

The basic mechanism of a high-cycle fatigue failure is that of a slowly spreading crack that extends with each cycle of applied stress. In order for a crack to propagate,

the stress across it must be tension; a compression stress will simply close the crack and cause no damage. One way, then, of preventing fatigue or at least extending the fatigue life of parts is to reduce or eliminate the tensile stresses that occur during loading by creating a constant compressive surface stress, called a residual stress, in the outer layers of the specimen. We can picture how it is possible to induce a constant compressive stress of this type by a simple analogy. Consider a bar with a small slot cut in the surface. If we force a wedge tightly into this slot, the wedge and the material in the bar adjacent to the slot will be in a compressive stress state. If a tensile stress is now applied to the bar, no tensile stress can exist in the region of the slot until the compressive stress caused by the wedge is overcome. In other words, the tensile stress in the region of the slot will always be less than in a region removed from the slot by an amount equal to the magnitude of the residual compressive stress.

Favourable compressive stresses can be induced in parts by more practical methods than cutting slots. One of the most common methods is that of shot peening. Shot peening is a process in which the surface of the part is impacted by many small steel balls moving at high velocity. This process plastically deforms the surface of the part and actually tends to make it somewhat bigger than it was. The effect is the same as the wedge. A now larger surface is forced to exist on a smaller sub-layer of material with the net result that a compressive stress is induced in the outer layer making it more resistant to fatigue failure.

In many cases, failure of engineering structures through fatigue can be fatal; one example is that of the Tay Rail Bridge disaster. Often disasters occur because engineering structures contain cracks - arising either during production or during service (e.g. from fatigue). For instance, growth of cracks in pressure vessels due to crack propagation could cause a fatal explosion. If failure were ever to happen, we would rather it were by yield or by leak before break.

Since cracks can lower the strength of the structure beyond that due to loss of



load-bearing area a material property, above and beyond conventional strength, is needed to describe the fatigue resistance of engineering materials. This is the reason for the need for fatigue mechanics - the evaluation of the strength of cracked structures.

#### **5.4.2 Enhancement of fatigue durability by incorporation of clay**

The formation of intercalated PU/organoclay nanocomposites was confirmed by WAXD. Generally, the *d*-spacing of organoclay in polymer nanocomposites depend on the interactions between polymer chains and organoclay [34]. Figure 5.19. shows WAXD for C20-clay and PU/C20-clay nanocomposite with 5wt.% organoclay. There was an observed increase in the *d*-spacing in the nanocomposite as compared to the organoclay. This expresses that the PUE chains were intercalated into the layers of the organoclay, which indicates the samples are typical intercalated PU/organoclay nanocomposites.

Fatigue property of materials is described in terms of the cyclic fatigue life (or durability). The properties are restricted to the results of constant-amplitude tests on specimens. It is generally thought that the results of these tests reflect the basic fatigue behaviour of the material. Mechanical property of the material should include fatigue property, but quite often reporting of fatigue properties is the fatigue durability. In this research the fatigue durability of the intercalated PU/organoclay nanocomposites containing different hard segments and organoclay contents were investigated in chapter 4.

In the experiment, the standard frequency of 1.44 Hz was used and the specimens tested at 100% stretching. As indicated in Table 5.15, the results show that with increasing hard segment content from 18% to 36% the fatigue durability slightly increased. Takahara et al. [34] found that hard segments can determine the fatigue resistance of polyurethanes. However, when the organoclay was incorporated, the

fatigue durability is significantly improved. The results also indicate that the addition of 3wt% of the organoclay led to the best result and the fatigue durability of the nanocomposite was increased about average of 10 times than that of pure PUE. The effect of organoclay is particularly significant as compared to that of hard segment. It was also noted that with higher organoclay content (wt.5%), although the fatigue durability was still greatly increased the improvement effect of organoclay became weak compared to these samples with lower organoclay contents. This may be resulted from the dispersion of organoclay in the PUE matrix. At higher clay content systems, it is difficult to maintain good dispersion quality of organoclay due to higher viscosity of the mixture. It was found that in the formation of PUE nanocomposites by an in-situ polymerisation, the viscous behaviour of polyol-organoclay mixture was strongly influenced by the amount of the organoclay. The viscosity was slightly increased when the organoclay was added from 0 to 3wt.%, but with further increasing organoclay content to 5wt.%, the viscosity of the mixture increased to three times than that containing 3% organoclay. The results are shown in Figure 5.19, suggesting that as the organoclay content is 3wt%, the critical viscosity of the mixture is reached.

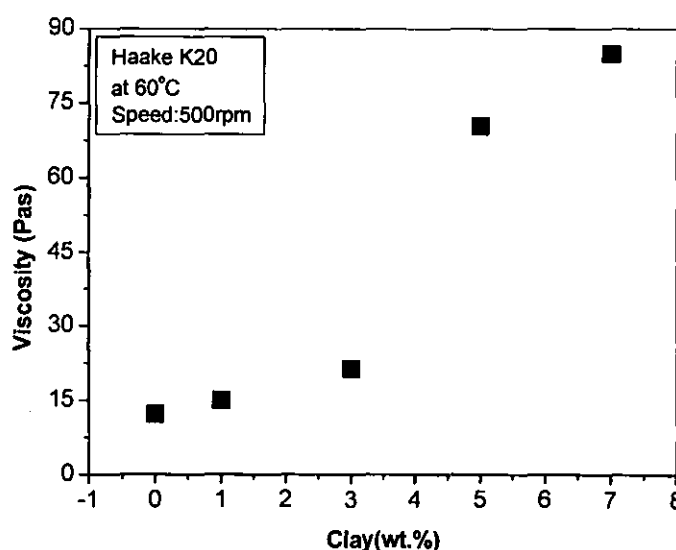


**Figure 5.25** Effect of organoclay on the viscosity of polyol.

Now the question remains here what factors lead to such significant improvement of the fatigue durability of PUE. Christenson [16] et al. indicated that the hard domain morphology of PUE is responsible for the deformation behaviour. PU exhibits micro-phase separated morphology. The hard domains serve as physical crosslinks and also reinforcement to the soft segment matrix. Depending on the hard segment content, the morphology of hard domain changes from isolated domains to interconnected domains [35]. The organoclays are dispersed in the form of swollen clay particles. Introduction of organoclay that preferentially interact with one of the polymer phases can induce large changes in morphology [11]. And introduction of organoclay that causes the existence of extremely large interfacial contact area between polymer chains and the surface of organoclay layers implies strong interfacial interactions. For the PU/organoclay nanocomposite system, the deformation behaviour, which is related to both interconnecting polymer chains and silicate platelets, is more complex than that of bulk polymer. The morphology changes and interfacial interactions may induce additional mechanisms of failure and significant energy consumption. Due to these factors, there is a necessary to get better understand the mechanism of the fatigue life enhancement of PU nanocomposites. For this reason, the effect of the morphology of PU/organoclay nanocomposites, the deformation behaviour clay nanoplatelets and its contribution to energy dissipation are discussed as follows, separately.

When organoclay was incorporated, the size of aggregates of hard domains was reduced. The size of aggregates of hard segment domains was significant reduced by the incorporation of organoclay. The average size decreased by about 50% when the organoclay level was of 3wt.%. Then further increasing the organoclay content, the aggregate size of hard segment domains was not significantly affected further. As well known, the curing dynamics plays a very important role for PU formation. The morphology and physical properties of PUE materials depend to a large extent on the

degree of curing. A typical chemical reaction is thermally activated, and thus, requires time for heat transfer into the reaction process involving the transformation of low molecular weight liquids into polymer network by means of an exothermic chemical reaction. In PUE formation, chemical reactions between isocyanate group and hydroxyl functionalities of polyol take place during the cure. The formation of micro-phase morphology is related to the reaction process [17, 36]. Due to the fast chemical reaction there was no enough time to develop big hard domain phase. And the fast chemical reaction also leads to the existence of sufficient number of small hard domains and wider interfacial region [37] between soft and hard segment phases. The interfacial regions between the hard and soft segments were the first to be disrupted [38]. The small hard segment domains with wider interfacial region could act as micro-barriers to lead a rise of fatigue resistance.

#### **5.4.3 Mechanism of the enhancement of fatigue durability**

Fracture resistance in polymeric materials is generally attributed to two principle mechanisms that absorb or dissipate energy as cracks advance through the system of polymer chains. One contribution comes from the energy required to extend the polymer chains, or some subsection, to the point of rupture. The second contribution arises from viscous dissipation. Viscoelastic loss associate with chain deformation in region around the crack tip is significant in determining the fracture resistance in polymers [39, 40]. It can be considered that during the fatigue test the deformation of PUE/organoclay nanocomposites involves from both stretching and orientation of hard segments and nanoplatelets. In fact, the total energy required contributes to not only extending and orientating the hard domains, and also to silicate platelets, and to overcoming internal frictions between polymer chains and between polymer chains and nanoplatelets.

The deformation behaviour of the silicate layers during the fatigue test can be observed by determining the nanolayer d-spacing using WAXD technique. The d-spacing was measured for a PUE nanocomposite sample containing 5wt.%

organoclay at original state, under uniaxial tension and after uniaxial tension. The experimental schedule was as follows: the specimen was uniaxial stress and held at given length for 10 minutes, and then  $d$ -spacing was measured. After test the stretching force was removed, and the  $d$ -spacing was measured again after a lapse of ten minutes. The strain amplitude was from 0% to 100% as same as that in the fatigue test. Figure 5.26 shows the WAXD results. For original sample (unstretched), the  $d$ -spacing value is 3.69nm and for 100% strain the  $d$ -spacing reached to 4.08nm. However, as the stretching force was removed the  $d$ -spacing nearly went back to the original position at about 3.69nm, indicating that the nanoplatelets exhibits reversible deformation behaviour under 100% stretching amplitude and behaves like elastic spring. Table 5.16 shows the  $d$ -spacing variation under different stains.

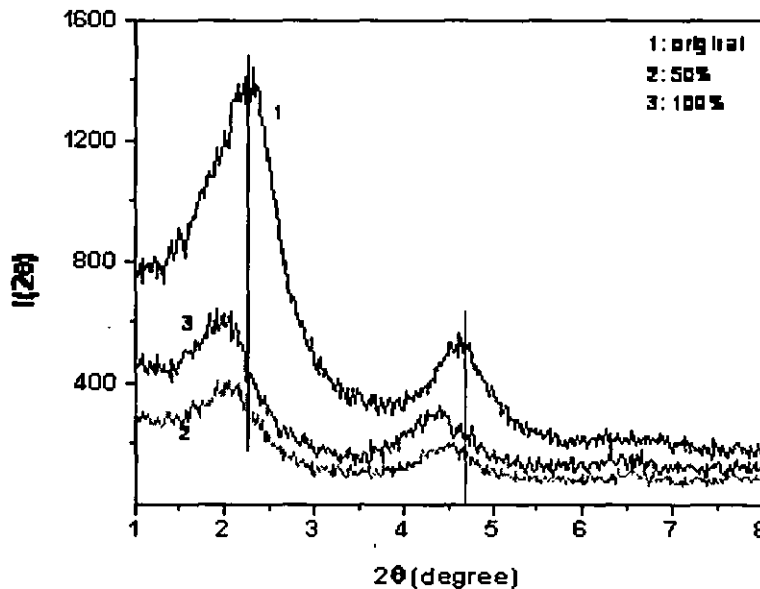


**Figure 5.26** WAXD results under different stains.

From the above results, it can be assumed that in the intercalated PU/organoclay nanocomposite, there are nanospring-like systems. Each nanospring system is composed by two nanoplatelets and polymer chains, which are intercalated in the two

nanoplatelets. During the fatigue test, the nanospring systems are capable of absorbing deformation energy, which was converted to potential energy of the systems. When the applied force was removed, the nanospring system is back to original position. The concentrated energy for each nanospring system will be released by intercalated PUE chain. Figure 5.27 shows a schematic of the d-spacing change during the fatigue test. These nanospring systems could play an important role in reducing the concentrated stress in the material and preventing the development of the fatigue cracks. Therefore, these could also give a rise of fatigue resistance of PUE.

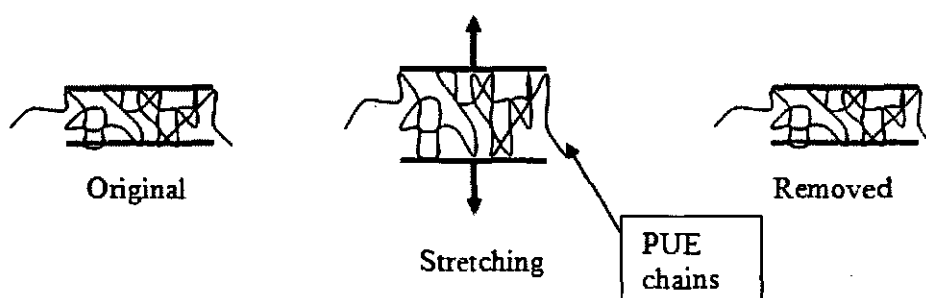


**Figure 5.27** Schematic diagram of d-spacing on nanoscale change during stretching.

**Table 5.10.** WAXD results for the stretching test of PUE-organoclay (5% by weight) nanocomposite

Status	d-spacing (nm)
Un-stretched (original)	3.69
Stretched (to 25%) (status A)	3.87
After stretching force was removed from status A	3.72
Stretched (to 50%) (status B)	3.92
After stretching force was removed from status B	3.67

Stretched (to 75%) (status C)	3.98
After stretching force was removed from status C	3.75
Stretched (to 100%) (status D)	4.08
After stretching force was removed from status D	3.67

For PU/organoclay nanocomposites, the hysteresis and the associated mechanical loss processes should be attributed to the deformation of both particles during cycling process. Irreversible deformation during first loading is responsible for hysteresis in stress-strain respond. The influence of organoclay on the fatigue durability was evaluated by hysteresis measurements at strain ratios of 50, 100%. With higher organoclay content, the loop area was gradually increased as shown in Figure 5.28 at 100% strain for first cycle. The total of dissipated energy was calculated as shown in Figure 5.29. As seen, the additional energy loss was caused by organoclay and it was slightly increased when the organoclay content was less than 3%. The permanent set was also measured on the 1<sup>st</sup> unloading cycle as shown in Figure 5.29. The addition of organoclay resulted in a slight increase in displacement (permanent set) when strain ratios were 50 and 100%. The results indicate that irreversible changes of microstructure took place resulting from the addition of organoclay.

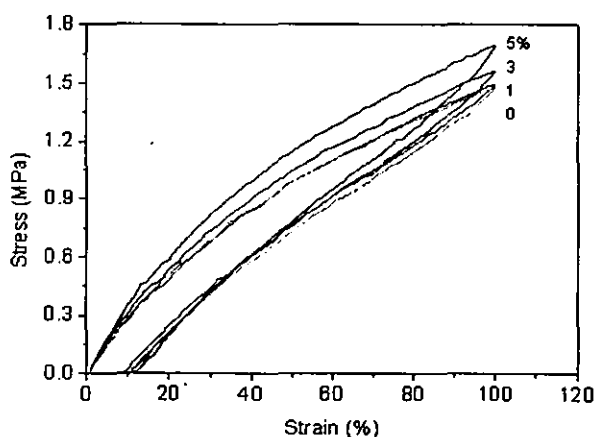


**Figure 5.28** Hysteresis curves for the PU/organoclay nanocomposites at 100% strain.

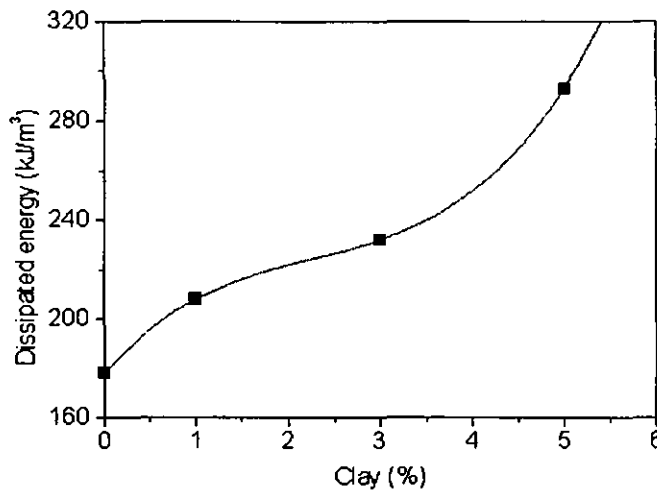


**Figure 5.29** Effect of organoclay on dissipated energy

Hysteresis describes the energy loss for internal friction contribution [41]. The additional energy loss caused by the incorporation of organoclay may be contributed to the orientation of nanoplatelets and frictional sliding at the interface between the surface of the organoclay layer and PU molecules. Additionally, if the silicate platelets are unable to return to their original positions when the force is removed this also in turn disrupts the PUE chains to relax. So the PUE nanocomposites show higher hysteresis and permanent set value than that of the pure PU. As a consequence, the energy loss could relate to the imposed tension.



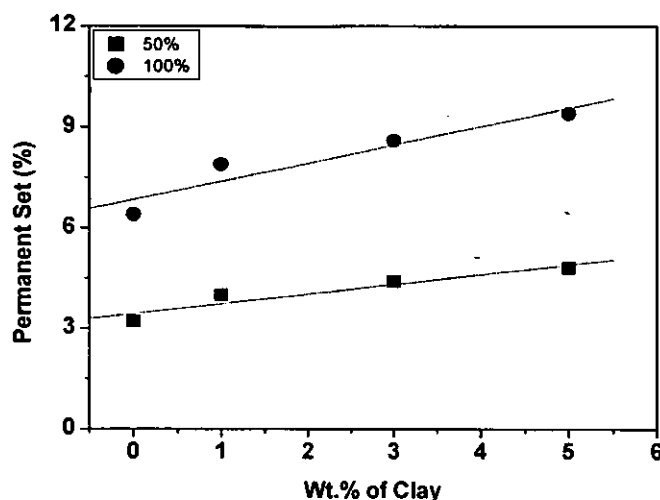


**Figure 5.30** Effect of the organoclay on permanent set.

In order to get better understand the nature of energy dissipation of PUE nanocomposites during fatigue test molecular dynamics simulation technique (MD) was used to simulate the recycle test process. The simulations were performed up to a maximum deflection of 100%. The strain on each simulated system was returned to zero at the end of each cycle. Models and simulation parameters can be found in reference 42.

As the data of the variation of orientation factor,  $f(\theta)$ , ( $= (3\langle \cos^2\theta \rangle - 1)/2$ ), of the simulated system with 5wt.% clay shows in chapter 4. It can be found that the orientation of the nanoplatelets almost is reversible within deformation of 100%. The dissipated energy in 2<sup>nd</sup>, 3<sup>rd</sup> and 4<sup>th</sup> cycles is the same, although the orientation of nanoplatelets occurred. This indicates that the orientation does not contribute any extra heat to the PUE matrix.

According to the above analysis, it is clear the addition of organoclay leads to the increase in energy dissipation, which mainly results from the friction of PUE chains

and the surface of the organoclay. Theoretically, the increase in energy dissipation will lower the fatigue durability. However, the fatigue durability of PUE significant increased by the incorporation of organoclay. We believe that firstly, the reduced hard-segment domain size with wider interfacial region as micro-barriers to lead a rise of fatigue resistance. Secondly, the orientation of clay nanoplatelets is reversible during fatigue test, which does not contribute any dissipated energy, which generates heat, to the PU matrix. Thirdly, the nanospring acts as a point, which can stop the crack growth when the tip of a crack reaches the nanospring. In fact, the effect of addition of organoclay on the increase in dissipated energy is also not very significant. Overall, the positive effect on the improvement of fatigue durability is much more important than the negative one of heat generated by the friction between PU chains and the surface of organoclay, which will lower fatigue durability.

## Reference

1. C. Caroli and Ph. Nozières, *Eur. Phys. J. B* **4**, 233, (1998).
2. I.M. Ward and D.W. Hadley, *An Introduction to the Mechanical Properties of Solid Polymers*, John Wiley and Sons, Chichester (1993).
3. B.N.J. Persson, *Surf. Sci.*, **401**, 445, (1998).
4. S. Ciliberto and C. Laroche, *Eur Phys. J.*, **B 9**, 551,(1999).
5. A.A. Spector, *Proceeding of the Japan International Tribology Conference Nagoya*, 1243, (1990).
6. A.M. Shapiro, *Wear* **237**, 223,(2000).
7. K. J. Yao, M. Song, D. J. Hourston, D. Z. Lou, *Polymer*, **3**, 1017, (2002).
8. Z. Wang, T.J. Pinnavia, *Chem. Mater.* **10**, 3769, (1998).
9. Y.I.Tien, K.H. Wei, *Macromolecules* **34**, 9045, (2001).
10. M. Song, D.J. Hourston, K.J.Yao, J.K.H. Toly, *Appl. Polym. Sci*, **90**, 3239,(2003).
11. B. Finnigan, D. Martin, P. Halley, R. Truss, K. Campbell, *Polymer*, **45**, 2249, (2004).

12. M.A. Osman, V. Mittal, M. Morbidelli, U.W. Suter, *Macromolecules*, **36**, 9851,(2003).
13. K.J. Yao, *High Performance Polyurethane-Organoclay Nanocomposites*, **PhD thesis**, Loughborough University,(2005).
14. J. Schijve, *Fatigue of Structure and Materials*, **Kluwer Academic Publishers**, (2001).
15. H. J. Qi, M. C. Boyce, *Mechan. Mater.*, **37**, 817, (2005).
16. E. M. Christenson, J. M. Anderson, A. Hiltner, E. Baer, *Polymer*, **46**,11744, (2005).
17. J. E. Kresta, *60 years of polyurethanes*, Lancaster PA, **Technomic Publications**, (1998).
18. C. Hepburn, *Polyurethane elastomers*, **Applied Science**, London, (1982).
19. R.S. Sinha, M. Okamoto, *Prog. Polym. Sci.* , **28**, 1539, (2003).
20. E. P. Giannelis, *Adv. Mater.*, **8**, 29, (1996).
21. M. Biswas, R. S. Sinha, *Adv. Polym. Sci.* ,**155**,167, (2001).
22. E. P. Giannelis, *Appl. Organomet. Chem* , **12**, 675, (1998).
23. M. A. Osman, V. Mittal, M. Morbidelli, U. W. Suter, *Macromolecules* ,**36**,9851, (2003).
24. J.W. Gliman, C. L. Jackson, A. B. Morgan, Harris R. *Chem Mater* ,**12**,1866, (2000).
25. M. Alexander, G. Beyer, C. Henrist, R. Cloots, A. Rulmont, R. Jerome, P. Dubois, *Macromol. Rapid. Commun.* , **22**, 643, (2001).
26. Putz, M.; Kremer, K.; Grest, G. S. *Europhys. Lett.* , **49**, 735, (2000).
27. M. P. Allen and D. J. Tildesley, *Computer Simulation of Liquids* **Clarendon**, Oxford, (1987).
28. D. Gersappe, *Phys. Rev. Lett.*, **89**, 058301, ( 2002).
29. M. Szycher, *Szycher's Handbook of Polyurethanes.* , Boca Raton: **CRC press**, (1999).
30. C. Hepburn, *Polyurethane Elastomers*. **Applied Science Publishers**, London

and New York, (1982).

31. N. Grossiord, J. Loos and C. E. Koning, *J. Mater. Chem.*, **15**, 2349, (2005).
32. J. Lai, J. E. Mark, *Advances in elastomers and rubber elasticity*. Plenum Press, New York (1986).
33. R. A. Vaia, E. P. Giannelis, *Macromolecules* , **30**, 8000, (1997).
34. A. Takahara., *Polymer Physics Japan*, . **25**, 894, (1982).
35. J. T. Koberstein, A. F. Galambos, T. M. Leung, *Macromolecules* , **25**, 6195, (1992).
36. C. Hepburn, *Polyurethane elastomers*, **Applied Science**, London, (1982).
37. J. Jin, M. Song, *Thermochimics Acta*, Accepted for publication.
38. L.M. Lui, M. Sumita, K. Miyasaka, *Macromolecular Science, Physics*, **B29**, 309, (1989).
39. H.K. Mueller, W. G Kanuss, *Trans Rheol* , **15**, 217, (1971).
40. E. H. Andrews, *J Mater Sci.* , **9**, 887, (1974).
41. K. A. Mazich, A. Samus, A. Smith, G. Rossi, *Macromolecules* , **24**, 2766, (1991).
42. M. Song, L. Chen, *Macromolecular Theory & Simulations*, **15**, 238, (2006).

## CHAPTER 6

# EFFECT OF GEOMETRY OF NANOFILLERS ON FRACTURE OF POLYMERS

### 6.1. Introduction

Compared to neat polymers, people expected these fillers to enhance properties including tensile strength, heat distortion temperature, and toughness, etc. Various modalities of nanoparticles have been added to polymers to fabricate nanocomposites. Some results shows the enhancement of nanoparticles to polymer, such as Bernd Wetzal et. al. [1] has studied effect of reinforcing influences of series of nanocomposites containing varying amounts of nanoparticles, either titanium dioxide ( $\text{TiO}_2$ ) or aluminium oxide ( $\text{Al}_2\text{O}_3$ ), exerted on the mechanical and fracture mechanical properties of epoxy resins, particularly with regard to fracture and toughening mechanisms. It was found that the presence of nanoparticles in epoxy induces various fracture mechanisms, e.g. crack deflection, plastic deformation, and crack pinning. At the same time, nanoparticles can overcome the drawbacks of traditional tougheners (e.g. glass beads or rubber particles) by simultaneously improving stiffness, strength and toughness of epoxy (see Figure 6.1), without sacrificing thermo-mechanical properties. At the filler content of 5 vol.%  $\text{Al}_2\text{O}_3$  the fracture toughness increases by 60%, and at 10 vol.% the improvement reaches 120%. EP/alumina nanocomposites behave considerably tougher than EP/ $\text{TiO}_2$ . Some of the authors considered the additional nanoparticles do not represent any significant improvement to polymers such as Dušan Galusek et. al. [2, 3] has studied  $\text{Al}_2\text{O}_3$ -SiC composites by warm pressing of poly(allyl)carbosilane-coated submicrometre alumina powder followed by pressureless sintering in the temperature interval between 1700 and 1850 °C. No significant influence on mechanical properties was detected, and the hardness and fracture toughness of the composites are comparable to those of monolithic alumina. The Vickers hardness of IP (polymer infiltration of

porous alumina matrix) specimens sintered at  $T < 1850\text{ }^{\circ}\text{C}$  increased by 1–10%, which is attributed to elimination of residual porosity. The hardness and indentation fracture toughness of specimens IP sintered at  $1850\text{ }^{\circ}\text{C}$  decreased after HIP (hot isostatic pressing) by 6 and 15%, respectively. The HIP of CW (warm pressing of polymer-coated alumina powder) composites increased their hardness and fracture toughness by approximately 10%. The maximum fracture toughness of  $5.2 \pm 0.2 \text{ MPa m}^{1/2}$  was measured for the materials containing 8 vol.% of SiC. A correlation was found between the fracture toughness, and the mean size and volume fraction of intergranular SiC inclusions in composites CW.

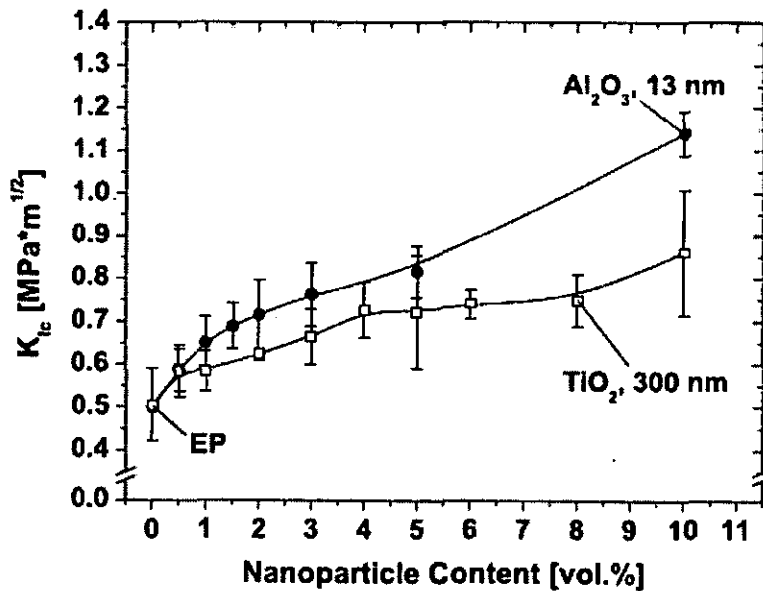


**Figure 6.1** Fracture toughness vs. nanoparticles volume content for EP (epoxy) /Al<sub>2</sub>O<sub>3</sub> and EP/TiO<sub>2</sub> nanocomposites [1].

Since the paper of carbon nanotubes (CNTs) was published by Iijima in 1991 [4], use of the CNTs to fill polymers has received remarkable success in materials mechanical properties [5–11]. In the fracture toughness area, the studies of Peng Guo, et al. show that in multiwalled carbon nanotubes (MWCNTs)/epoxy nanocomposites

which fabricated by using ultrasonication and the cast molding method, the fracture strain was enhanced distinctly with the increase of MWCNTs addition (shown in Figure 6.2). therefore, the fracture toughness of polymer matrix is increased as well.

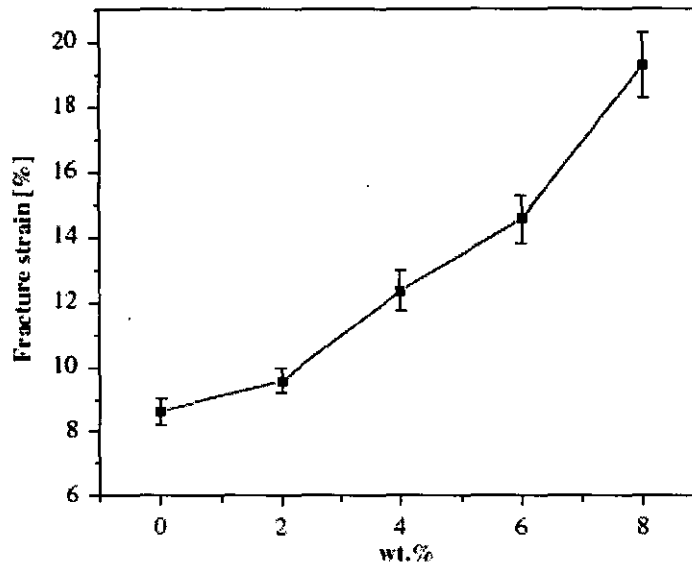


**Figure 6.2** The effects of MWCNTs loading content (wt.%) on the mechanical performances of CNTs/epoxy composites: fracture strain [12]

Inorganically treated titanium dioxide and organically treated Na-montmorillonite to enhance the toughness of epoxy matrix has been reported by Jin-Chein Lin and L. C. Chang et. al. [32]. The filler content were varied from 2 to 10 vol%, the epoxy matrix was polyester cured by a polyamine hardener at high temperatures. The nanocomposite was mixing epoxy matrix with filler particles, the mixture was sonicated by ultrasound and degassed under vacuum to further disperse the clay in the resin. When the mixture was cooled to room temperature, the catalyst was added for further mixed and followed by the process of pouring into a mold. The experimental results are found that the tensile strength, loss modulus, impact strength and dynamic thermal rheology of nanocomposites are extensively affected by the geometry, temperature, volume and type of filler content, and homogeneity of the nanoparticles.

Using nanoparticles, nanoplatelets and nanotubes to enhance the polymer toughness has been validated in above examples, but different geometry of nanofillers lead to different extent enhancement. Directly characterizing the effect of nanofiller geometry to nanocomposites at nanometer scale is still a challenging task. On the other hand, simulations based on both discrete and continuum models have provided useful insight into the geometry effect of nanocomposites. The methods of MD have been extensively applied in the study of fracture in material systems such as metals, semiconductors and CNTs, etc.. The main objective of this chapter is to investigate the effect of the geometry of nanofillers on the fracture behaviour of polymer nanocomposites.

## **6.2. Models of simulation**

### **6.2.1. Model of polymer chain**

The model of polymer chain continued beads-Spring model which has been used in the chapter 4 and chapter 5. In the model, the polymer chains are described as spherical beads connecting with unearthy spring. The interactions rules are controlled by a Lennard- Jones potential with a cut- off radius and an attractive finitely extensible nonlinear elastic (FENE) potential, which details are shown in chapter 4 and chapter 5.

### **6.2.2. Model of nanoparticles**

The nanoparticles are considered as granules. Each granule has a radius,  $R_p$  (shown in Figure 6.2.1.). The Figure 6.3 shows the sketch map of the nanoparticles model with a cut- off radius. O is the centre of the nanoparticles sphere,  $R_p$  is the radius of nanoparticles sphere,  $r_{pc}$  is cut- off radius of nanoparticles. OA, OB and OC are the radius of nanoparticles sphere, AA', BB' and CC' are the cut- off radius in the direction of OA, OB and OC, respectively. The interactions between two nanoparticles are described by an emendatory 6- 12 Lennard- Jones potential with a



cut- off radius,  $r_{pc}$ , which  $r_{pc}$  thosen as:  $r_{pc} = 2.5\sigma$ .

$$\text{For } A = 2l^2 \quad (6.1)$$

Where  $A$  is the surface area of the nanoplatelet model,  
 $l$  is the length of nanoplatelet model.

$$A' = 4\pi R_p^2 \quad (6.2)$$

Where  $A'$  is the surface area of nanoparticles model,  
 $R_p$  is the radius of nanoparticles model.

Duo to the surface area of nanoparticle is supposed same with the surface area of nanoplatelet and nanotube ( $A=A'$ ), then:

$$2l^2 = 4\pi R_p^2 \quad (6.3)$$

Therefore,

$$R_p = \sqrt{\frac{2}{\pi}}l = 0.798l \quad (6.4)$$

The nanoparticle has a mass,  $m$ , which is well- proportioned disturbed on the surface of the model.

The total elements in the simulation system were 4096 (nanoparticles 40 + segments 4056). The same cut- off radius and length scale of nanoparticle granule and monomers will be used in this work, and the density of nanoparticles is chosen by 3 times of the density of monomers. The characteristic energy of nanoparticles is chosen by 3 times of the characteristic energy of monomers. Periodic boundary conditions were applied in x- axis and y- axis directions, while the z direction was bounded by

walls. At the initial stage, the system was equilibrated, i.e, energy of the system is minimized and the nanoparticles were uniformly distributed in the polymer matrix. The speed of the stretching along z- axis was  $v = 0.03 \sigma/\tau$ .  $\tau$  is the characteristic time. It was assumed that the failure never occurs at the interface between walls and the polymer matrix. For simulation,  $0.005\tau$  was used as time step.

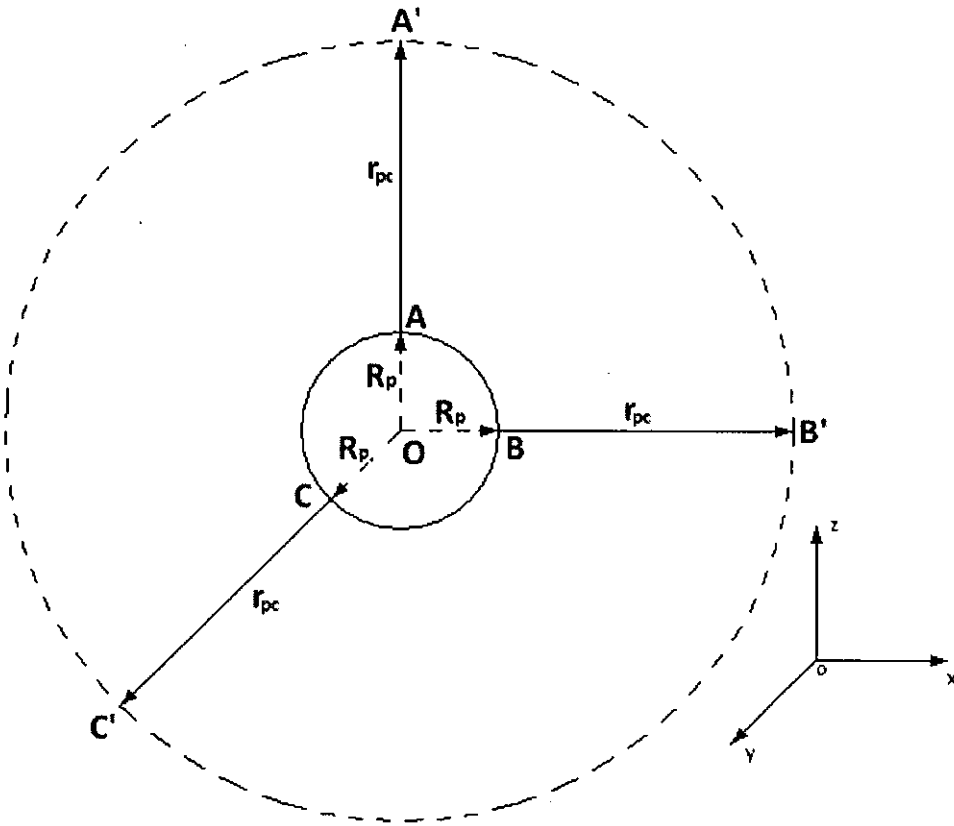


**Figure 6.3** Schematic map of the nanoparticles model with a cut- off radius. O is the centre of the nanoparticles sphere,  $R_p$  is the radius of nanoparticles sphere,  $r_{pc}$  is cut-off radius of nanoparticles. OA, OB and OC are the radius of nanoparticles sphere, AA', BB' and CC' are the cut- off radius in the direction of OA, OB and OC, respectively.

### 6.2.3. Model of nanoplatelet

The model of a nanoplatelet is continued the model of nanoplatelets used in the

former chapters, which considered that the modality of a nanoplatelet is a hard square flat panel with a thickness, but the thickness of flat panel was not taken into account. The length of the flat panel is  $l$ , and then the surface area of nanoplatelet model is:

$$A = l^2 + l^2 = 2l^2 \quad (6.5)$$

The interactions between nanoplatelets and polymers followed an emendatory 6- 12 Lennard- Jones potential with a cut- off radius, which described as:

$$V_{pm}(r) = \begin{cases} 4\varepsilon_{pm} \left[ \left( \frac{\sigma}{r_{pm} - s_{pm}} \right)^{12} - \left( \frac{\sigma}{r_{pm} - s_{pm}} \right)^6 \right] & r < r_{pmc} \\ 0 & r \geq r_{pmc} \end{cases} \quad (6.6)$$

Where,  $V_{pm}(r)$  is Lennard- Jones potential between a nanoplatelet and a monomer of a neighboring polymer chain,

$r_{pm}$  is the distance between nanoplatelet and the monomer of a polymer chain, the  $r_{pm}$  are considered as  $r_{pm} = \frac{r_{pmA} + r_{pmB} + r_{pmC} + r_{pmD}}{4}$  (shown in Figure 6.4),

$$s_{pm} = \frac{\sigma_p + \sigma_m}{2},$$

$r_{pmc}$  is the cut- off radius between a nanoplatelet and a monomer of a neighboring polymer chain,

$\varepsilon_{pm}$  is characteristic energy between a nanoplatelet and a monomer of a neighboring polymer chain.

The total elements in the simulation system were 4096 (nanoplatelet segments 4056). The same cut- off radius and length scale of nanoplatelet flat panel and monomers

was used in this work, and the density of nanoplatelets was chosen by 3 times of the density of monomers. The characteristic energy of nanoplatelets was chosen by 3 times of the characteristic energy of monomers. Periodic boundary conditions were applied in x- axis and y- axis directions, and the z direction was bounded by walls. At the initial stage, the system was equilibrated, just like the initial stage of nanoparticles- polymer matrix system. The speed of the stretching along z- axis was fixed at  $v = 0.03 \sigma/\tau$ .  $\tau$  is the characteristic time. It was assumed that the failure never occurs at the interface between walls and the polymer matrix. For simulation,  $0.005\tau$  was used as time step.

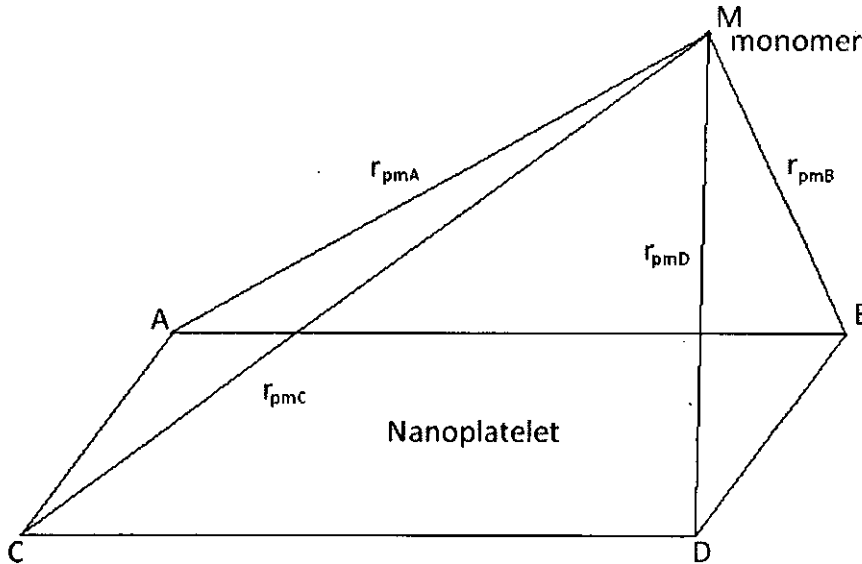


**Figure 6.4** Schematic map of the calculation of the distance between a nanoplatelet and a monomer of a neighboring polymer chain,  $r_{pm}$ .

#### 6.2.4. Model of nanotube

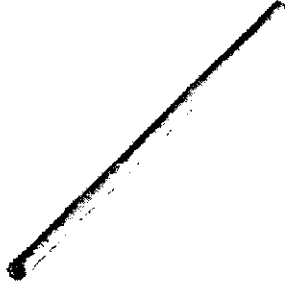


**Figure 6.5** Schematic map of a nanotube model.

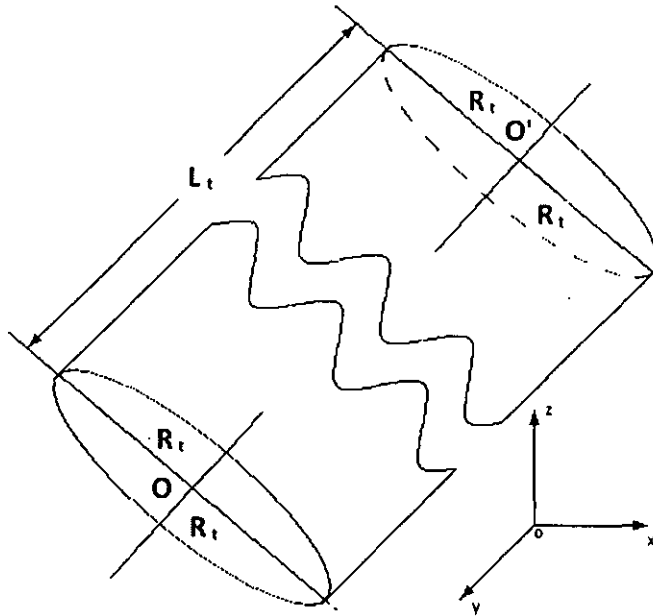


**Figure 6.6** Schematic map of the calculation of  $L_t$ . O and O' are the centres of two nanotube cross sections, respectively.  $R_t$  is radius of the nanotube cross section,  $L_t$  is the length of nanotube.

A nanotube is a nanometer scale tube-like structure. Carbon nanotube (CNT) is one of the most commonly used nanofillers in nanocomposites. In the simulation, the nanotube was considered as a threadlike solid cylinder which the cross section of the cylinder was not taken into account (shown in Figure 6.5). The nanotube has a mass,  $m$ , which is well- proportioned disturbed on the surface of the model.

In Figure 6.6, O and O' are the centres of two nanotube cross sections, respectively.  $R_t$  is radius of the nanotube cross section,  $L_t$  is the length of a nanotube.

The surfacé area of a nanotube is:

$$A = 2\pi R_t L_t \quad (6.7)$$

The surface area of nanotube is equal to the surface area of nanoparticle and nanoplatelet, then:

$$R_t L_t = \frac{A}{2\pi} = \frac{l^2}{\pi} \quad (6.8)$$

Where  $l$  is the length of a nanoplatelet.

For it is supposed that  $\frac{R_t}{L_t} = \frac{1}{10}$ , then:

$$L_t^2 = \frac{10}{\pi} l^2 \quad (6.9)$$

Therefore,

$$L_t = \sqrt{\frac{10}{\pi}} l \cong 1.784l \quad (6.10)$$

The interaction between one nanotube and polymer chain are also described by a 6-12 Lennard- Jones potential with a cut- off radius,  $r_{lmc}$ , which is given by:

$$V_{tm}(r) = \begin{cases} 4\epsilon_{tm} \left[ \left( \frac{\sigma}{r_{tm} - s_{tm}} \right)^{12} - \left( \frac{\sigma}{r_{tm} - s_{tm}} \right)^6 \right] & r < r_{tmc} \\ 0 & r \geq r_{tmc} \end{cases} \quad (6.11)$$

Where,  $V_{tm}(r)$  is Lennard- Jones potential between a nanotube and a monomer of a neighboring polymer chain,

$r_{tm}$  is the distance between nanotube and the monomer of a polymer chain,

the  $r_{tm}$  are considered as  $r_{tm} = \frac{r_{tmA} + r_{tmB}}{2}$  (shown in Figure 6.7),

$$s_{tm} = \frac{\sigma_t + \sigma_m}{2},$$

$r_{tmc}$  is the cut- off radius between a nanotube and a monomer of a neighboring polymer chain,

$\epsilon_{tm}$  is characteristic energy between a nanotube and a monomer of a neighboring polymer chain.

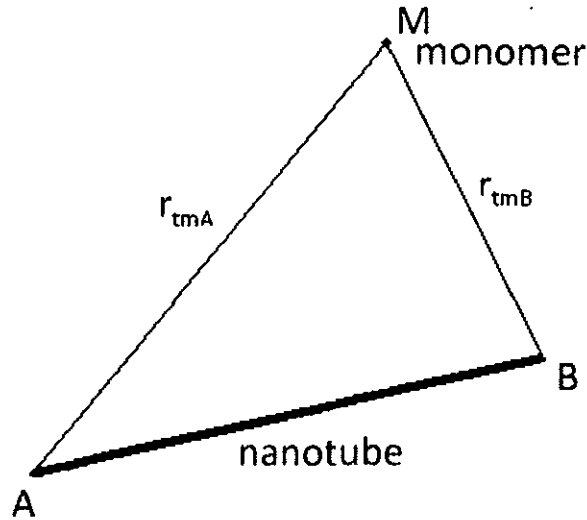


**Figure 6.7** The Schematic map of the calculation of the distance between a nanotube and a monomer (or segment) of a neighbouring polymer chain,  $r_{tm}$ .

The total elements in the simulation system were 4096 (nanotubes 40 + segments 4056). The same cut-off radius and length scale of nanotubes monomers were used in this work and the density of nanotubes was chosen by 3 times of the density of monomers. The characteristic energy of nanotubes was chosen by 3 times of the characteristic energy of monomers. Periodic boundary conditions were applied in x-axis and y-axis directions, while the z direction was bounded by walls. At the initial stage, the system was equilibrated, i.e, energy of the system was minimized and the nanotubes were uniformly distributed in the polymer matrix. The speed of the stretching along z-axis was  $v = 0.03 \sigma/\tau$ .  $\tau$  is the characteristic time. It was assumed that the failure never occurs at the interface between walls and the polymer matrix. For simulation,  $0.005\tau$  was used as time step.

### 6.3. Result and discussion

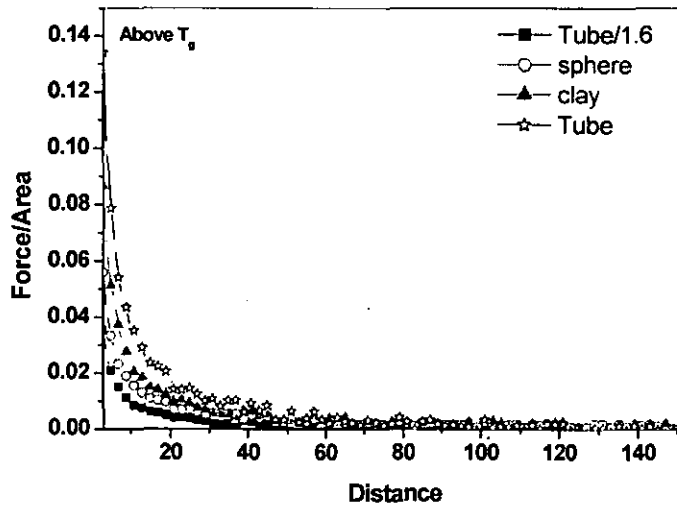


**Figure 6.8** The force/area curves vs. distance with different geometry of the nanofillers at  $1.1T_g$ .



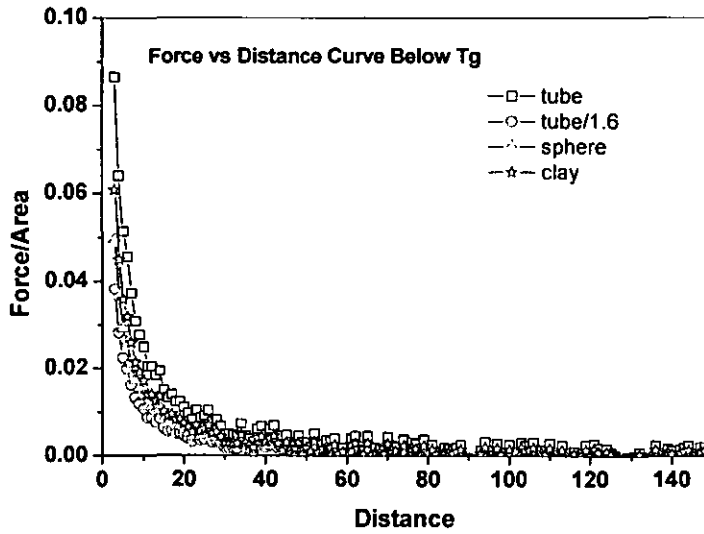


**Figure 6.9** The force/area curves vs. distance with different geometry of the nanofillers at  $0.4T_g$ .

Figure 6.8 and 6.9 show the force/area curves vs. distance with different geometry of the nanofillers at the temperature above  $T_g$  and below  $T_g$ , respectively. It can be seen that the addition of the nanofillers with different geometries has a significant influence on the force/area curve vs. distance of the polymer nanocomposite.

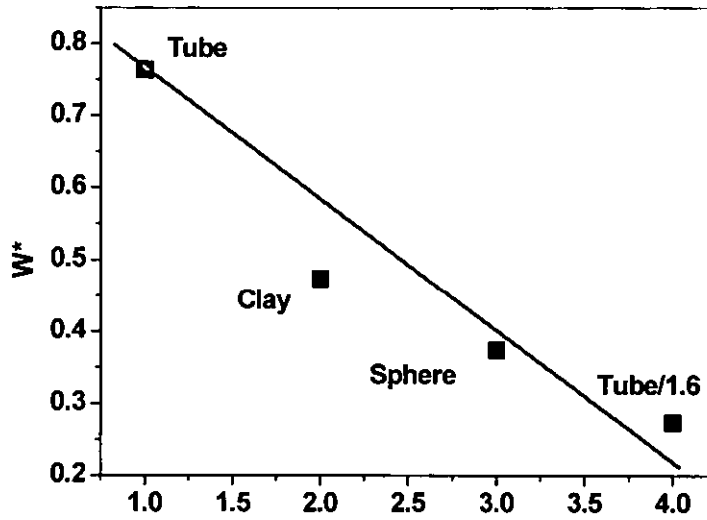


**Figure 6.10** The normalized work,  $W^*$ , to failure with different geometry of the nanofillers at  $0.4T_g$ .

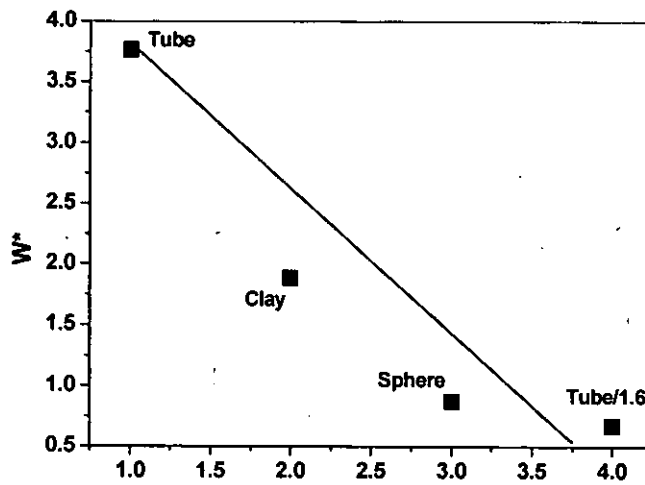


**Figure 6.11** The normalized work,  $W^*$ , to failure with different geometry of the nanofillers at  $1.1T_g$ .

Figures 6.10 and 6.11 show the normalized work,  $W^*$ , to failure.  $W^*$  is defined as the

work to failure of the polymer nanocomposite after cavitation has occurred divided by the work to failure of non-nanofiller system. Results indicate that  $W^*$  from high to low is nanotube, nanoplatelets, nanoparticles and nanotube with 1.6 times interactions between monomers at below the  $T_g$  of the polymer. It is clear that tube is the best one for the enhancement.

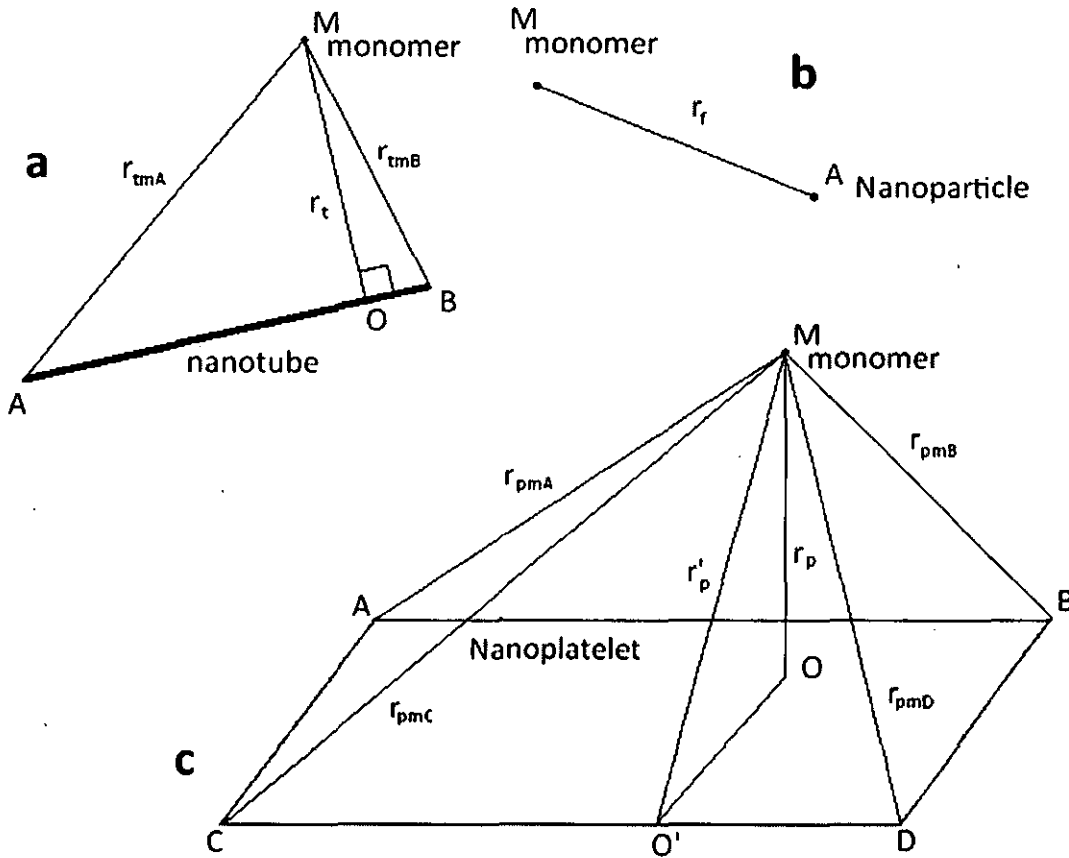


**Figure 6.12** The relationships of  $r_{fm}$ ,  $r_{pm}$  and  $r_{tm}$ , when  $r_f = r_p = r_t = r$

It can be assumed that the distance between monomer and nanofiller is  $r$ . if the distance between monomer and nanofiller are equal,  $r_f = r_p = r_t = r$ , then by the

Figure 6.12.:

$$r_{fm} = r_f \quad (6.12)$$

$$r_{tm} = \frac{r_{tmA} + r_{tmB}}{2} > r_t \quad (6.13)$$

$$r_{pm} = \frac{r_{pmA} + r_{pmB} + r_{pmC} + r_{pmD}}{4} > r'_p > r_p \quad (6.14)$$

Therefore:

$$r_{pm} > r_{tm} > r_{fm} \quad (6.15)$$

For E.6.2.1., E.6.2.3. and E.6.2.4.:

If  $\sigma < r$  then  $V(r)$ , then

$$V_{pm} > V_{tm} > V_{fm} \quad (6.16)$$

If  $\sigma > r$  then

$$V_{pm} < V_{tm} < V_{fm} \quad (6.17)$$

When  $\sigma < r$ ,  $V(r) > 0$ , it means the nanofiller and the monomer are attrahent each other, then during the deformation of nanocomposite the outside loading have to work to conquer  $V(r)$  in order to finish the deformation.

When  $\sigma > r$ ,  $V(r) < 0$ , it is means the nanofiller and the monomer are repulsive each other, then during the deformation of nanocomposite the energy dissipated equal to the work of outside loading subtract the  $V(r)$ .

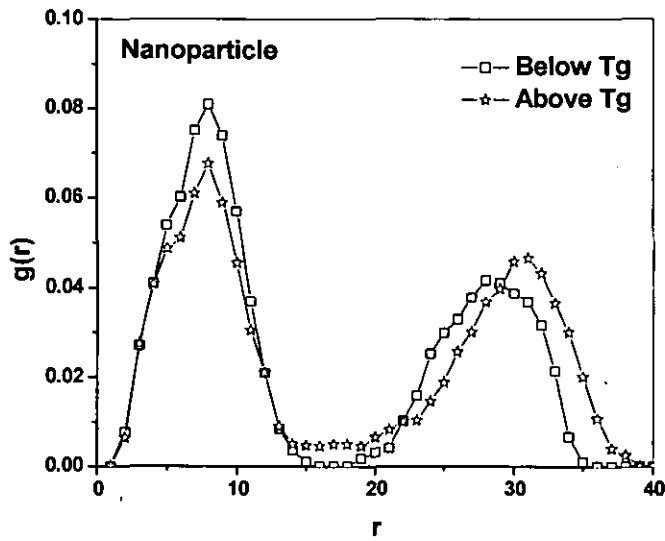


**Figure 6.13** Nanoparticle – nanoparticle correlation function,  $g(r)$  with 3wt.% content of nanoparticle.

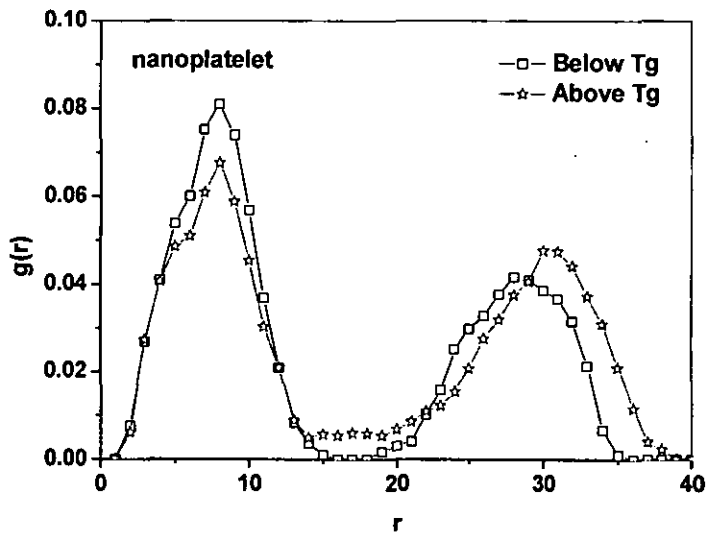


**Figure 6.14** Nanoplatelet – nanoplatelet correlation function,  $g(r)$  with 3wt.% content of nanoplatelets.

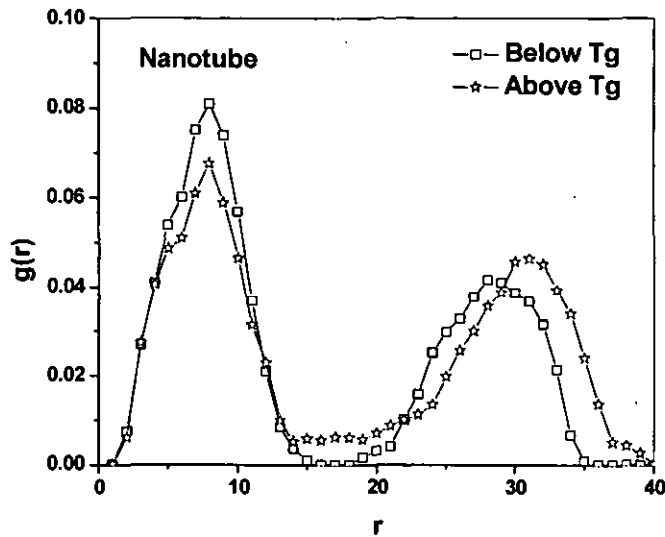


**Figure 6.15** Nanotube – nanotube correlation function,  $g(r)$  with 3wt.% content of nanotubes.

From Figure 6.13, Figure 6.14 and Figure 6.15 it can be seen that the system at above  $T_g$  always shows an increasing of amount of the nanofillers present in the bridge region during the simulation than at below  $T_g$ , because the more mobility of nanofillers have to form the temporary bonds even the local region at above  $T_g$  and the temporary bonds and local region can dissipate energy superfluity when the dimensions in nanometer range increased. But the mobility of nanofillers in all geometries will be reduced at below  $T_g$ .

## Reference

1. Bernd Wetzels, Patrick Rosso, Frank Hauptert, Klaus Friedrich, *Eng.Fra. Mech.* **73**, 2375, (2006).
2. Duřsan Galusek, Jaroslav Sedl'áček, Peter řSvan'c'arek, Ralf Riedel, Raphaëlle Satet, Michael Hoffmann, *J. Euro. Ceramic Soc.*, **27**,1237, (2007).

3. Duřsan Galusek, Jaroslav Sedl'aček, Ralf Riedel, *J. Euro. Ceramic Soc.*, **27**, 2385, (2007).
4. Iijima S. Helical microtubules of graphitic carbon. *Nature*, **354**,56, (1991).
5. Frank S, Poncharal P, Wang ZL, de Heer WA. *Science*, **280**, 1744, (1998).
6. Tsukagoshi K, Alphenaar BW, Ago H. *Nature*, **401**, 572, (1999).
7. Allaoui A, Bai S, Cheng HM, Bai JB. *Compos Sci Technol*, **62**, 1993, (2003).
8. Liao YH, Marietta-Tondin O, Liang ZY, Zhang C, Wang B. *Mater Sci Eng A* **385**, 175 (2004).
9. Miyagawa H, Drzal LT. *Polymer*, **45**, 5163 (2004).
10. Zhu J, Kim J, Peng H, Margrave JL, Khabashesku VN, Barrera EV. *Nano Lett*, **3**, 1107, (2003).
11. Zhu J, Peng H, Rodriguez-Macias F, Margrave JL, Khabashesku VN, Imam AM, et al. *Adv Funct Mater*, **14**,643,(2004).
12. Peng, G, Xiaohong. C, Xinchun.G, Huaihe S, Heyun S, *Com.Sci. Tech.*, **67**, 3331, (2007).

## **CHAPTER 7**

### **CONCLUSIONS AND FUTURE WORKS**

Fracture and energy dissipation in polymer clay nanocomposites have been investigated by computer simulation and experimentally. The following conclusions have been conducted:

A computer programme of molecular dynamics simulations for investigation of the effect of nanofillers on fracture and energy dissipation of polymers has been developed and validated.

Molecular dynamics simulation (MD) results reveal that the addition of layered silicate can improve the fracture strength of polymers. The interactions between the surface of layered silicate and polymer chains, and the difference between the relaxation times of layered silicate and that of polymer chains have significant influences on the fracture strength of polymers. For these polymers, which their  $T_g$ s are lower than room temperature, such as polyurethane, or nearby (or equal to) room temperature, such as nylons, the nanoplatelets can always enhance the mechanical properties. However, for these polymers, which  $T_g$ s are higher than room temperature, such as epoxy and polystyrene, the addition of the nanoplatelets does not work well for toughening these polymers. If one wants the nanoplatelets to be working for toughening these polymers, it is necessary to build up a stress relaxation interface between the polymer matrix and the nanoplatelet, such as the modification of the surfaces of nanofillers using coupling agents. Figure 7.1 (reproduced) indicates when the relaxation time of the polymer is long enough, the incorporation of nanofillers into the polymer will cause the polymer more brittle. This result explains why the toughness of epoxy clay nanocomposites becomes poor.



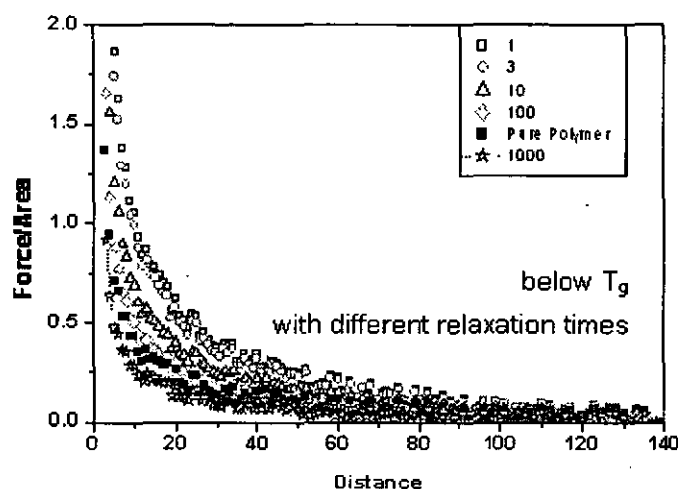


**Figure 7.1** The force/area curves vs. distance with content of the nanoplatelets at  $0.4T_g$ .

The simulation results clearly revealed that the orientation of nanoplatelets is reversible at low strain of 50% suggesting that additional energy dissipation only results from the frictional sliding at the interface, whereas the orientation of nanoplatelets at large strain of 200% showed more irreversible suggesting that the additional energy loss results from both the interfacial frictional sliding and the orientation of the nanoplatelets. The additional dissipated energy was also influenced by the strength of interactions between polymer chains and clay platelets. The stronger interactions the more energy dissipated. Figure 7.2 (reproduced) shows the findings.

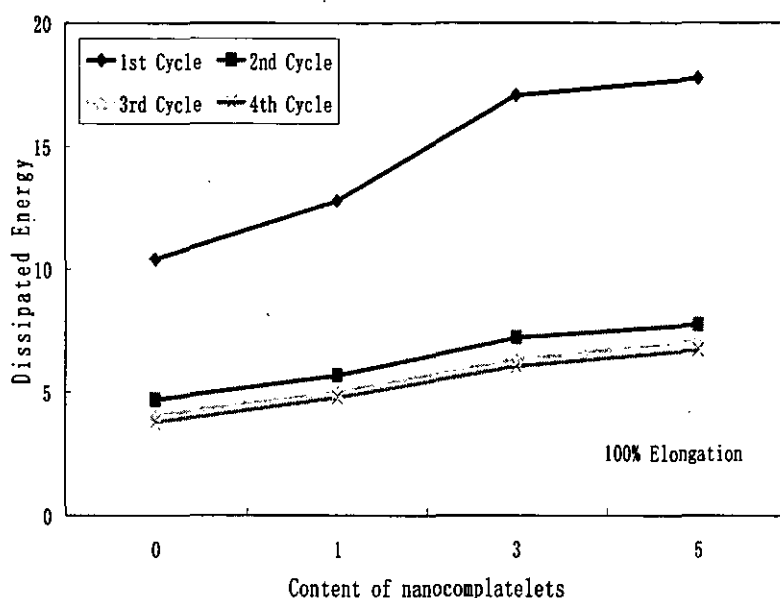


Figure 7.2 Dissipated energy vs. content of nanoplatelets at 100% elongation.

The system of polymer clay nanocomposites tested at above its  $T_g$  always shows an increase in the amount of the nanofillers presenting in the bridge region than tested below  $T_g$ . This is because the mobility of nanofillers becomes higher and form temporary bonds above  $T_g$ . The temporary bonds can dissipate energy. But the mobility of nanofillers in all geometries will be reduced tested at below  $T_g$  of the polymer.

Molecular dynamics simulation results revealed that the geometry of nanofillers can affect the mechanical properties of polymer nanocomposites. The enhancement of carbon nanotubes on the mechanical properties of the polymer is the highest.

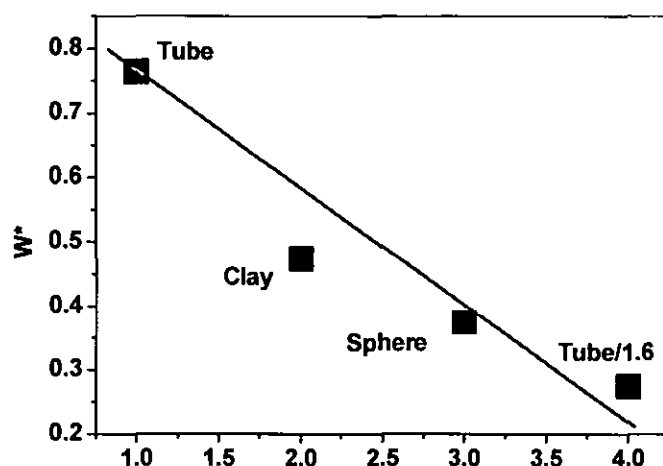


Figure 7.3 The normalized work,  $W^*$ , to failure with different geometries of the nanofillers at  $0.4T_g$ .

The addition of organoclay leads to the increase in energy dissipation, which mainly results from the friction of PU chains and the surface of the organoclay. Theoretically, the increase in energy dissipation will lower the fatigue durability. However, the fatigue durability of PU significant increased by the incorporation of organoclay. We believe that firstly, the reduced hard-segment domain size with wider interfacial region as micro-barriers to lead a rise of fatigue resistance. Secondly, the orientation of clay nanoplatelets is reversible during fatigue test, which does not contribute any dissipated energy, which generates heat, to the PU matrix. Thirdly, the nanospring acts as a point, which can stop the crack growth when the tip of a crack reaches the nanospring. In fact, the effect of addition of organoclay on the increase in dissipated energy is also not very significant. Overall, the positive effect on the improvement of fatigue durability is much more important than heat generated by the friction between PU chains and the surface of organoclay, which will lower fatigue durability.

Although the effect of incorporation of nanofillers on toughness and energy dissipation of polymers has been investigated by computer simulations, but only

simple model was used in the simulation such as the interactions of internal molecular segments and the configuration of nanofillers, and fixed speed of the blank. In fact, variation of these parameters need to be considered. Therefore, the followings need to be considered in the future,

1. Use a larger system
2. Change introduction speed of the blank
3. Built up more complex nanofiller configurations
4. Validate these results obtained using above 1-3.

## **APPENDIX**

### **PUBLICATIONS:**

Song, m. and Chen, L., "Molecular Dynamics Simulation of the Fracture in Polymer-Exfoliated Layered Silicate nanocomposites", *Macromolecular Theory & Simulations*, 15, 2006, pp238-245.

Xia, H.S., Song, M., Jin, J. and Chen, L., "Poly(propylene glycol)-Grafted Multi-Walled Carbon nanotube Polyurethane", *Macromolecular Chemistry and Physics*, 207, 2006, pp 1945-1952.

Jin, J., Chen, L., Song, M. and yao, K.J., "An Analysis on Enhancement of Fatigue Durability of Polyurethane by Incorporating Organoclay Nanofillers" *Macromolecular Materials and Engineering*, 291, 2006, pp 1411-1421.

Jin, J., Song, M., Yao, K. J. and Chen, L., "A Study of Viscoelasticity of Polyurethane-organical Nanocomposites", *Journal of Applied Polymer Science*, 99(6), 2006, pp 3677-3683.

Chen, L., Jin, J. and Song, M., "Energy Dissipation in Exfoliated Polymer/Organoclay Nanocomposites", Submitted to *Journal of Applied Polymer Science* for publication.



